

The transpeptidase PBP2 governs initial localization and activity of the major cell-wall synthesis machinery in *E. coli*

Gizem Özbaykal^{1,2*}, Eva Wollrab^{1*}, Francois Simon¹, Antoine Vigouroux^{1,3,4}, Baptiste Cordier¹, Andrey Aristov¹, Thibault Chaze⁵, Mariette Matondo⁵, and Sven van Teeffelen^{1#}

1. Microbial Morphogenesis and Growth Lab, Institut Pasteur, Paris, France
2. Université Paris Diderot, Sorbonne-Paris-Cité, Paris, France
3. Synthetic Biology Lab, Institut Pasteur, Paris, France
4. Université Paris Descartes, Sorbonne-Paris-Cité, Paris, France
5. Proteomics Platform, Institut Pasteur, Paris, France

* These authors contributed equally to the work.

Correspondence should be addressed to Sven van Teeffelen
(sven.vanteeffelen@gmail.com)

Table of contents

Main text	1
Bibliography	17
Main figures	21
Methods	28
Supplemental Figures	49
Captions for Supplementary Files	71
Video captions	71
Captions for Supplemental Datasets for Figures	72

1 Abstract

2 Bacterial shape is physically determined by the peptidoglycan cell wall. The cell-wall-
3 synthesis machinery responsible for rod shape in *Escherichia coli* is the processive 'Rod
4 complex'. Previously, cytoplasmic MreB filaments were thought to govern formation and
5 localization of Rod complexes based on local cell-envelope curvature. Using single-particle
6 tracking of the transpeptidase and Rod-complex component PBP2, we found that PBP2
7 binds to a substrate different from MreB. Depletion and localization experiments of other
8 putative Rod-complex components provide evidence that none of those provide the sole
9 rate-limiting substrate for PBP2 binding. Consistently, we found only weak correlations
10 between MreB and envelope curvature in the cylindrical part of cells. Residual correlations
11 do not require curvature-based Rod-complex initiation but can be attributed to persistent
12 rotational motion. We therefore speculate that the local cell-wall architecture provides the
13 cue for Rod-complex initiation, either through direct binding by PBP2 or through an unknown
14 intermediate.

16 The peptidoglycan (PG) cell wall is the major load-bearing structure of the bacterial cell
17 envelope and physically responsible for cell shape (Vollmer et al., 2008). Rod-like cell shape
18 in *Escherichia coli* requires peptidoglycan synthesis by stable multi-enzyme 'Rod complexes'
19 containing the transglycosylase RodA, the transpeptidase PBP2, the transmembrane protein
20 RodZ, and the actin homolog MreB (Cho et al., 2016; Emami et al., 2017; Meeske et al.,
21 2016; Morgenstein et al., 2015; Typas et al., 2012). All of these proteins move persistently
22 around the cell circumference at similar speeds (Cho et al., 2016; Morgenstein et al., 2015;
23 van Teeffelen et al., 2011), suggesting that these proteins stably associate for processive
24 cell-wall insertion. Colocalization of MreB and RodZ (Alyahya et al., 2009; Bendezú et al.,
25 2009; Morgenstein et al., 2015) supports this idea.

26 Other proteins (MreC, MreD, PBP1a, and PBP1b) are possibly also part of these complexes
27 (Banzhaf et al., 2012; Cho et al., 2016; Contreras-Martel et al., 2017; Kruse et al., 2004;
28 Morgenstein et al., 2015). MreC activates PBP2 (Contreras-Martel et al., 2017; Rohs et al.,
29 2018). However, the shape defect of a *mreCD* deletion is partially suppressed by a
30 hyperactive PBP2 point mutant (Rohs et al., 2018), suggesting that neither MreC nor MreD
31 are strictly necessary for Rod-complex assembly or function. The bi-functional class-A
32 penicillin-binding proteins PBP1a and PBP1b interact with PBP2 and RodZ, respectively
33 (Banzhaf et al., 2012; Morgenstein et al., 2015), and PBP2 activates PBP1a
34 glycosyltransferase activity *in vitro* (Banzhaf et al., 2012). However, Rod-complex rotational
35 motion is independent of class-A PBP activity (Cho et al., 2016). Furthermore, single-
36 molecule tracking suggests that any possible association of PBP1a or PBP1b with the Rod
37 complex is short lived (Cho et al., 2016). Similar to *mreCD*, a *rodZ* deletion can also be
38 suppressed by point mutations in PBP2, RodA, or MreB (Shiomi et al., 2008). Summarizing,
39 it emerges, that RodA, PBP2, and MreB form the core of the Rod complex (Rohs et al.,
40 2018). On the contrary, the determinants of Rod-complex spatial distribution and activity,
41 which are ultimately responsible for cell shape, remain less well understood.

42 MreB filaments are intrinsically curved (Hussain et al., 2018; Salje et al., 2011). This
43 curvature likely stabilizes their circumferential orientation (Billaudeau et al., 2019; Hussain et
44 al., 2018; Olshausen et al., 2013; Ouzounov et al., 2016; Wang and Wingreen, 2013) and
45 the circumferential orientation of Rod complex motion (Errington, 2015; Hussain et al.,
46 2018).

47 Previously, it has been suggested that MreB filaments provide a platform that recruits other
48 Rod-complex components to the site of future cell-wall synthesis (Errington, 2015; Shi et al.,
49 2018; Surovtsev and Jacobs-Wagner, 2018). Accordingly, MreB filaments might be
50 responsible for the initial localization of Rod complexes. Ursell et al. and others suggested
51 that MreB filaments are attracted to sites of specific two-dimensional cell-envelope curvature
52 (Billings et al., 2014; Shi et al., 2018; Ursell et al., 2014) based on mechanical properties of

MreB filaments and RodZ-MreB interactions (Bratton et al., 2018; Colavin et al., 2018). However, correlations could also come about indirectly, for example through a curvature-independent depletion of MreB from highly curved cell poles (Kawazura et al., 2017) or through persistent motion (Hussain et al., 2018; Wong et al., 2017, 2019). Therefore, the initial localization of Rod complexes could in principle be governed by factors different from MreB. We thus wondered, whether the cell wall itself could provide a local cue for the initiation of Rod complexes, independently of cell-envelope curvature. Such a local cue would have to be sensed by a protein with a periplasmic domain that can possibly bind the cell wall.

An obvious candidate is the transpeptidase PBP2. For its cross-linking activity PBP2 must bring together donor peptides on nascent glycan strands and acceptor peptides in the cell wall. Binding of PBP2 to the existing cell wall could therefore provide an alternative mechanism of Rod-complex initiation. In support of this hypothesis, a PBP2(L61R) mutant shows increased cell-wall synthetic activity and affects the distribution of MreB-actin filament length (Rohs et al., 2018). Further support comes from localization studies in *E. coli* (Lee et al., 2014) and *Caulobacter crescentus* (Dye et al., 2005; Hocking et al., 2012). The spatial distributions of PBP2 and MreB only partially overlap, which is compatible with the hypothesis that PBP2 finds sites for activity independently of MreB.

Here, we used single-molecule tracking to demonstrate that diffusive PBP2 molecules stably bind to an immobile component in the cell envelope. Bound molecules transition between immobile and persistently moving states, the latter depending on Rod-complex activity. Interestingly, MreB filaments are not the binding substrate for PBP2, nor does MreB determine locations of PBP2 binding. Depletion and localization experiments of other known Rod-complex components suggest that none of those provide the sole substrate for PBP2 binding. These observations suggest that PBP2 or an unknown protein determine the initial localization of newly forming Rod complexes. We speculate that the cell wall itself provides the cue for Rod-complex initiation. In support of our observations, we found that MreB filaments are likely not recruited to regions of particular cell-envelope curvature in filamentous and normal cells, contrary to (Ursell et al., 2014). Specifically, we found only weak MreB-curvature correlations once cell poles were excluded from the analysis. Residual correlations were attributed to weak spontaneous cell bending, suggesting that they are caused by persistent rotational motion (Wong et al., 2017). Finally, we also found that fast diffusing molecules cannot contribute to processive Rod-complex activity due to limitations of diffusion, contrary to (Lee et al., 2014).

88 *PBP2 enzymes can be quantitatively separated into diffusive and bound fractions*

89 To study the role of PBP2 for the formation of Rod complexes we characterized its different
90 states of motion, which are potentially representative of different states of substrate binding
91 and activity. We imaged a functional, N-terminal protein fusion of the photo-activatable
92 fluorescent protein PAmCherry to PBP2 (Lee et al., 2014). The fusion is expressed from the
93 native *mrdA* locus at a level similar to the wild-type protein according to quantitative mass
94 spectrometry (Fig. 1–SI Fig. 1D; Supplementary File 1a) and Bocillin labeling experiments
95 [Fig. 1–SI Fig. 1A and also (Lee et al., 2014)]. The strain carrying the fusion maintains rod-
96 like cell shape with only slight deviations of average cell diameter and length (Fig. 1–SI
97 Fig. 1B) and does not show any growth defect (Fig. 1–SI Fig. 1C) (Lee et al., 2014).

98 We obtained single-molecule tracks by single-particle tracking *PhotoActivatable Localization*
99 *Microscopy* (sptPALM) (Manley et al., 2008) in total internal reflection fluorescence (TIRF)
100 mode, which restricts the observation to the bottom part of the cell. We first imaged PBP2
101 molecules at high frequency (intervals of 60 ms). We found both spatially extended
102 trajectories, corresponding to fast diffusing molecules, and trajectories that appeared as
103 localized, corresponding to immobile or slowly moving molecules (Fig. 1A, Fig. 1–Video 1).

104 We confirmed the presence of two distinct fractions of diffusing and localized molecules
105 based on the distributions of jump lengths during different time lags (Fig. 1B). Specifically,
106 we fit those distributions to a two-state or a three-state diffusion model using the Spot-On
107 tool (Hansen et al., 2018) (Methods; Supplementary File 2). Both models contain as a
108 special case an immobile population, and they lead to very similar results (Fig. 1B; Fig. 1–
109 SI Fig. 2). We found a diffusive population with average diffusion constant $D = 0.04 \mu\text{m}^2/\text{s}$
110 containing 74-78 % of all enzymes, and a second population with zero diffusion constant
111 containing 22-26% of all molecules (Supplementary File 1a). The three-state model led to
112 slightly better fits, predicting a larger fast-diffusing and a smaller slow-diffusing population
113 with diffusion constants of $D_1 = 0.015 \pm 0.005 \mu\text{m}^2/\text{s}$ and $D_2 = 0.055 \pm 0.006 \mu\text{m}^2/\text{s}$,
114 respectively. Because the true diffusive behavior might be more complex, we report the
115 average diffusion constant in the following. We confirmed our findings using an alternative
116 method that is based on the distribution of single-track effective diffusion constants, yielding
117 a slightly lower bound fraction (Fig. 1–SI Fig. 3).

118 Upon overexpressed by about three- to six-fold (Fig. 1–SI 1D) using the vector pKC128 that
119 expresses PAmCherry-PBP2 from the native *mrdAB* promoter (Lee et al., 2014) the fraction
120 of molecules with near-zero diffusion constant decreased to $12.3 \pm 1.1\%$ (Fig. 1H-I and
121 Fig. 1–SI Fig. 2). Here, the three-state diffusion model gave significantly better fits (Fig. 1–
122 SI Fig. 2). We therefore decided to use the three-state model throughout the rest of the

paper. We also noticed that the average diffusion constant of the diffusive population decreased from $D = 0.042 \pm 0.004 \mu\text{m}^2/\text{s}$ to $0.025 \pm 0.002 \mu\text{m}^2/\text{s}$. We will come back to this latter point further down.

While diffusing molecules are likely enzymatically inactive and possibly searching for new sites of cell-wall insertion (see further down), localized molecules are likely bound to an immobile substrate or part of slowly moving Rod complexes with anticipated speeds of 10-40 nm/s (Cho et al., 2016; van Teeffelen et al., 2011).

Bound PBP2 molecules are either persistently moving or immobile

To test whether all or part of the bound molecules were moving persistently we imaged PBP2 molecules at low frequency, taking images with an exposure time of 1 s and intervals of 3.6 s. The long exposure time effectively smears out the fluorescence of fast diffusing molecules, allowing us to detect the positions of individual bound molecules. Using this protocol, we found molecules that moved persistently, were immobile, or showed transitions between these two states (Fig. 1C-E, Fig. 1–Video 2, and Fig. 1–SI Fig. 4).

Persistently moving molecules showed similar distributions of speed and orientation as a functional msfGFP-MreB fusion (Ouzounov et al., 2016) expressed from the native *mreB* locus (Fig. 1F, G) (Cho et al., 2016), in agreement with previous measurements (Cho et al., 2016; van Teeffelen et al., 2011). For accurate velocity measurements, we obtained these results from movies acquired with a shorter time interval of 1 s. Straight tracks representing persistently moving molecules were selected based on the mean squared displacements (MSD) (Fig. 1–SI Fig. 5).

Because PBP2 molecules show transitions between different states in single trajectories, we quantified immobile and persistent states locally in time. Specifically, we classified motion states using a single threshold on the mean velocity during four consecutive time steps in movies acquired with 3.6 s interval (Fig. 1C-E). Window size and velocity threshold (8 nm/s) were chosen based on computationally simulated tracks (Fig. 1–SI Fig. 6A-C). In confirmation of our two-state model, we found good agreement between the average MSD obtained from experiment and simulation for immobile and persistent segments, respectively (Fig. 1–SI Fig. 6D-F). Other states of motion are therefore likely not present. Using this criterion, we found a persistent fraction of $42.2 \pm 1.1 \%$ of all bound molecules, while $57.8 \pm 1.1 \%$ remained immobile (Fig. 1H).

Upon overexpression of PAmCherry-PBP2 as above, we found that the persistent fraction remained nearly constant (Fig. 1I; Supplementary File 1a), suggesting that the number of active Rod complexes, $N_{\text{active}} = N_{\text{PBP2}}bp$ (with N_{PBP2} the number of PBP2 molecules, and b and p the bound and persistent fractions, respectively), increased by about two-fold (Fig. 1–SI Fig. 7B). This finding suggests that PBP2 is an important limiting component for the number of active Rod complexes. This viewpoint is consistent with the recent report that a

hyperactive PBP2 point mutant (L61R) increased the overall amount of active Rod complexes (Rohs et al., 2018). We will come back to this mutant in the next section.

msfGFP-PBP2 fusion confirms findings and demonstrates increased PBP2 binding upon PBP2 depletion

We tested our findings using a strain that carries a functional msfGFP-PBP2 fusion (Cho et al., 2016) expressed at the native *mrdA* locus (AV127). Surprisingly, PBP2 levels were about four-fold lower than in the wildtype according to quantitative mass spectrometry. Yet, the strain showed normal cell shape and growth (Fig. 1–SI Fig. 8A). Tracking msfGFP-PBP2 at high frequency after initial pre-bleaching, we found a fraction of bound PBP2 molecules of $36.5 \pm 5 \%$ (Fig. 1–SI Fig. 8C, Fig. 1– Video 3), which is higher than in the case of PAmCherry-PBP2.

To test whether the higher fraction was due to reduced PBP2 levels, we also used a strain that carries the same msfGFP-PBP2 fusion under IPTG-inducible control as the sole copy of PBP2 (MG1655 *mrdA::aph* ($P_{lac}::msfgfp-mrdA$)) (Cho et al., 2016). Indeed, we found that the bound fraction decreased with increasing induction level (Fig. 1–SI Fig. 8C), qualitatively similar to the PAmCherry fusion.

To our surprise, near-wild-type levels observed at low induction (5 μ M IPTG) led to loss of rod shape at long times (Fig. 1–SI Fig. 9A), even though average PBP2 levels were close to wild-type levels after 6h (Fig. 1–SI Fig. S8B) and remained constant during long-term exponential growth (Fig. 1–SI Fig. 9A). Since AV127 did not display shape defects despite lower average levels of msfGFP-PBP2, we reasoned that shape defects might be due to the noisier expression from the inducible promoter.

Long-term shape changes in the inducible strain were accompanied by an almost two-fold increase of the bound fraction (Fig. 1–SI Fig. 9B). We therefore speculated that stronger PBP2 binding might be a response to the increased need for Rod-complex activity. We will come back to a potential feedback between PBP2 binding and cell-wall architecture further down.

As a test of our method, we also tracked an msfGFP fusion to the PBP2 point mutant (L61R) recently characterized by (Rohs et al., 2018). Based on slow-frequency imaging, they reported that the number of bound msfGFP-PBP2(L61R) was about two-fold increased as compared to msfGFP-PBP2 (Rohs et al., 2018). We confirmed this finding quantitatively, using the same inducible PBP2 fusions (Rohs et al., 2018) (Fig. 1–SI Fig. 8C).

Among the bound wildtype molecules we found a fraction of 76-83 % persistently moving molecules, depending on strain and expression level (Fig. 1–SI Fig. 10A, Supplementary File 1a, Fig. 1– Video 4), which is significantly higher than in the case of the PAmCherry fusion. We therefore reasoned that the PAmCherry fusion might have reduced functionality.

However, similarly to the PAmCherry fusion, the persistent fraction remained nearly constant over the 20-fold range of expression levels (according to Western Blot) (Fig. 1–SI Fig. 10A, Supplementary File 1a). Therefore, PBP2 activity is predominantly limited by the number of bound PBP2 molecules, similar to the PAmCherry fusion.

We also measured persistent motion in the PBP2(L61R) mutant and found that the persistent fraction is reduced in comparison to the wild-type protein (Fig. 1–SI Fig. 8A, p-value 0.016).

In summary, these results are compatible with our findings with the PAmCherry fusion.

PBP2 molecules show long persistent runs

The classification into different motion states at the sub-trajectory level allowed us to extract average transition rates between immobile and persistently moving states, k_{ip} and k_{pi} , respectively (Fig. 2A-B). Depending on the fluorescent-protein fusion, we found values of k_{ip} between 0.014-0.063 s⁻¹, and of k_{pi} between 0.009-0.031 s⁻¹. The msfGFP-PBP2 fusion shows less frequent arrests and faster transitions from immobile to persistently moving states, in agreement with its higher fraction of moving molecules (Fig. 1–SI Fig. 10A).

A persistent run of PBP2 terminates either due to an arrest of PBP2 (persistent-to-immobile transition) or due to an unbinding event (persistent-to-diffusive transition). As an upper bound of the unbinding rate, we measured the transition rate from the aggregate bound state (persistent and immobile states) to the diffusive state, k_{bd} (Fig. 2A). Specifically, we acquired distributions of track lengths for two different imaging intervals of 1 s and 12 s (Fig. 2C), using the inducible msfGFP-PBP2 fusion with 25 μM IPTG for the higher number of tracks obtained. Track length is limited by bleaching, unbinding, and persistent molecules leaving the field of view. The latter two processes are responsible for the shorter track lengths observed for $dt = 12$ s. Taking all three processes into account in computational simulations, we obtained an upper limit of the unbinding rate of $k_{bd} < 0.03$ s⁻¹, corresponding to a minimum average lifetime of 30 s (Fig. 2–SI Fig. 1).

The rates k_{pi} and k_{bd} then yield the possible ranges of average run lengths of persistently moving molecules between 0.3-1.6 μm, depending on protein fusion and exact unbinding rate. This range is compatible with long tracks of MreB motion observed previously (van Teeffelen et al., 2011).

PBP2 spatial pattern and bound fraction are independent of MreB cytoskeleton

MreB is often regarded as a hub for Rod-complex components (Errington, 2015; Shi et al., 2018; Surovtsev and Jacobs-Wagner, 2018). To determine whether MreB is the substrate of PBP2 binding we treated cells with the putative MreB-polymerization inhibitor A22 (Gitai, 2005). A22 treatment (50 μg/ml) strongly reduced both number and size of MreB-msfGFP

spots observed in the cell envelope (Fig. 3A-D, Fig. 3–SI Fig. 1-2) and abolished rotational motion (Fig. 3– Videos 1-2). We observed the same qualitative behavior for a functional RodZ-GFP fusion (Bendezú et al., 2009) expressed as the sole copy of RodZ (Fig. 3A-D, Fig. 3–SI Fig. 1-2). On the contrary, the spotty pattern of mCherry-PBP2 did not change during A22 treatment. Since these images were taken with a long exposure time (1s), each spot likely represents multiple bound PBP2 molecules. Our results thus indicate that MreB filaments are not the binding substrate for PBP2. We will come back to the role of RodZ further down.

Next, we measured bound and persistent fractions of PBP2 molecules before and after A22 treatment. The bound fraction remained close to the value of untreated cells for both PAmCherry- and msfGFP fusions (Fig. 3E; Fig. 3–SI Fig. 3). Yet, the fraction of persistently moving molecules nearly vanished (Fig. 3F). This is consistent with the arrest of MreB rotation (Fig. 3– Video 2) and with previous bulk measurements of Rod-complex activity (Uehara and Park, 2008). To follow the bound fraction during two mass-doubling times (Fig. 3E), we used an intermediate concentration of A22 (20 µg/ml), which did not affect growth (Fig. 3–SI Fig. 4A). Together, our findings suggest that MreB polymers are neither the substrate of PBP2 binding nor do they affect the rate of PBP2 binding and unbinding.

MreB depolymerization did also not elicit a rapid change of the diffusion constant of the freely diffusing molecules (Fig. 3E), suggesting that MreB does not significantly constrain the movement of diffusive PBP2 molecules (Strahl et al., 2014). Therefore, if PBP2 binds its substrate from the diffusive state, the locations of PBP2 binding are also independent of MreB.

A22 treatment already demonstrates that PBP2 binding is independent of Rod-complex activity. We confirmed this finding using the PBP2-targeting beta-lactam Mecillinam, which binds covalently to the active site (Spratt, 1975). Mecillinam did not cause a reduction of the bound fraction (Fig. 3E), demonstrating that PBP2 binds its binding target with a moiety different from its active site.

At long times of treatment with Mecillinam or A22 (120 min) the bound fraction increased and the diffusion constant decreased (Fig. 3E), which coincides and is potentially caused by the loss of normal cell-wall architecture during loss of rod-like cell shape (Fig. 3–SI Fig. 4C), similar to the increase of the bound fraction at sustained low induction levels of msfGFP-PBP2 (Fig. 1–SI Fig. 9B).

PBP2 binds to its substrate at locations that are independent of MreB localization

To demonstrate that PBP2 binding was indeed independent of MreB filaments or Rod-complex activity as suggested by Fig. 3 we still needed to show that PBP2 molecules interchange between diffusive and bound states during A22 treatment. We already found a low upper bound for the transition rate from bound to diffusive states in non-treated cells (k_{bd}

$< 0.03 \text{ s}^{-1}$) (Fig. 2C), and we expect inverse transitions to occur even more rarely. We therefore used a variant of Fluorescence Recovery After Photobleaching (FRAP) (Fig. 4A) termed Bound-Molecule FRAP: Instead of measuring fluorescence intensity we measure the bound fraction at different time points, after bleaching almost all molecules at the bottom of the TIR field of view. Right after bleaching, the bound fraction dropped significantly (Fig. 4B), suggesting that fast diffusing molecules re-entered the observation window within less than half a minute but did not quickly bind their substrate. Within about 2-4 min the bound fraction recovered, yielding a transition rate from diffusive to bound states of $k_{db} = (4.3 \pm 2) \cdot 10^{-3} \text{ s}^{-1}$. The same experiment in non-treated cells did not reveal recovery of the bound fraction (Fig. 4–SI Fig. 1), likely because bound molecules leave the field of view through persistent motion within less than 1 min (Methods).

Since the bound and diffusive fractions did not change by more than 10% after A22 treatment, transition rates from the diffusive into the bound states must be matched by reverse transitions from the bound to the diffusive state with a rate $k_{bd} = k_{db}(1-b)/b = 0.015 \pm 0.009 \text{ s}^{-1}$, where b is the bound fraction. We confirmed this expectation through independent lifetime measurements of A22-treated cells, similar to those in Fig. 2 (Fig. 4C), yielding $k_{bd} = 0.018 \pm 0.01 \text{ s}^{-1}$. Since bound fractions are almost identical for untreated and A22-treated cells, we reasoned that binding and unbinding rates k_{bd} and k_{db} are likely also the same in both conditions.

The average lifetime of a bound molecule of about 1 min is 70-fold smaller than the cell doubling time of 70 min (Fig. 1–SI Fig. 1C). Therefore, almost all bound PBP2 molecules observed at any time have undergone multiple transitions from the diffusive to their current bound state. Together with the previous observation that free diffusion is not constrained by MreB filaments. We can thus conclude that PBP2 binds its substrate at locations that are determined independently of MreB filaments.

PBP2 or an unknown low-abundant substrate determines the location of new Rod complexes

Two qualitatively different scenarios for the formation of an active Rod complex are conceivable (Fig. 4D): First, PBP2 could bind to a location in the cell envelope and then recruit MreB filaments directly (through diffusion and capture or through nucleation). Alternatively, MreB filaments could bind the PBP2-binding site independently of PBP2 (however, without actively influencing the sites of PBP2 binding itself, as shown in the previous paragraph).

The latter scenario would pose a strong constraint on the binding substrate: It would require that a fraction of binding sites at least as high as the persistent fraction of PBP2 molecules was occupied by MreB filaments. This scenario would thus require that the number of binding sites is not much higher than the number of MreB filaments in the cell envelope, but

still greater than the number of bound PBP2 molecules. With a conservative estimate of MreB filaments of about 200 per cell (Methods) and bound molecules of about 10-150 depending on expression and measurement method (Fig. 1–SI Fig. 7A), this constraint would require that the binding substrate is low-abundant. Alternatively, if MreB was recruited through bound PBP2 molecules, binding targets could be highly abundant.

None of the known Rod-complex components appears as the sole rate-limiting binding substrate for PBP2

To investigate the role of known Rod-complex components different from MreB as potential binding substrates for PBP2, we constructed depletion strains for RodA, RodZ, or MreCD in a background strain expressing either native levels of PAmCherry-PBP2 (for RodZ, MreCD) or overexpressing PAmCherry-PBP2 (for RodA). Without repression, almost all strains showed normal growth rate (Fig. 5–SI Fig. 1), cell shape (Fig. 5A, Fig. 5–SI Fig. 2A-B), bound fractions (Fig. 5C), and persistent fractions (Fig. 5D). Only the RodA-depletion strain showed longer cells and grew slightly slower than the wild type, in agreement with the growth rate of the overexpression strain (Fig. 1–SI Fig. 1C). Furthermore, the RodZ-depletion strain showed slightly higher bound and persistent fractions.

Within 6 h of depletion, cell shape was perturbed (Fig. 5B, Fig. 5–SI Fig. 2A-B), and repressed protein levels were reduced below wildtype levels (Fig. 5–SI Fig. 2C), while PBP2 levels remained close to initial levels (Fig. 5–SI Fig. 2D, Supplementary File 1b). Furthermore, growth rates were at most weakly reduced with respect to non-repressed conditions (Fig. 5–SI Fig.1).

Upon depletion of RodA or MreCD, bound fractions remained constant (Fig. 5C). According to previous measurements (Vigouroux et al., 2018), RodA was likely repressed by at least three-fold below levels of bound PBP2 molecules (Methods), suggesting that RodA is not the main binding substrate. Due to high residual levels of MreC and possibly high levels of undetected MreD it is possible that either or both of these proteins are required for PBP2 binding. However, constancy of the bound fraction despite a 2.3-fold reduction of MreCD levels with respect to MG1655, suggests that MreC and MreD are not rate-limiting for PBP2 binding.

Depletion of RodZ led to a significant reduction of the bound fraction (p-value = 0.021). At the same time, the persistent fraction remained high, which is compatible with observations of reduced but continued MreB motion (Dion et al., 2019). The drop of the bound fraction already occurred within two hours (Fig. 5–SI Fig. 2F), suggesting that RodZ modulates the rates of PBP2 binding or unbinding.

Despite the strong effect of RodZ depletion, multiple observations suggest that RodZ is not the sole rate-limiting substrate for PBP2 binding: First, the bound fraction increased after 6 h of depletion, despite a continued low level of RodZ (Fig. 5–SI Fig. 2C, F). Second, the

spatial pattern of RodZ but not of PBP2 depends on the presence of MreB filaments (Fig. 3), suggesting that the localization of PBP2 does also not depend on RodZ. Third, correlations between spatial patterns of mCherry-PBP2 and RodZ-GFP in cells expressing both fusions as sole copies of the respective proteins were low, in contrast to RodZ-GFP and MreB-mCherry (Fig. 5–SI Fig. 3) (Alyahya et al., 2009; Morgenstein et al., 2015).

Finally, *ponA* deletion (PBP1a) (Fig. 5) led to a drop of the bound fraction. Therefore, PBP1a is not required for PBP2 binding but might aid PBP2 binding or stabilize bound PBP2.

In conclusion, RodA and PBP1a are likely not the substrate for PBP2 binding, and we found evidence that neither MreCD nor RodZ are the sole rate-limiting substrate for PBP2.

MreB-curvature correlations are likely the result of persistent motion

Previously, Ursell et al. observed that MreB filaments were excluded from regions of positive Gaussian cell-envelope curvature such as found at the cell poles, while MreB was enriched in regions of negative Gaussian curvature as found at the inner sides of bent cells (Ursell et al., 2014). They concluded that the locations of Rod-complex activity are determined by MreB filaments preferentially localizing to sites of negative Gaussian curvature in rod-shaped cells (Ursell et al., 2014). This conclusion is in contradiction to our finding that PBP2 is responsible for the initial localization of new Rod complexes in the cylindrical part of the cell. However, MreB-curvature correlations could also come about indirectly through persistent rotational motion (Hussain et al., 2018; Wong et al., 2017, 2019) or additional mechanisms of polar exclusion (Kawazura et al., 2017), without any curvature-based Rod-complex initiation. To resolve this conflict, we reinvestigated MreB-curvature correlations and their potentially different origin.

We followed a very similar approach to (Ursell et al., 2014). Specifically, we measured the spatial pattern of MreB-msfGFP (Ouzounov et al., 2016) on the two-dimensional cell contour (Fig. 6A,B) both in filamentous cells, through expression of the division inhibitor SulA (Bi and Lutkenhaus, 1993), and in non-filamentous cells growing on agarose pads under the microscope. We obtained the contour curvature of the cell from phase-contrast images using the Morphometrics cell segmentation tool (Ursell et al., 2017, 2014). In cylindrical regions of normally growing or filamentous cells with low variations of cell diameter σ , contour curvature κ is a good proxy for Gaussian curvature G , with $G = 2 \kappa / \sigma$.

First, we measured the enrichment of MreB intensity at the cell contour as a function of local contour curvature, just like (Ursell et al., 2014) (Fig. 6C for filamentous cells; Fig. 6–SI Fig. 1 for wild-type cells). In quantitative agreement with their data we found enrichment of MreB at negative curvature and depletion at positive curvatures, as present at cell poles.

We then constrained our analysis to the cylindrical part of the cells and found that correlations were reduced by about five-fold at positive curvature values (Fig. 6C). These

findings demonstrate that the pattern of MreB localization is not simply a function of contour or Gaussian curvature. Instead, curvature correlations are qualitatively different at different parts of the cell and dominated by cell poles. On the contrary, correlations between MreB and contour curvature in the cylindrical part of the cell are weak.

In previous work by some of us (Wong et al., 2017) we found small but significant correlations between MreB and cell-centerline curvature in mechanically bent cells. We therefore wondered whether residual correlations between MreB and contour curvature in the cylindrical part of the cell observed here were dominated by weak cell bending (Fig. 6A) likely caused by cells attaching to the glass surface (Duvernoy et al., 2018). To that end we restricted our analysis to regions of the cell, where the spatially filtered cell centerline (using a Gauss filter of $\sigma = 80$ nm) was nearly straight (Fig. 6A). These regions still showed variations of cell-envelope curvature due to bulges or indentations (Fig. 6F). However, we did not find any significant correlations between MreB and contour curvature (Fig. 6D). Therefore, all residual MreB-curvature correlations after removal of poles and septa can be attributed to weak cell bending, while bending-independent bulges and indentations do not affect MreB localization.

We confirmed our findings with two alternative approaches: First, we subtracted from the local contour curvature the curvature contribution due to cell bending (Fig. 6–SI Fig. 2A-B). Residual curvature fluctuations originate from bulges or indentations. Consistently with our observation in straight cell segments, we found no significant correlations between MreB and corrected contour curvature. In an independent approach, we corrected MreB intensity values along the contours for the effect expected from cell-centerline bending (Fig. 6–SI Fig. 2C). Again, we did not find residual correlations after correction. Both of these analyses therefore strongly support the conclusion that spontaneous cell bending is responsible for all correlations between MreB and contour curvature in the cylindrical parts of normally growing cells.

Previously, we demonstrated that a small bending-induced enrichment of MreB can be explained by persistent rotational motion of MreB filaments (Wong et al., 2017), because rotating MreB filaments tend to accumulate at inner regions of bent cells. Our observations are therefore compatible with a model of MreB-independent initiation of Rod complexes through PBP2.

Diffusing PBP2 molecules do not contribute to Rod-complex activity

It was previously suggested that diffusive PBP2 molecules contribute to cell-wall synthesis (Lee et al., 2014). However, if diffusive PBP2 molecules indeed contributed to processive Rod-complex activity, any cross-linking site of a moving Rod complex would have to be found by independent PBP2 molecules through diffusion at a rate equal to the cross-linking

rate of up to 15/s. This rate corresponds to the distance between cross links of 2 nm (Meroueh et al., 2006) and a speed of PBP2 of 30 nm/s frequently observed (Fig. 1F).

To test whether PBP2 diffusion was fast enough for the biological cross-linking rate, we conducted computational simulations of freely diffusing PBP2 molecules and measured the average encounter rate between any simulated molecule and a given target site representing a Rod complex (Fig. 7A, B). We found that the rate between encounters was at least three times lower than the rate of cross-linking, even if a single enzyme had a high chance of returning to the same site and conduct multiple cross-linking reactions on average (Fig. 7C). Therefore, free diffusion cannot account for physiological cross-linking rates.

As an extension of the model we considered the possibility that PBP2 molecules underwent facilitated diffusion by preferentially diffusing along MreB filaments, which could possibly serve to increase encounter rates between PBP2 and cell-wall-insertion sites. One-dimensional diffusion along filaments indeed increased the encounter rate (Fig. 7D). However, due to the preferentially circumferential orientation of MreB filaments, facilitated diffusion would also lead to reduced and asymmetric diffusion (Fig. 7E). On the contrary, we did not observe increased diffusion around the circumference (Fig. 7F). Therefore, Rod-complex activity requires the stable association between transglycosylase and transpeptidase for multiple cross-linking events. Our findings suggest, that only the persistently moving fraction of PBP2 molecules substantially contributes to cross-linking.

Discussion

In summary, we found an important role of PBP2 for Rod-complex initiation and persistent cell-wall synthetic activity. New Rod complexes are initiated once PBP2 binds to an immobile substrate in the cell envelope that is different from MreB filaments. Furthermore, we found evidence that none of the known Rod-complex components provides the sole rate-limiting binding substrate for PBP2.

PBP2 might bind directly to the cell wall

Based on our observations we speculated that PBP2 might bind to the cell wall directly. Support for this viewpoint comes from the diffusive motion of PBP2 molecules. PBP2 diffusion is much slower than diffusion of similar-size membrane proteins (Kumar et al., 2010) or of a truncated version of PBP2 (Lee et al., 2014), suggesting that PBP2 might weakly bind the cell wall even during diffusion (Lee et al., 2014). We found that depletion of RodA, RodZ, and MreCD caused an additional decrease of the diffusion constant (Fig. 5–SI Fig. 2E), similarly to long-term treatment with A22 or Mecillinam (Fig. 3E). In all cases, Rod-complex activity is inhibited or reduced, which changes cell-wall architecture (Wang et al., 2012) and reduces the degree of cross-linking (Uehara and Park, 2008). These observations support the model that diffusion is governed by the physical interactions between PBP2 and

the cell wall (Lee et al., 2014). Interestingly, overexpression of PBP2 also led to a reduction of the diffusion constant (Fig. 1–SI Fig. 2). To determine whether this reduction is due to an alteration of the cell-wall structure or due to a different cause, will require further investigation.

Cell-wall architecture and not envelope curvature likely provides the signal for Rod-complex initiation

It has been proposed that Rod complexes are recruited to sites of specific cell-envelope curvature based on mechanical properties of MreB (Ursell et al., 2014). We found that correlations between MreB filaments and cell-envelope curvature in normally growing rods do not require any curvature-dependent initiation of Rod complexes. This observation does not rule out that MreB-curvature correlations in cells of strongly perturbed shape might be influenced by MreB-filament bending or twisting (Bratton et al., 2018; Colavin et al., 2018). Evidence for motion-independent curvature preferences comes from *C. crescentus* (Harris et al., 2014). However, our study as well as previous studies (Hussain et al., 2018; Wong et al., 2017, 2019) suggest that MreB-filament rotation around the circumference are responsible for MreB-curvature correlations in wild-type and filamentous cells. Therefore, the physical signal underlying the spatial pattern of new Rod complexes is likely found in the local architecture of the cell wall, and not, as previously suggested, in the geometry of the cytoplasmic membrane.

What is the PBP2-binding substrate?

The bound fraction of PBP2 molecules remained nearly constant upon A22 or Mecillinam treatment (Fig. 3). We thus reasoned that persistently moving and immobile molecules are likely bound to the same substrate. In Gram-negative *E. coli*, active Rod complexes are thought to insert nascent glycan strands in between template strands (Höltje, 1998), even if deviations from perfect alignment are reported (Turner et al., 2018). During cell-wall insertion, Rod complexes might therefore stay connected to the local cell wall through associations between PBP2 and a template strand, independently of enzymatic activity. In the future, it will be interesting to study potential interactions at the molecular level. These might then also reveal structural features of the cell wall potentially responsible for stable PBP2 association.

What determines the rates of binding and unbinding?

PBP2 molecules transition only slowly between bound and diffusive states (Fig. 2). Possibly, PBP2 is found in two different molecular states that facilitate stable binding or allow for diffusive motion – either through conformational change or through interaction with an unknown interaction partner. Depletion experiments with RodA through CRISPRi suggest

that RodA is not involved in this process, since RodA levels were likely repressed below the levels of bound PBP2. Depletion experiments with MreCD and RodZ suggest that none of these proteins constitutes the sole rate-limiting binding substrate. However, residual protein levels upon depletion were too high to rule out an important and possibly essential role for PBP2 binding. Specifically, RodZ depletion led to a reduction of the bound fraction, suggesting that RodZ directly modulates PBP2 binding or the stability of the bound form of PBP2. This is compatible with previous observations of RodZ-PBP2 interactions (Bendezú et al., 2009; Morgenstein et al., 2015). It will thus be interesting to investigate the role of RodZ for PBP2 binding or unbinding in more detail in the future.

How do MreB filaments 'find' the binding substrate?

We reasoned that MreB filaments must either be recruited to bound PBP2 molecules or to an unknown, low-abundant binding substrate. To find its target, MreB filaments could explore the cell envelope through rapid diffusive motion previously overlooked. Alternatively, the binding target could nucleate new MreB filaments. Other Rod-complex components such as RodZ could facilitate this process. This latter hypothesis is supported by the recent observation that the hyperactive PBP2(L61R) mutant described above causes more and shorter MreB filaments (Rohs et al., 2018).

High residual Rod-complex activity upon PBP2 overexpression suggests that PBP2 activates the Rod complex

We observed that the fraction of bound PAmCherry-PBP2 molecules decreased by about two-fold upon three-fold increase of enzyme levels. Together with a nearly constant fraction of persistently moving molecules, this suggests that the number of active enzymes increases about two-fold (Supplementary File 1a). Therefore, PBP2 appears to be an important limiting factor for Rod-complex activity. This finding is consistent with the previous observation that PBP2 activates RodA (Rohs et al., 2018).

For the msfGFP-fusion we observed that the decrease of the bound fraction was roughly inversely proportional to expression level up to 5 μ M IPTG (Supplementary File 1a). However, while this level of induction lead to wild-type levels of enzymes on average, it still led to a time-dependent change of cell shape and bound fraction. The quantitative interpretation of this result is therefore difficult.

Both fusions suggest that PBP2 abundance might not be the sole limiting factor for PBP2 binding and Rod-complex activity, and we already found two qualitatively different limiting factors: RodZ has a strong effect on PBP2 binding, possibly by facilitating binding or by stabilizing the bound fraction, while RodA and MreCD have seemingly no effect on binding but an important limiting role for persistent motion.

520 ***Rod-complex activity and cell shape***

521 Despite the substantial residual degree of persistent motion upon depletion of MreCD,
522 RodA, or RodZ, the presence of all these components is required to stably maintain rod
523 shape. A recent paper suggested that cell diameter in *E. coli* is partially determined by the
524 spatial density of active Rod complexes (Dion et al., 2019). The model is compatible with the
525 fold-change of persistently moving PBP2 molecules and cell-diameter changes observed
526 during MreCD and RodZ depletion. However, during RodA-depletion this simple model does
527 not apply: Due to overexpression of PBP2, the total number of persistently moving PBP2
528 molecules per cell is likely as high as in the wildtype – even during RodA depletion. In the
529 future, it will therefore be interesting to study how the stoichiometry of different Rod-complex
530 components affects cell-wall insertion and cell shape.

531 **Acknowledgements**

532 We thank Timothy Lee and KC Huang for strain TKL130 and plasmid pKC128, Nikolay
533 Ouzounov and Zemer Gitai for strains NO50 and NO53, Tom Bernhardt for strains
534 TU230(attLHC943) and TU230(attLPR122), Felipe Bendezú and Piet de Boer for plasmids
535 pFB121, pFB290 and strain FB60(iFB273). This work was supported by the European
536 Research Council (ERC) under the Europe Union's Horizon 2020 research and innovation
537 program [Grant Agreement No. (679980)], the French Government's Investissement d'Avenir
538 program Laboratoire d'Excellence “Integrative Biology of Emerging Infectious Diseases”
539 (ANR-10-LABX-62-IBEID), the Mairie de Paris “Emergence(s)” program, the PRESTIGE
540 Postdoc fellowship (Campus France), and the Volkswagen Foundation.

- 542 Alyahya, S.A., Alexander, R., Costa, T., Henriques, A.O., Emonet, T., and Jacobs-Wagner,
543 C. (2009). RodZ, a component of the bacterial core morphogenic apparatus. *Proceedings of*
544 *the National Academy of Sciences* 106, 1239–1244.
- 545 Banzhaf, M., van den Berg van Saparoea, B., Terrak, M., Fraipont, C., Egan, A., Philippe, J.,
546 Zapun, A., Breukink, E., Nguyen-Disteche, M., den Blaauwen, T., et al. (2012). Cooperativity
547 of peptidoglycan synthases active in bacterial cell elongation. *Molecular Microbiology* 85,
548 179–194.
- 549 Bendezú, F.O., Hale, C.A., Bernhardt, T.G., and de Boer, P.A.J. (2009). RodZ (YfgA) is
550 required for proper assembly of the MreB actin cytoskeleton and cell shape in *E. coli*. *The*
551 *EMBO Journal* 28, 193–204.
- 552 Bi, E., and Lutkenhaus, J. (1993). Cell division inhibitors SulA and MinCD prevent formation
553 of the FtsZ ring. *J. Bacteriol.* 175, 1118–1125.
- 554 Billaudeau, C., Yao, Z., Cornilleau, C., Carballido-López, R., and Chastanet, A. (2019). MreB
555 Forms Subdiffraction Nanofilaments during Active Growth in *Bacillus subtilis*. *MBio* 10,
556 e01879-18.
- 557 Billings, G., Ouzounov, N., Ursell, T., Desmarais, S.M., Shaevitz, J., Gitai, Z., and Huang,
558 K.C. (2014). De novomorphogenesis in L-forms via geometric control of cell growth.
559 *Molecular Microbiology* 93, 883–896.
- 560 Bratton, B.P., Shaevitz, J.W., Gitai, Z., and Morgenstein, R.M. (2018). MreB polymers and
561 curvature localization are enhanced by RodZ and predict *E. coli*'s cylindrical uniformity.
562 *Nature Communications* 9, 2797.
- 563 Cho, H., Wivagg, C.N., Kapoor, M., Barry, Z., Rohs, P.D.A., Suh, H., Marto, J.A., Garner,
564 E.C., and Bernhardt, T.G. (2016). Bacterial cell wall biogenesis is mediated by SEDS and
565 PBP polymerase families functioning semi-autonomously. *Nat. Microbiol* 1, 16172–16172.
- 566 Colavin, A., Shi, H., and Huang, K.C. (2018). RodZ modulates geometric localization of the
567 bacterial actin MreB to regulate cell shape. *Nature Communications* 9, 1280.
- 568 Contreras-Martel, C., Martins, A., Ecobichon, C., Trindade, D.M., Matteï, P.-J., Hicham, S.,
569 Hardouin, P., Ghachi, M.E., Boneca, I.G., and Dessen, A. (2017). Molecular architecture of
570 the PBP2–MreC core bacterial cell wall synthesis complex. *Nature Communications* 8, 776.
- 571 Dion, M.F., Kapoor, M., Sun, Y., Wilson, S., Ryan, J., Vigouroux, A., Teeffelen, S. van,
572 Oldenbourg, R., and Garner, E.C. (2019). *Bacillus subtilis* cell diameter is determined by the
573 opposing actions of two distinct cell wall synthetic systems. *Nature Microbiology* 1.
- 574 Duvernoy, M.-C., Mora, T., Ardré, M., Croquette, V., Bensimon, D., Quilliet, C., Ghigo, J.-M.,
575 Balland, M., Beloin, C., Lecuyer, S., et al. (2018). Asymmetric adhesion of rod-shaped
576 bacteria controls microcolony morphogenesis. *Nature Communications* 9, 1120.
- 577 Dye, N.A., Pincus, Z., Theriot, J.A., Shapiro, L., and Gitai, Z. (2005). Two independent spiral
578 structures control cell shape in *Caulobacter*. *Proc Natl Acad Sci USA* 102, 18608–18613.
- 579 Emami, K., Guyet, A., Kawai, Y., Devi, J., Wu, L.J., Allenby, N., Daniel, R.A., and Errington,
580 J. (2017). RodA as the missing glycosyltransferase in *Bacillus subtilis* and antibiotic
581 discovery for the peptidoglycan polymerase pathway. *Nature Microbiology* 2, 16253.
- 582 Errington, J. (2015). Bacterial morphogenesis and the enigmatic MreB helix. *Nature Reviews*
583 *Microbiology* 13, 241–248.

584 Gitai, Z. (2005). The new bacterial cell biology: moving parts and subcellular architecture.
585 *Cell* 120, 577–586.

586 Hansen, A.S., Woringer, M., Grimm, J.B., Lavis, L.D., Tjian, R., and Darzacq, X. (2018).
587 Robust model-based analysis of single-particle tracking experiments with Spot-On. *ELife* 7,
588 e33125.

589 Harris, L.K., Dye, N.A., and Theriot, J.A. (2014). A *Caulobacter* MreB mutant with irregular
590 cell shape exhibits compensatory widening to maintain a preferred surface area to volume
591 ratio. *Molecular Microbiology* 94, 988–1005.

592 Hocking, J., Priyadarshini, R., Takacs, C.N., Costa, T., Dye, N.A., Shapiro, L., Vollmer, W.,
593 and Jacobs-Wagner, C. (2012). Osmolality-dependent relocation of penicillin-binding protein
594 PBP2 to the division site in *Caulobacter crescentus*. *Journal of Bacteriology* 194, 3116–
595 3127.

596 Höltje, J.V. (1998). Growth of the stress-bearing and shape-maintaining murein sacculus of
597 *Escherichia coli*. *Microbiology and Molecular Biology Reviews* 62, 181–203.

598 Hussain, S., Wivagg, C.N., Szwedziak, P., Wong, F., Schaefer, K., Izoré, T., Renner, L.D.,
599 Holmes, M.J., Sun, Y., Bisson-Filho, A.W., et al. (2018). MreB filaments align along greatest
600 principal membrane curvature to orient cell wall synthesis. *ELife Sciences* 7, e32471.

601 Kawazura, T., Matsumoto, K., Kojima, K., Kato, F., Kanai, T., Niki, H., and Shiomi, D. (2017).
602 Exclusion of assembled MreB by anionic phospholipids at cell poles confers cell polarity for
603 bidirectional growth. *Molecular Microbiology* 104, 472–486.

604 Kruse, T., Bork-Jensen, J., and Gerdes, K. (2004). The morphogenetic MreBCD proteins of
605 *Escherichia coli* form an essential membrane-bound complex. *Molecular Microbiology* 55,
606 78–89.

607 Kumar, M., Mommer, M.S., and Sourjik, V. (2010). Mobility of Cytoplasmic, Membrane, and
608 DNA-Binding Proteins in *Escherichia coli*. *Biophysical Journal* 98, 552–559.

609 Lee, T.K., Tropini, C., Hsin, J., Desmarais, S.M., Ursell, T.S., Gong, E., Gitai, Z., Monds,
610 R.D., and Huang, K.C. (2014). A dynamically assembled cell wall synthesis machinery
611 buffers cell growth. *Proceedings of the National Academy of Sciences* 111, 4554–4559.

612 Manley, S., Gillette, J.M., Patterson, G.H., Shroff, H., Hess, H.F., Betzig, E., and Lippincott-
613 Schwartz, J. (2008). High-density mapping of single-molecule trajectories with
614 photoactivated localization microscopy. *Nature Methods* 5, 155–157.

615 Meeske, A.J., Riley, E.P., Robins, W.P., Uehara, T., Mekalanos, J.J., Kahne, D., Walker, S.,
616 Kruse, A.C., Bernhardt, T.G., and Rudner, D.Z. (2016). SEDS proteins are a widespread
617 family of bacterial cell wall polymerases. *Nature* 537, 634–638.

618 Morgenstein, R.M., Bratton, B.P., Nguyen, J.P., Ouzounov, N., Shaevitz, J.W., and Gitai, Z.
619 (2015). RodZ links MreB to cell wall synthesis to mediate MreB rotation and robust
620 morphogenesis. *Proceedings of the National Academy of Sciences* 112, 12510–12515.

621 Olshausen, P. v, Defeu Soufo, H.J., Wicker, K., Heintzmann, R., Graumann, P.L., and
622 Rohrbach, A. (2013). Superresolution Imaging of Dynamic MreB Filaments in *B. subtilis*—A
623 Multiple-Motor-Driven Transport? *Biophysical Journal* 105, 1171–1181.

624 Ouzounov, N., Nguyen, J.P., Bratton, B.P., Jacobowitz, D., Gitai, Z., and Shaevitz, J.W.
625 (2016). MreB Orientation Correlates with Cell Diameter in *Escherichia coli*. *Biophysical*
626 *Journal* 111, 1035–1043.

627 Rohs, P.D.A., Buss, J., Sim, S.I., Squyres, G.R., Srisuknimit, V., Smith, M., Cho, H., Sjødt,
628 M., Kruse, A.C., Garner, E.C., et al. (2018). A central role for PBP2 in the activation of

629 peptidoglycan polymerization by the bacterial cell elongation machinery. *PLOS Genetics* 14,
630 e1007726.

631 Salje, J., van den Ent, F., de Boer, P., and Löwe, J. (2011). Direct Membrane Binding by
632 Bacterial Actin MreB. *Molecular Cell* 43, 478–487.

633 Shi, H., Bratton, B.P., Gitai, Z., and Huang, K.C. (2018). How to Build a Bacterial Cell: MreB
634 as the Foreman of *E. coli* Construction. *Cell* 172, 1294–1305.

635 Shiomi, D., Sakai, M., and Niki, H. (2008). Determination of bacterial rod shape by a novel
636 cytoskeletal membrane protein. *The EMBO Journal* 27, 3081–3091.

637 Spratt, B.G. (1975). Distinct penicillin binding proteins involved in the division, elongation,
638 and shape of *Escherichia coli* K12. *Proc Natl Acad Sci USA* 72, 2999–3003.

639 Strahl, H., Bürmann, F., and Hamoen, L.W. (2014). The actin homologue MreB organizes
640 the bacterial cell membrane. *Nat Commun* 5, 3442–3442.

641 Surovtsev, I.V., and Jacobs-Wagner, C. (2018). Subcellular Organization: A Critical Feature
642 of Bacterial Cell Replication. *Cell* 172, 1271–1293.

643 van Teeffelen, S., Wang, S., Furchtgott, L., Huang, K.C., Wingreen, N.S., Shaevitz, J.W.,
644 and Gitai, Z. (2011). The bacterial actin MreB rotates, and rotation depends on cell-wall
645 assembly. *Proceedings of the National Academy of Sciences* 108, 15822–15827.

646 Turner, R.D., Mesnage, S., Hobbs, J.K., and Foster, S.J. (2018). Molecular imaging of
647 glycan chains couples cell-wall polysaccharide architecture to bacterial cell morphology.
648 *Nature Communications* 9, 1263.

649 Typas, A., Banzhaf, M., Gross, C.A., and Vollmer, W. (2012). From the regulation of
650 peptidoglycan synthesis to bacterial growth and morphology. *Nat Rev Microbiol* 10, 123–
651 136.

652 Uehara, T., and Park, J.T. (2008). Growth of *Escherichia coli*: Significance of Peptidoglycan
653 Degradation during Elongation and Septation. *Journal of Bacteriology* 190, 3914–3922.

654 Ursell, T., Lee, T.K., Shiomi, D., Shi, H., Tropini, C., Monds, R.D., Colavin, A., Billings, G.,
655 Bhaya-Grossman, I., Broxton, M., et al. (2017). Rapid, precise quantification of bacterial
656 cellular dimensions across a genomic-scale knockout library. *BMC Biology* 15, 17.

657 Ursell, T.S., Nguyen, J., Monds, R.D., Colavin, A., Billings, G., Ouzounov, N., Gitai, Z.,
658 Shaevitz, J.W., and Huang, K.C. (2014). Rod-like bacterial shape is maintained by feedback
659 between cell curvature and cytoskeletal localization. *Proceedings of the National Academy*
660 *of Sciences* 111, E1025-34.

661 Vigouroux, A., Oldewurtel, E., Cui, L., Bikard, D., and Teeffelen, S. van (2018). Tuning
662 dCas9's ability to block transcription enables robust, noiseless knockdown of bacterial
663 genes. *Molecular Systems Biology* 14, e7899.

664 Vollmer, W., Blanot, D., and de Pedro, M.A. (2008). Peptidoglycan structure and
665 architecture. *FEMS Microbiol Rev* 32, 149–167.

666 Wang, S., and Wingreen, N.S. (2013). Cell shape can mediate the spatial organization of the
667 bacterial cytoskeleton. *Biophysical Journal* 104, 541–552.

668 Wang, S., Furchtgott, L., Huang, K.C., and Shaevitz, J.W. (2012). Helical insertion of
669 peptidoglycan produces chiral ordering of the bacterial cell wall. *Proceedings of the National*
670 *Academy of Sciences* 109, E595-604.

671 Wong, F., Renner, L.D., Özbaykal, G., Paulose, J., Weibel, D.B., Teeffelen, S. van, and
672 Amir, A. (2017). Mechanical strain sensing implicated in cell shape recovery in *Escherichia*
673 *coli*. *Nature Microbiology* 2, 17115.

674 Wong, F., Garner, E.C., and Amir, A. (2019). Mechanics and dynamics of translocating MreB
675 filaments on curved membranes. *ELife* 8, e40472.

676

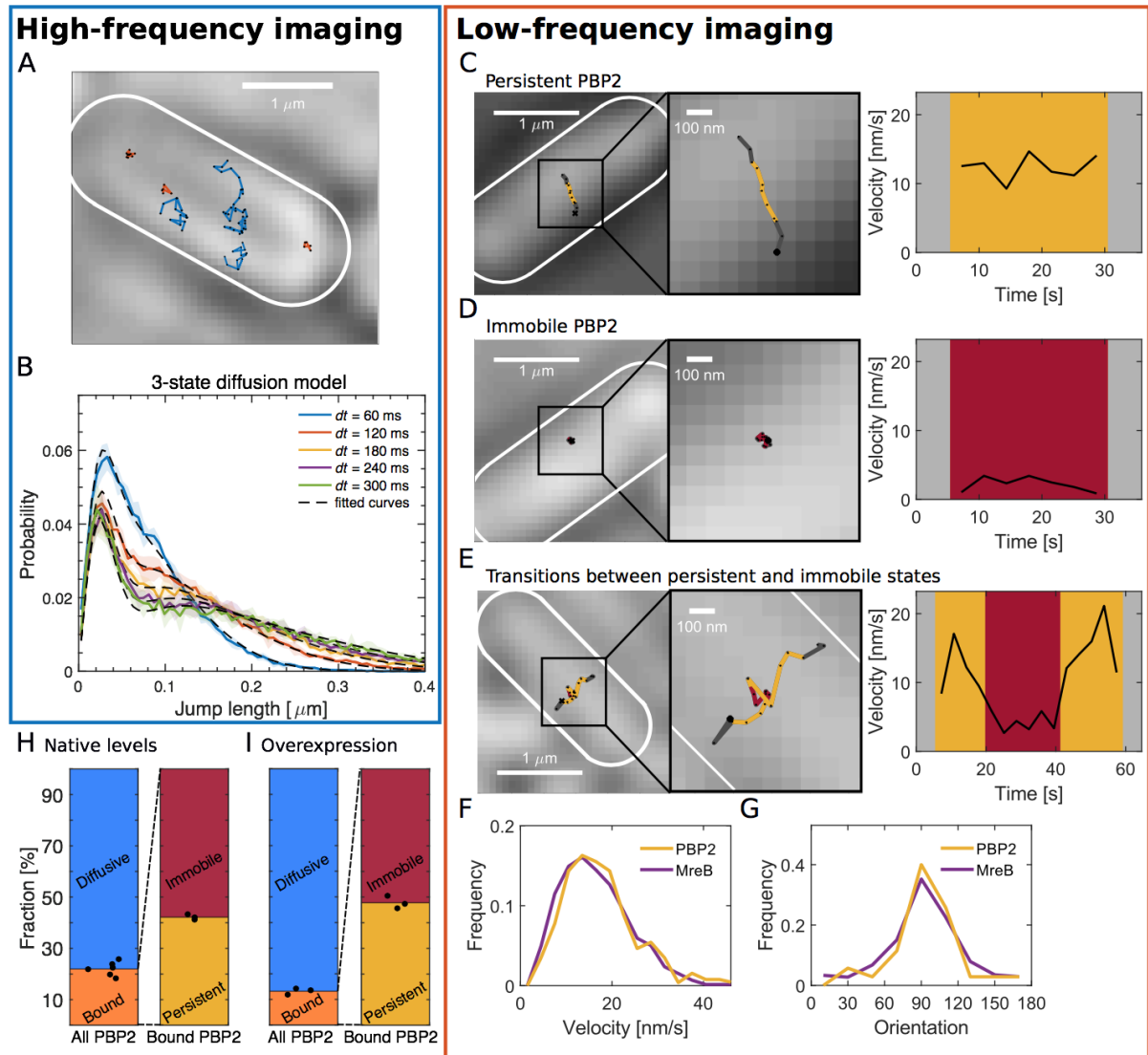


Figure 1. PBP2 molecules reside in diffusive, immobile, or persistently moving states.

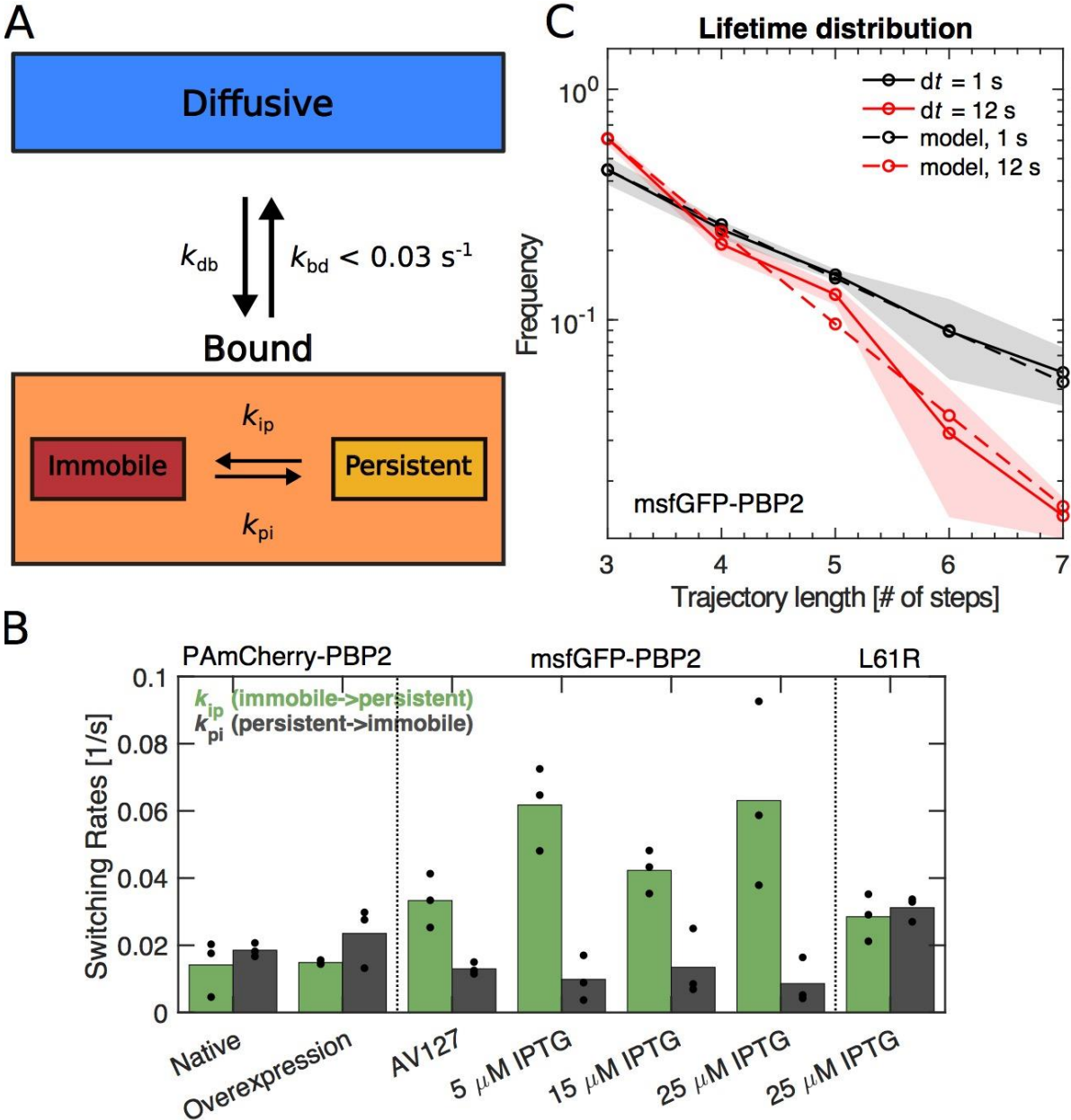
(A) Representative trajectories of PAmCherry-PBP2 molecules (TKL130) obtained by high-frequency imaging (time interval 60 ms) reveals diffusive (blue) and bound (orange) molecules.

(B) Probability distribution of single-molecule jump lengths (solid lines, colored) and fit (dashed, black) using a three-state-diffusion model for different time intervals. 78% of PBP2 move diffusively with $\langle D \rangle = 0.042 \mu\text{m}^2/\text{s}$ while 22% are immobile. The shaded area indicates standard deviation between 6 biological replicates.

(C-E) Low-frequency imaging (3.6 s with 1 s exposure time) reveals that bound PBP2 molecules are either persistently moving **(C)** or immobile **(D)**, according to the instantaneous PBP2 velocity. PBP2 molecules show transitions between persistent and immobile states **(E)**.

(F-G) Persistently moving PBP2 and MreB filaments show similar speeds **(F)** and orientations of motion (orientation measured with respect to the cell centerline) **(G)**.

(H-I) Average fractions of bound, diffusive, persistently moving, and immobile PAmCherry-PBP2 at native levels (TKL130) **(H)** or if overexpressed (TKL130/pKC128) **(I)**. Dots show biological replicates.



696

697 **Figure 2. PBP2 molecules transition between different dynamic states.**

698 **(A)** Diagram illustrating transition rates measured between different motion states.

699 **(B)** Transition rates between immobile and persistently moving states for different protein
700 fusions and expression levels. Circles: biological replicates.

701 **(C)** Fluorescence-lifetime distributions of msfGFP-PBP2 trajectories with imaging intervals of
702 1 s (black solid line) and 12 s (red solid line). Dashed lines represent a joint fit of the two
703 curves to a model of photobleaching and bleaching-independent track termination, the latter
704 comprising unbinding and persistently molecules leaving the TIR field of view (bleaching
705 probability per frame $p_b = 0.39 \pm 0.08$, apparent track termination rate $k_a = 0.035 \pm 0.007 \text{ s}^{-1}$).
706 Based on a model for persistent motion, we obtained an upper limit of the unbinding rate of
707 $k_{bd} < 0.03/\text{s}$ (Fig. 2–SI Fig. 1). Shaded region: Standard deviation between at least 3
708 technical replicates.

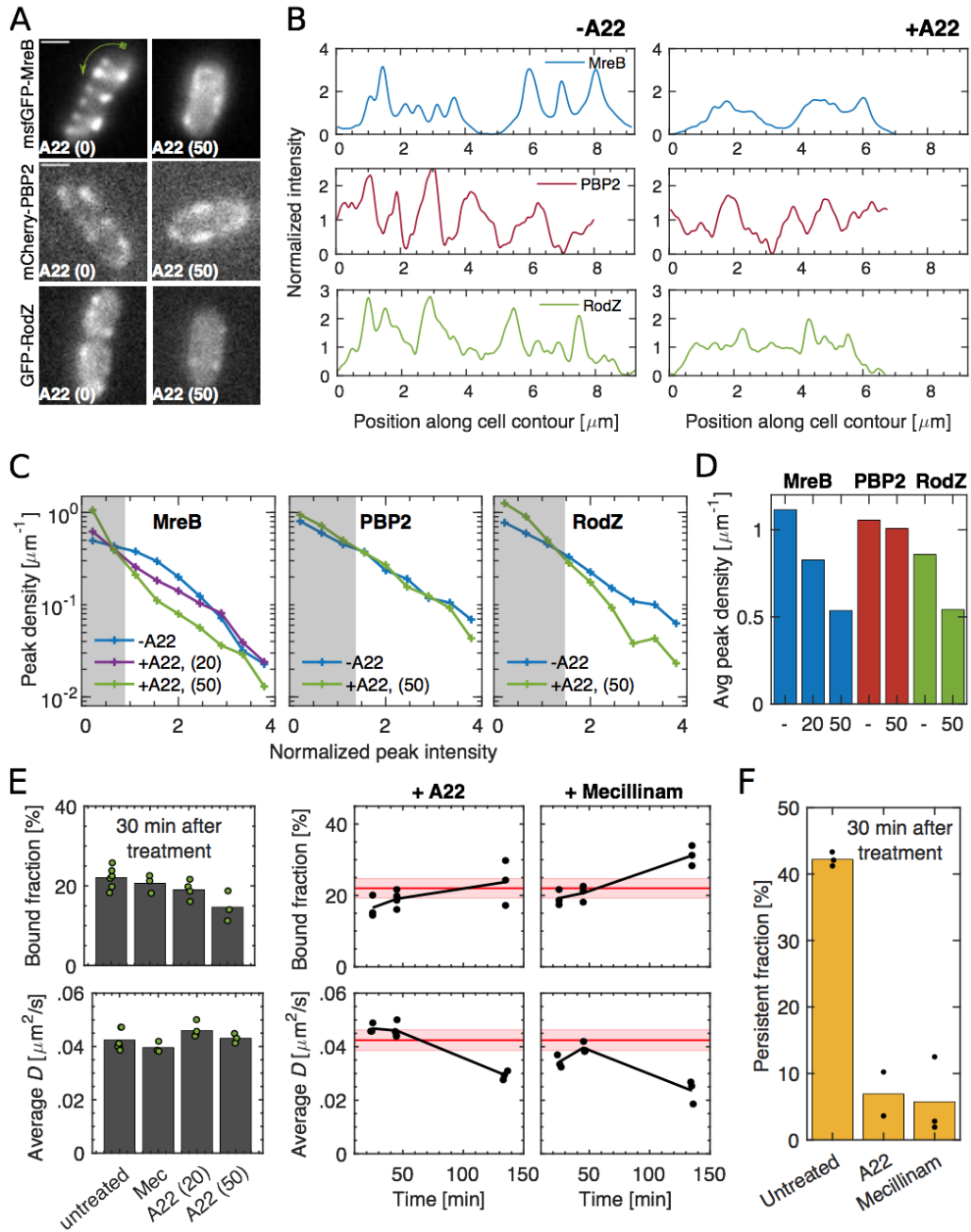


Figure 3. Spatial distribution and magnitude of PBP2 bound fraction are independent of MreB cytoskeleton.

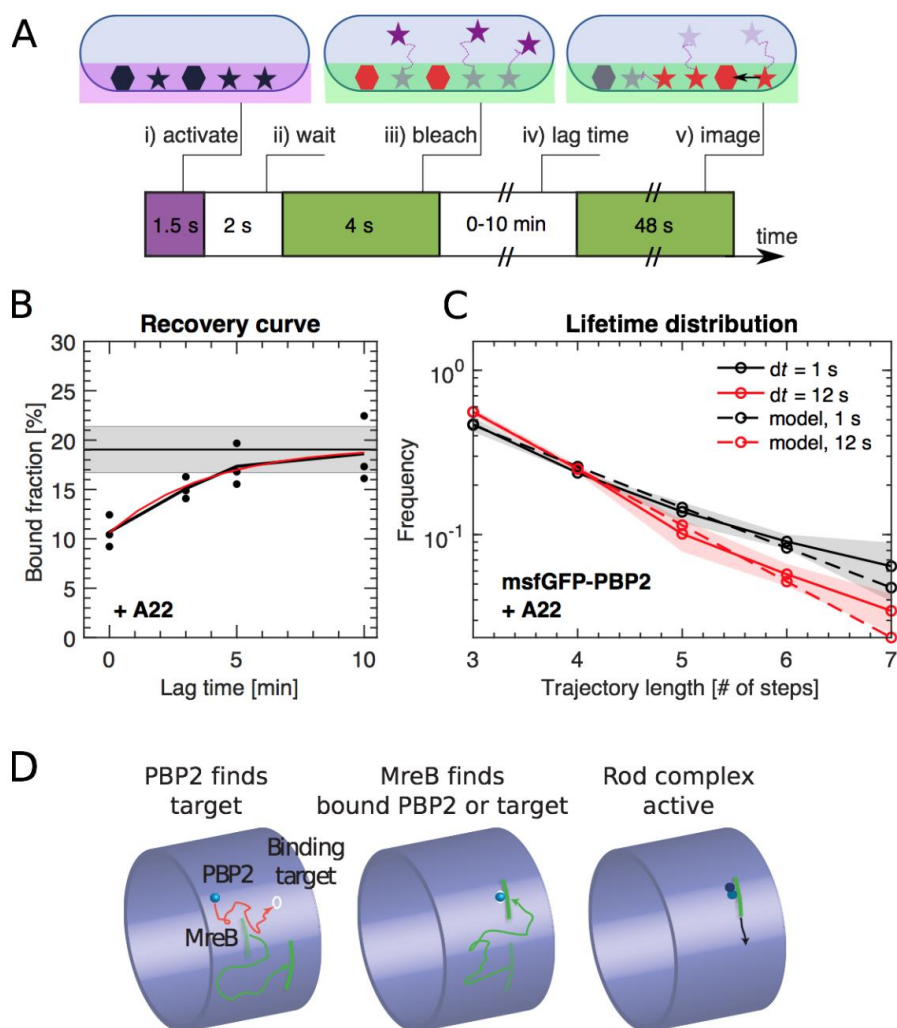
(A-B) 30-min A22 treatment (50 $\mu\text{g/ml}$) visibly reduces peak number and intensity of MreB-msfGFP and GFP-RodZ but not of mCherry-PBP2 on cell boundaries, as seen in epifluorescence images (A) and in line profiles measured along the cell contour (B), starting from one cell pole at $x=0$ as indicated by the green arrow in (A). Image exposure time 1 s. Scale bar 1 μm .

(C) Peak density on the cell boundary [$1/\mu\text{m}$] as function of peak intensity for two A22 concentrations (20, 50 $\mu\text{g/ml}$). Intensities are normalized by median peak intensity in untreated cells. Gray regions: peaks within noise floor.

(D) Density of all peaks above noise floor in (A) for untreated and A22-treated conditions.

(E) Left. Bound fraction and diffusion constant of PAmCherry-PBP2 30 minutes after drug treatment with mecillinam (labeled 'Mec', 100 $\mu\text{g/ml}$) or A22 (20 or 50 $\mu\text{g/ml}$). Right. Bound fraction and diffusion constant over time after treatment with A22 (20 $\mu\text{g/ml}$) or mecillinam (100 $\mu\text{g/ml}$). Dots indicate technical replicates. Red lines and shaded areas: Average values and standard deviations between biological replicates from untreated cells.

(F) Persistent fractions corresponding to the 30 min time point in (E).



728

729

730 **Figure 4. PBP2 slowly transitions between diffusive and bound states.**

731 **(A)** Bound-Molecule-FRAP reveals rate of PAmCherry-PBP2 binding k_{db} : i) Diffusive (stars)
 732 and bound (hexagons) molecules are activated at bottom of cell through TIR illumination. ii)
 733 Most activated diffusive molecules (purple) leave the field of view. iii) Remaining molecules
 734 are bleached (red). iv) Activated diffusive molecules partially return into the field of view,
 735 where they can bind (black arrow). v) Measurement of bound fraction.

736 **(B)** Bound fraction according to (A) at different lag times. Black horizontal line and shaded
 737 area: bound fraction without bleaching and standard deviation from technical replicates. An
 738 exponential fit in the form $b(t) = a_1 - a_2 \exp[-k_{db} t]$ (red line) yields binding rate $k_{db} = (4.3 \pm$
 739 $2) \times 10^{-3} \text{ s}^{-1}$. Dots represent technical replicates. Shaded area shows standard deviation
 740 between 6 biological replicates.

741 **(C)** Fluorescence-lifetime distributions of msfGFP-PBP2 tracks in A22-treated cells with
 742 imaging intervals of 1 s (black solid line) and 12 s (red solid line) yields unbinding rate $k_{bd} =$
 743 $0.02 \pm 0.01 \text{ s}^{-1}$. Shaded area shows standard deviation between at least 3 technical
 744 replicates.

745 **(D)** Cartoon of suggested Rod-complex initiation: PBP2 (blue) binds to a target site in the
 746 cell envelope (white circle) independently of MreB filaments or PBP2 activity. PBP2 or the
 747 target site then recruits an MreB filament through diffusion and capture (green) or through
 748 nucleation, and also recruits other rod-complex components (magenta).

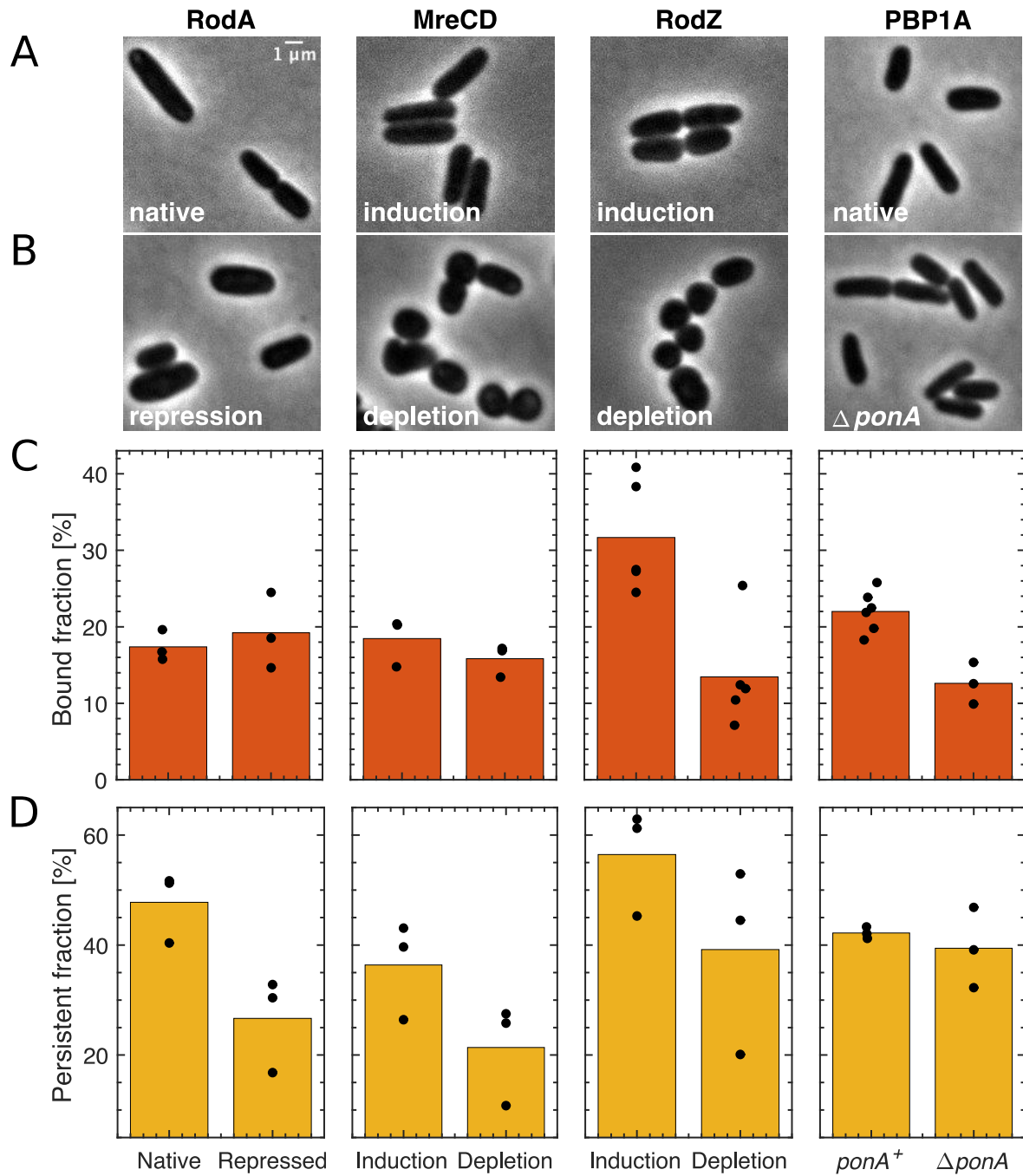


Figure 5. Depletion of known rod-complex components only weakly affects PBP2 binding.

(A-B) Cell shape upon near-native expression (A) or long-time depletion (B) of RodA, MreCD, RodZ, or PBP1a. RodA was repressed for 9h through CRISPRi against *mrdAB* operon (coding for PBP2 and RodA) in AV48/pKC128 [*P_{mrdA}::PamCherry-PBP2*]. Here, PBP2 was 2-5-fold overexpressed from plasmid pKC128 to avoid PBP2 depletion upon *mrdAB* repression. MreCD was depleted for 6h in TKL130 Δ *mreCD*/pFB121 [*P_{lac}::mreCD*]. RodZ was depleted for 6h in TKL130 Δ *rodZ*/pFB290 [*P_{lac}::rodZ*]. PBP1a is not essential and was deleted. In all cases except for PBP1A, cells loose rod-like cell shape.

(C-D) Bound fractions (C) and persistent fractions (D) of PAmCherry-PBP2 upon expression or depletion of proteins indicated above (A). Dots represent biological replicates.

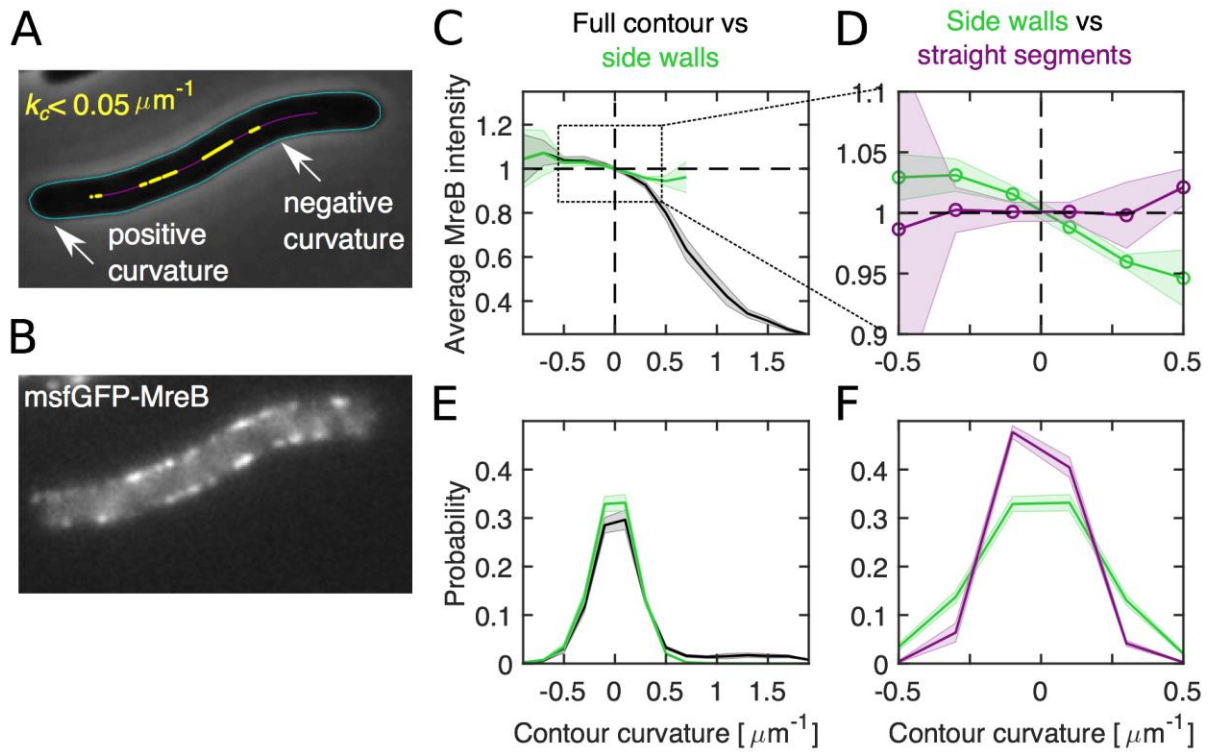


Figure 6. Differential MreB-curvature correlations in filamentous cells are due to cell poles and cell bending.

(A-B) Phase-contrast image **(A)** and fluorescence intensity **(B)** of a representative filamentous *E. coli* expressing MreB-msfGFP and Sula (NO53/pDB192). Contours (cyan) are obtained by computational cell segmentation. Positive contour curvature is found at cell poles, bulges, and outer parts of spontaneously bent regions, while negative curvature is found at indentations and inner parts of bent regions. Straight cell segments (yellow) are defined as regions where the curvature of the spatially averaged centerline (magenta) is smaller than $0.05 \mu\text{m}^{-1}$.

(C-D) Normalized average MreB intensity as a function of local contour curvature. Comparison between correlations obtained from full contours (black) and side walls (green) **(C)** and from side walls (green) and straight cell segments (magenta) **(D)**.

(E-F) Distributions of contour-curvature values corresponding to correlation plots in **(C-D)**. Shaded region: Standard deviation between 3 biological replicates.

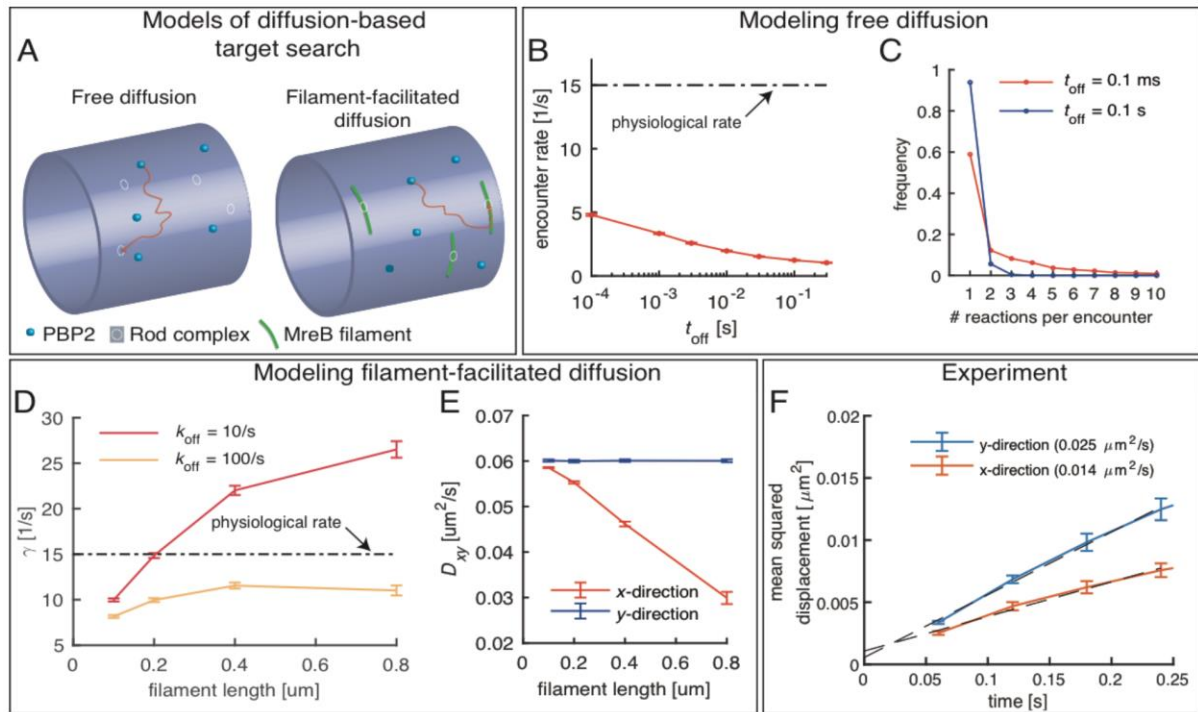


Figure 7. Testing a possible role of diffusive PBP2 for cross-linking.

(A) Cartoon of PBP2 finding the target site of a 'rod complex' through free diffusion (left) or filament-facilitated diffusion (right).

(B) The average encounter rate between any of 100 freely diffusing PBP2 molecules and a given rod-complex site as a function of the unknown latency time t_{off} (the duration for which a single PBP2 enzyme is inactive after a cross-linking reaction) (red) in comparison to the physiological cross-linking rate (dashed-dotted line) **(C)** Distribution of the number of successive cross-linking reactions conducted by the same PBP2 molecule at the same rod-complex site for two different latency times.

(D-E) Facilitated diffusion along circumferentially oriented filaments centered at every rod-complex site increases the encounter rate **(D)** and renders diffusion asymmetric **(E)**.

(F) Diffusion of PAmCherry-PBP2 is along the long axis of the cell (x-direction) is not faster than around the circumference (y-direction), suggesting that PBP2 does not undergo facilitated diffusion along circumferentially oriented filaments. Reduced diffusion around the circumference is possibly caused by out-of-plane motion.

794 Table of contents

795	1.	Key Resources Table	29
796	2.	Strain construction	30
797	3.	Bocillin labelling.....	31
798	4.	Sample preparation and imaging conditions	31
799	5.	Microscopy	32
800	6.	Cell segmentation	33
801	7.	PBP2 tracking.....	34
802	8.	MreB tracking	34
803	9.	Curvature analysis and MreB-curvature correlations.....	35
804	10.	Spot analysis and colocalization analysis on cell boundaries and in TIRF	36
805	11.	Determination of bound fraction and diffusion constant.....	37
806	12.	Velocity and orientation distributions of persistently moving PBP2 and MreB.....	37
807	13.	Localization accuracy in low-frequency imaging	38
808	14.	Simulation of persistent and immobile tracks	38
809	15.	Determination of persistent and immobile states and switching rates	39
810	16.	Testing the two-state model of immobile and persistent states	39
811	17.	Calculation of the unbinding rate based on fluorescence-lifetime measurements	39
812	18.	Estimate of the number of MreB filaments per cell.....	40
813	19.	Measuring transitions from diffusive to bound states (Bound-Molecule FRAP)	40
814	20.	Estimation of the timescale of molecules leaving the TIR field of view due to persistent	
815	motion	41	
816	21.	Quantification of expression level from fluorescence	41
817	22.	Calculation of the stoichiometry between RodA and bound PBP2 molecules	41
818	23.	Model to test the contribution of diffusing PBP2 molecules to rod-complex activity	42
819	24.	Western blotting.....	43
820	25.	PBP2 Mass-spectrometry.....	43
821		<i>Preparation of E. coli whole protein extracts</i>	<i>44</i>
822		<i>LC-MS data acquisitions.....</i>	<i>44</i>
823		<i>Data analysis</i>	<i>45</i>
824		Bibliography	46

1. Key Resources Table

Reagent type (species) or resource	Designation	Source or reference	Identifiers	Additional information
strain, strain background (<i>E. coli</i>)	TKL130	(Lee et al., 2014)	MG1655 <i>mrdA::PAmCherry-mrdA</i>	
strain, strain background (<i>E. coli</i>)	EW07	This work	TKL130 Δ <i>mreCD</i> , pFB121	Materials and Methods, Section 2.
strain, strain background (<i>E. coli</i>)	EW49	This work	TKL130 Δ <i>rodZ</i> , pFB290	Materials and Methods, Section 2.
strain, strain background (<i>E. coli</i>)	AV48	This work	<i>186attB::Ptet-dcas9, mrdA::rPAmCherry-mrdA</i>	Materials and Methods, Section 2.
strain, strain background (<i>E. coli</i>)	NO53	(Ouzounov et al., 2016)	MG1655 <i>mreB-msfGFP^{SW}</i>	
strain, strain background (<i>E. coli</i>)	TU230(attL HC943)	(Rohs et al., 2018)	MG1655 <i>mrdA::aph (P_{lac}::msfgfp-mrdA)</i>	
strain, strain background (<i>E. coli</i>)	TU230(attL PR122)	(Rohs et al., 2018)	MG1655 <i>mrdA::aph (P_{lac}::msfgfp-pbpA(L61R))</i>	
strain, strain background (<i>E. coli</i>)	S352	This work	MG1655 Δ <i>ponA::aph</i>	Materials and Methods, Section 2.
strain, strain background (<i>E. coli</i>)	FB83	(Bendezú and Boer, 2008)	MG1655, <i>lacIZYA::frt, mreB-mCherry^{SW} yhdE::frt</i>	
strain, strain background (<i>E. coli</i>)	AV07	(Vigouroux et al., 2018)	MG1655 <i>mrdA::mcherry-mrdA</i>	
strain, strain background (<i>E. coli</i>)	AV127	This work	<i>186::dCas9, mrdA::sfgfp-mrdA</i>	Materials and Methods, Section 2.
strain, strain background (<i>E. coli</i>)	FB60 (iFB273)	(Bendezú and Boer, 2008)	MG1655 <i>lacIZYA::frt, rodZ::aph, Plac::gfp-rodZ</i>	

<i>coli</i>)				
strain, strain background (<i>E. coli</i>)	S504	This work	FB83, <i>rodZ::aph</i> , <i>P_{lac}::gfp-rodZ</i>	Materials and Methods, Section 2.
strain, strain background (<i>E. coli</i>)	S505	This work	AV07, <i>rodZ::aph</i> , <i>P_{lac}::gfp-rodZ</i>	Materials and Methods, Section 2.
chemical compound, drug	Mecillinam	Sigma-Aldrich, #33447		
chemical compound, drug	A22	Cayman Chemical #15870		
software, algorithm	Trackmate	(Tinevez et al., 2017) 10.1016/j.ymeth.2016.09.016		
software, algorithm	Morphometrics	(Ursell et al., 2017)		
software, algorithm	Spot-On	(Hansen et al., 2018)		

2. Strain construction

All strains, plasmids, and primers can be found in Supplementary File 3.

EW07: To obtain the MreCD depletion strain EW07 (TKL130 $\Delta mreCD$, pFB121) we introduced pFB121 (Bendezú and Boer, 2008) into TKL130. We replaced the *mreCD* gene by a kanamycin resistance gene (amplified from pKD13 with primer DmreC_fw and DmreC_rv) using the λ -Red mediated recombineering system expressed from pTKred (Kuhlman and Cox, 2010). The resulting strain was then grown at 42°C to cure the plasmid pTKred. We verified the deletion of *mreCD* by PCR.

EW49: For the RodZ depletion strain EW49 (TKL130 $\Delta rodZ$, pFB290) we first introduced pFB290 (Bendezú et al., 2009) into TKL130. In the resulting strain we deleted *rodZ* by a P1 transduction with lysate made from the $\Delta yfgA$ strain from the Keio collection yielding strain EW49.

AV48: We constructed a strain AV48 (186::P_{tet}-*dcas9*, *mrdA::rPAmcherry-mrdA*) that allows repressing the native *mrdAB* operon using CRISPRi and a guide RNA targeting the codon-modified ORF of rPAmcherry (Vigouroux et al., 2018), where 'r' denotes the codon modification (repressible). To construct strain AV48 we used allelic exchange on the strain LC69 (186attB::P_{tet}-*dcas9*) (Cui et al., 2018). To that end, we first electroporated the plasmid pAV25 (Vigouroux et al., 2018) into LC69 and selected for growth on chloramphenicol. Then we removed the plasmid backbone by transforming the cells with pAV10 (Vigouroux et al., 2018). The resulting strain was then grown at 42°C to cure the plasmid pAV10.

For RodA repression, we transformed AV48 with the CRISPR plasmid pcrRNA G20-R20 (Vigouroux et al., 2018) and pKC128 (P_{*mrdA*}-*PAmcherry-mrdA*, non-repressible version) to counter repression of native PBP2.

S352: For the *ponA* deletion strain we deleted *ponA* in TKL130 by a P1 transduction with lysate made from the Δ *ponA* strain from the Keio collection yielding strain S352.

AV127: The strain AV127 was obtained with the allelic exchange procedure described in (Vigouroux et al., 2018). LC69 (Cui et al., 2018) was electroporated with the suicide plasmid pAV101, then clones that integrated the plasmid by recombination were screened for by PCR. We then transformed these clones with pAV10 (Vigouroux et al., 2018) in a medium containing diacetyl-phloroglucinol (DAPG) to induce backbone excision. Finally, clones containing the desired scarless insertion were identified by PCR. To make pAV101, we amplified the *msfGFP-PBP2* fusion from pHC943 (Cho et al., 2016) with primers V396 and V397, the backbone from pSW23t with V171 and V394, and an homology region from MG1655's chromosome with V180 and V395. These three fragments were then assembled together by Gibson assembly. We checked the sequence of the fusion gene by Sanger sequencing.

S504: To construct a strain expressing both MreB-mCherry and GFP-RodZ fusions, we used FB83 (*mreB-mCherry*) and performed P1 transduction with lysate made from FB60(iFB273) (Δ *rodZ*, *Plac::gfp-rodZ*) (Bendezú et al., 2009) first selecting on ampicillin for *Plac::gfp-rodZ* then a second transduction with the same lysate and selecting on kanamycin for deleting the native *rodZ*.

S505: To construct a strain carrying both mCherry-PBP2 and GFP-RodZ fusions, we used strain AV07 (*mCherry-mrdA*) and performed P1 transduction with lysate made from FB60 (iFB273) (Δ *rodZ*, *Plac::gfp-rodZ*) (Bendezú et al., 2009) first selecting on ampicillin for *Plac::gfp-rodZ* then a second transduction with the same phage lysate and selecting on kanamycin for deleting native *rodZ*.

3. Bocillin labelling

PBP2 levels of strains MG1655, TKL130 and TKL130/pKC128 were measured by a Bocillin-binding assay as described similarly in (Cho et al., 2016; Kocaoglu et al., 2012). We performed the quantification in parallel on two identical cultures grown from independent colonies of each strain. We grew strains overnight in LB at 37° C. We then washed the cells in LB, diluted them 1/200 in LB and grew them at 37° C until an OD600 of ~0.4. We washed 1.8 ml of the culture in PBS, resuspended in 200 μ l PBS and kept cultures on ice. We disrupted cells by sonication (FB120, Fisher Scientific) and centrifuged them for 15 min at 4° C (21,000 g). We subsequently resuspended the pellet corresponding to the membrane fraction in 50 μ l PBS containing 15 μ M fluorescently labelled Bocillin-FL (Invitrogen). Membranes were incubated at 37° C for 30 min and washed once in 1ml PBS. We centrifuged the membranes for 15 min (21,000 g) and resuspended them in 50 μ l PBS. We measured the protein concentration of each sample with a colorimetric assay based on the Bradford method (#5000006, Bio-Rad) and loaded equal amounts of protein mixed with 4X Laemmli buffer onto a 10 % polyacrylamide gel. We visualized the labelled proteins with a Typhoon 9000 fluorescence imager (GE Healthcare): excitation at 488 nm and emission at 530 nm. We quantified the relative amounts of PBP2 in each sample by quantifying the grey values of each lane in ImageJ (Schneider et al., 2012).

4. Sample preparation and imaging conditions

Cells were grown overnight at 37°C in LB medium and then washed and diluted at least 1:500 in M63 minimal medium (Miller, 1972) supplemented with 0.1% casamino acids, thiamine (5·10⁻⁵%), glucose (0.2%) and MgSO₄ (1 mM) (here referred to as minimal medium) and grown to early exponential phase (maximum OD600 of 0.1) at 30°C. If strains carried antibiotic resistance we added the respective antibiotics to the medium (carbenicillin (100 μ g/ml), kanamycin (50 μ g/ml), chloramphenicol (30 μ g/ml), all Sigma-Aldrich). Inducers were added as indicated below. For microscopy, cells were spotted on 1% agarose pads (UltraPure™ Agarose, Invitrogen) of minimal medium, without any antibiotics. Drugs targeting MreB or cell-wall synthesis and inducers were added as indicated below.

For technical replicates, we grew cell cultures to exponential phase in independent flasks starting from the same saturated overnight culture. For biological replicates, we grew overnight cultures from different bacterial colonies.

Cells were imaged in a custom-built temperature-controlled chamber at 29°C. Prior to imaging the cells were incubated 10-20 min on the microscope to equilibrate sample temperature and minimize drift. In experiments with drugs [mecillinam (Sigma-Aldrich, #33447), A22 (Cayman Chemical #15870)] cells were spotted on agarose pads containing the antibiotic at the concentration of 100 µg/ml (mecillinam), or 20-50 µg/ml (A22). For treatments longer than 20 min cells were incubated in liquid culture with the respective antibiotic at the same concentration prior to imaging. The indicated incubation times denote the total incubation time in liquid and on the pad.

In experiments where we depleted MreCD and RodZ (strains EW07 and EW49 respectively) we grew cells in the presence of 50 or 100 µM IPTG respectively (EUROMEDEX #EU0008-B) and carbenicillin both during overnight growth and during regrowth as described above. We then washed the cells 3 times, diluted them and grew them in minimal medium in the absence of IPTG for 6 hours.

In experiments where we repressed the *mrdAB* operon (strain AV48/pcrRNA G20-R20/pKC128) we grew cells in the presence of kanamycin and chloramphenicol both during overnight growth and during regrowth as described above. We added anhydrotetracycline (aTc) (100 ng/ml, Acros Organic) upon dilution in minimal medium to induce the repression. We grew cells for 9 h prior to imaging both in the presence and absence of aTc.

In experiments where we imaged msfGFP-PBP2, TU230(attLHC943) cells are plated on and grown overnight in minimal media containing 25 µM IPTG. For the regrowth from saturated culture, we used minimal media containing the indicated IPTG concentration. We grew cells for 6, 8 or 10 hours to early exponential phase at 30°C. For the measurement of auto fluorescence, we grew MG1655 in the same way but without the addition of an antibiotic or IPTG.

In experiments where we imaged GFP-RodZ, we used 100 µM IPTG.

For MreB-curvature correlation measurements we grew NO53 or NO53/pDB192 overnight at 37°C in LB medium. We diluted the cultures by 1:500 and grew them at 30°C in LB medium for 2h. We then washed the cultures and diluted them 1:200 in MOPS rich medium (MOPS EZ Rich Defined Medium Kit. Cat.No. M2105, TEKnova) and grew them at 30°C for an additional 4h, such that the culture density remained below an OD600 of 0.1. The growth media of NO53/pDB192 cells contains carbenicillin at all times until the cells are harvested for microscopy. Cell division is inhibited by adding 1mM IPTG in liquid culture inducing *sula* expression 30 min prior to imaging. Cells were placed on 1% agarose pads of the same media without any antibiotics but containing the same amount of IPTG for filamentation. Images were taken right after placing cells on a pad (NO53) or after maintaining cells for 30 min on the pad at the same 30°C (NO53/pDB192).

5. Microscopy

Single particle tracking of PAmCherry-PBP2 and msfGFP-PBP2 was performed on a custom-designed fluorescence microscope (here referred to as microscope 1) in TIRF (total internal reflection fluorescence) mode. The microscope was equipped with a 100x TIRF objective (Apo TIRF, 100x, NA 1.49, Nikon), three laser lines: 405 nm (Obis, Coherent), 488 nm (Sapphire, Coherent), 561 nm (Sapphire, Coherent), a dichroic beamsplitter (Di03-R488/561-t3-25x36, Semrock), an edge filter for PAmCherry imaging (BLP02-561R-25, Semrock), and a laser-line filter (NF561-18, Thorlabs). Shuttering of the 488 nm laser was controlled with an acusto optic tunable filter (AA Optoelectronics) or with shutters (Uniblitz, LS3 and TS6B, Vincent Associates). The 405 nm laser was controlled directly via a USB interface. Images were acquired with an EMCCD camera (iXon Ultra, Andor). All components were controlled and synchronized using µManager (Edelstein et al., 2010).

For high-frequency imaging with PAmCherry-PBP2, images were acquired with exposure time and intervals of 60 ms for a duration of 1 min. A weak UV-laser pulse (405 nm, 100-200 ms) was provided before the acquisition and every 200 frames during the measurements to

activate new fluorophores. To obtain low variability of the bound fraction of molecules between replicates (standard deviation < 5%) we aimed to generate about 1000 tracks per technical replicate by taking 3-10 movies per replicate.

Low-frequency imaging was conducted with an exposure time of 1000 ms and with imaging intervals of 3.6 s or 1 s for a duration of 3.5 min or 3 min, respectively. We activated fluorophores once before the acquisition for 100-200 ms. In this way we collected 7-9 movies per replicate yielding about 100 tracks of at least 4 time steps, which resulted in variability of the persistent fraction of standard deviation < 10%. This way, the imaging time did not exceed 30 min per replicate.

Single molecule tracking with cells carrying the msfGFP-PBP2 fusion requires a photo-bleaching phase prior to image acquisition. For high-frequency imaging, the sample was exposed to 488 nm laser in epi mode in order not to bias our analysis towards diffusive molecules as exposure to light in TIR mode would predominantly lead to a loss of bound molecules. After photo-bleaching, we immediately switched to TIR mode for image acquisition. Images are taken with 60 ms exposure time and intervals for a duration of 1 minute as for the PAmCherry fusion. As for PAmCherry-PBP2, we aimed to generate about 1000 tracks per replicate.

For low-frequency imaging of msfGFP-PBP2, the sample is first photo-bleached in TIR mode with high laser power. This step is followed by image acquisition while using a reduced laser power with an exposure time of 1000 ms and imaging intervals of 3.6 s for a duration of 4.5 minutes. Bleaching times for both cases were adjusted according to the PBP2 levels and it varies between 5 to 30 or 2 to 10 seconds for high and low frequency imaging respectively. As for PAmCherry-PBP2, we aimed to generate > 100 tracks per replicate.

For measurements of cell shape, average fluorescence intensity, MreB-curvature correlations, and MreB rotation we used two inverted epi-fluorescence microscopes, an Eclipse Ti (Nikon) microscope (microscope 2) or a DeltaVision™ Elite (GE Healthcare) microscope (microscope 3). Microscope 2 is equipped with a 100x phase contrast objective (CFI PlanApo LambdaDM100X 1.4NA, Nikon), a solid-state light source (Spectra X, Lumencor Inc., Beaverton, OR), a multiband dichroic (69002bs, Chroma Technology Corp., Bellows Falls, VT), and excitation (485/25) and emission (535/50) filters. Images were acquired using a sCMOS camera (Orca Flash 4.0, Hamamatsu, Japan) with an effective pixel size of 65 nm. Microscope 3 is equipped with a 100x phase contrast objective (UPlanSApo 100X NA 1.4, Olympus), a multi-band dichroic beamsplitter (DAPI-FITC-mCh-Cy5) with excitation (475/28) and emission (525/48) filters, and a sCMOS camera (DV Elite, PCO-Edge 5.5) with an effective pixel size of 65nm.

For measurements of fluorescence on cell boundaries, contour curvature, and MreB-msfGFP tracks, we focused on cells based on the phase-contrast signal. to track MreB-msfGFP spots moving at the bottom of the cell, we moved the focal plane 250 nm below the central plane of cells. Images were taken every 1 s for a duration of 120 s. We generated images of about 100 cells per replicate.

6. Cell segmentation

Cell boundaries were detected from phase contrast microscopy images on microscope 2 or 3 using the MATLAB based cell segmentation tool Morphometrics (SimTK) (Ursell et al., 2017). The cell poles and the cell centerline were identified using the MicrobeTracker package (Sliusarenko et al., 2011). The spacing of subsequent points along the cell centerline was chosen as 0.5 pixels (32 nm). Cell width was measured as the median of all local widths.

A smoothened centerline (x- and y-coordinates Gauss-filtered, $\sigma = 3.5$ steps) was used for a cell-internal orthogonal coordinate system, specifically to determine the local orientation of the cell.

7. PBP2 tracking

All images taken on microscope 1 were analyzed using custom Matlab code (available as source code file). First, we segmented bright field images using a semi-automated approach based on standard image processing tools to separate regions containing cells from background regions. For spatially separated cells this also allowed us to obtain a coordinate system for each cell.

PAmCherry-PBP2 spots in fluorescence images were identified as the local maxima of the denoised (bandpass filtered) images with intensity 3.5 or 2 (for fast and slow imaging, respectively) times higher than background (bpass and pkfnd functions from <https://site.physics.georgetown.edu/matlab/code.html>). Sub-pixel resolution was achieved by finding the center of a two-dimensional Gaussian fitted to the intensity profile of each spot. We discarded peaks with a poor (residuals of fit) or broad (standard deviation of fit) Gaussian profile. Spots in subsequent frames were then connected into raw trajectories if their distance was below a threshold distance that is consistent with diffusion (high-frequency imaging) or persistent motion (low-frequency imaging) (Crocker and Grier, 1996). Threshold distances were 600 nm for imaging intervals of $\tau = 60$ ms, 112.5 nm for $\tau = 1$ s, and 225 nm for $\tau = 3.6$ s. If tracking of a particle lead to a situation where a particle can be connected to more than one possible peak in the next frame we discontinued the tracking for this trajectory. We checked that low-frequency trajectories lie in cells by comparing fluorescent images and brightfield images.

msfGFP-PBP2 images from fast frequency imaging are analyzed in the same way except that peaks which have intensity 1.6 times higher than background are selected.

msfGFP-PBP2 spots from low frequency imaging were identified and tracked in the following way: Peaks were preselected as local maxima in the bandpass-filtered image (using a Laplacian of Gaussian filter with $\sigma = 1.8$ pixels and pkfind, as above). We only considered local maxima in regions of the 2% highest intensity values that are 4-connected and contain at least 3 pixels each. We only consider peaks with nearest-neighbor distance higher than 3.5 pixels.

For further peak selection and sub-pixel localization we considered denoised raw images (using a Gauss filter with $\sigma = 0.4$ pixels). We selected peaks with a ratio of peak signal to local background noise higher than 3. Local background intensity and noise are respectively the average and standard deviation of the values of the pixels at a distance included between 3 and 4 pixels of the center of the peak. To avoid very low intensity peaks we also discarded peaks with absolute signal (<2000 counts for 1s exposure, <1200 counts for 60ms exposure), and we remove the 1% of the peaks with highest intensities, as those likely represent clusters of molecules. Sub-pixel resolution was achieved by fitting a two-dimensional Gaussian to every selected peak. Peaks with standard deviation > 3 or with a ratio of the average absolute value of the residuals divided by peak intensity > 0.2 are removed.

Tracking was performed using the same code from (Crocker and Grier, 1996) with a maximum displacement between subsequent frames of 4 pixels (both for slow and fast tracking). For lifetime measurements with a time interval of 12 s, we increased to maximal displacement to 6 pixels.

For the comparison between different datasets we used Student's t-test for bound fractions, persistent fractions, and diffusion constants where appropriate. P-values are indicated in supplemental datasets corresponding to the different figures.

8. MreB tracking

Fluorescence images were analyzed using a custom Matlab code: Images were first filtered in both space and time using a three-dimensional Savitzky-Golay filter with a filter size of 3 pixels in xy-directions time 3 points along the temporal dimension. Images were subsequently de-noised once more using a 2D-Gauss filter ($\sigma = 0.5$ pixels).

Images were subsequently rescaled by a factor of 5 using spline interpolation to achieve sub-pixel resolution. MreB spots were detected as local maxima inside the cell boundary obtained by segmentation.

The local maxima were connected to construct raw trajectories based on their distance at consecutive time points (van Teeffelen et al., 2011) with a maximal displacement during subsequent time frames of 2 pixels.

9. Curvature analysis and MreB-curvature correlations

After obtaining the cell contours and the two poles of each cell we first computed the contour curvature all along the cell boundary by fitting a polygon to every contour point and its two neighboring points (MATLAB function LineCurvature2D, <http://www.mathworks.com/matlabcentral/>). Negative curvature values correspond to indentations and positive curvature values to bulges and poles. To eliminate the influence of noise the contour curvature c is then obtained by Gauss-filtering the raw curvature values ($\sigma = 2$ steps, corresponding to 65 nm).

To obtain MreB-msfGFP intensities along the cell boundary we first smoothened raw MreB-msfGFP images using a 2D-Gauss filter ($\sigma = 0.5$ pixels). For interpolation of the GFP images at points close to the cell boundary we then corrected the contour coordinates \mathbf{r}_i for systematic shifts between the phase-contrast-based cell contours and the GFP-intensity peaks corresponding to MreB filaments. Specifically, we obtained the corrected contour coordinates \mathbf{r}_i^c from the Morphometrics-based contour coordinates \mathbf{r}_i according to

$$\mathbf{r}_i^c = \mathbf{r}_i + \Delta\mathbf{r} - \mathbf{r}_{\perp i} s.$$

Here, the first term $\Delta\mathbf{r} = (-0.35, -0.78)$ pixels is a microscope-dependent displacement vector that accounts for a systematic shift between phase-contrast and GFP images. The second term shifts the contour by an amount $s = 140$ nm inward (along a vector normal to the cell boundary $\mathbf{r}_{\perp i}$), such that the corrected contour passes through the positions of the GFP intensity peaks that correspond to the positions of MreB filaments on the sides of the cell. By convention, $\mathbf{r}_{\perp i}$ always points outward from the cell center. To make sure to take MreB-msfGFP peaks into account even if they are slightly displaced from the corrected boundary, GFP intensity values I_i are then obtained by linear interpolation of the smoothened MreB-msfGFP image at the positions of the corrected contour and at two other points perpendicular to the boundary and spaced 0.5 pixel inward and outward:

$$I_i = \frac{1}{3} [I(\mathbf{r}_i^c - \mathbf{r}_{\perp i} \delta) + I(\mathbf{r}_i^c) + I(\mathbf{r}_i^c + \mathbf{r}_{\perp i} \delta)],$$

where $\delta = 65$ nm. Subsequently, intensity values are normalized by the average taken over the full contour, the side walls, or the straight cell segments, respectively, depending on the analysis. To obtain the MreB enrichment as a function of curvature, the curvature values are binned and MreB intensities corresponding to those curvature values are averaged. Subsequently, intensity values are normalized by the average intensity found close to zero curvature:

$$I_i^c = I_i / \langle I_i | -0.05/\mu\text{m} < c_i < 0.05/\mu\text{m} \rangle.$$

If a bin contains less than at least 0.1% of the data points per replicate, it is not displayed in the figure.

To remove the cell poles and potential septa from the analysis, we removed 2 μm from each cell pole (according to the distance along the centerline) and 650 nm from the middle of the cell. The large distance from the poles was chosen, since the automated software does sometimes not identify the poles correctly. In those cases, contour points can fall into MreB-msfGFP-free regions at the poles even if the corresponding centerline points are more than just 0.5 μm away from the automatically identified poles.

To determine correlations between MreB and contour curvature independently of spontaneous cell bending, we either concentrated on regions where the smoothened centerline was straight or we performed two independent normalization approaches:

1105 To constrain our analysis to straight segments of the cell we considered only those boundary
1106 points corresponding to centerline curvatures with $|\kappa_i| < 0.05/\mu m$.

1107 In the first normalization approach we renormalized the contour curvature by subtracting the
1108 contribution of cell bending according to

1109
$$c_i^{\text{corr}} = c_i \pm \kappa_i / \left(1 - \frac{\kappa_i w_i}{2}\right),$$

1110 where κ_i is the curvature of the smoothened centerline (x- and y-coordinates Gauss-filtered,
1111 $\sigma = 3.5$ steps), and where w_i is the local width of the cell. The centerline was smoothened to
1112 consider only the contribution of long-range bending rather than the impact of short-scale
1113 oscillations of boundary curvature. Positive/negative centerline-curvature values correspond
1114 to cells bent to the right/left along the direction of the centerline. The plus or minus signs
1115 correspond to the right or left side of the cell, respectively. The correction only works for
1116 segments of the cell with $\kappa_i < 0.5 w_i$ to avoid divergence. For the cell segments excluding
1117 poles and potential septa this criterion was always fulfilled.

1118 In the second normalization approach we renormalized the MreB intensity by the component
1119 expected due to cell bending:

1120
$$I_i^{\text{corr}} = I_i / (1 \pm \alpha \kappa_i w_i),$$

1121 where $\alpha \sim 0.2$ is a coefficient that accounts for the correlations observed between MreB
1122 intensity and smoothened centerline curvature (Fig. 6–SI Fig. 2D). As above, the plus/minus
1123 signs correspond to the inner/outer face of the bent cell, respectively.

1124 **10. Spot analysis and colocalization analysis on cell boundaries** 1125 **and in TIRF**

1126 To analyse the distribution of fluorescence peaks of cells expressing mCherry-PBP2, MreB-
1127 msfGFP, or GFP-RodZ and to perform colocalization measurements we first obtained
1128 fluorescence profiles on cell contours from epi-fluorescence images as described in Section
1129 9.

1130 Peak analysis: Fluorescence profiles were smoothened with a Gauss filter ($\sigma = 0.5$ pixels).
1131 Subsequently, we subtracted the median intensity of every cell contour. Peaks were then
1132 detected as positive-valued local maxima (Figs. 3C).

1133 The intensity-dependent peak density is the number of peaks with intensity p divided by total
1134 contour length of all cells $\sum_i^{N_{\text{cells}}} l_i$. For the total density of all peaks, we considered all peaks
1135 with peak height 3 times higher than the estimated intensity noise (gray regions in Figs. 3C).
1136 The noise was calculated in non-treated conditions. To that end, we filtered the raw
1137 fluorescence image with a 2D Gauss filter of $\sigma = 0.5$ pixels and $\sigma = 3$ pixels separately. The
1138 signal on the cell boundaries are then extracted from two sets of images. Next, we took the
1139 difference of signals belonging to same cells and calculated the average standard deviation
1140 of the differences, which is used as a readout for pixel noise.

1141 For colocalization analysis, we extracted profiles as described above for two different fusions
1142 and calculate the Pearson correlation coefficient in each cell independently.

1143 For the analysis of spots and colocalization with TIRF microscopy, images of mCherry-
1144 PBP2, MreB-msfGFP, MreB-mCherry, and GFP-RodZ are taken with Microscope 1 in TIRF
1145 mode. Cells are manually segmented based on the bright-field image by drawing a line
1146 along the long axis of the cell, defining a centerline. The raw fluorescence images are
1147 smoothened using a 2D-Gauss filter ($\sigma = 1$ pixel). The 2D-intensity map is acquired from the
1148 region ± 210 nm around the centerline. For peak analysis, we subtracted the median
1149 intensity from every map and detected peaks as positive-valued local maxima. The intensity-
1150 dependent peak density and total density of all peaks are calculated in the same way as on
1151 the cell boundary. To calculate the levels of noise, the raw fluorescence images are filtered
1152 with a 2D Gauss filter of $\sigma = 1$ pixel and $\sigma = 3$ pixels separately. Next, we took the difference
1153 of maps belonging to same cells and calculated the average standard deviation of the
1154 differences, which is used as a readout for pixel noise.

For colocalization analysis with TIRF microscopy, we first applied a correction for the systematic shifts between the signals appear in the red- and green- channels. By imaging TetraSpeck beads (Invitrogen) in the two channels and performing peak detection, we found a displacement vector $\Delta \mathbf{p} = (-1, -0)$ with a magnitude of 105 nm. Then, we modified the coordinates of the points on the centerline of each cell according to: $\mathbf{p}_i^c = \mathbf{p}_i + \Delta \mathbf{p}$ where \mathbf{p}_i and \mathbf{p}_i^c show the original and modified centerline coordinates, respectively. Next, we generated 2D intensity maps (Fig. 5–SI Fig. 3C-D) and calculated the Pearson correlation coefficient between the two different fluorescence channels for each cell.

11. Determination of bound fraction and diffusion constant

We used the Spot-On software (Hansen et al., 2018) to fit 2- and 3-state-diffusion models to high-frequency data (Supplementary File 2). In brief, Spot-On fits the experimental jump-length distributions for different time lags to the analytical solution of a multi-state diffusion model. The code returns fractions and diffusion constants of the different fractions, and the particle-localization precision. We used jump-length distributions from lags between 1 and 5 time intervals (60-300 ms). To that end, we selected tracks with at least 4 or 7 localizations, for PAmCherry and GFP fusions respectively. We used a normalized value for the sum of residuals (χ^2) acquired by dividing χ^2 by the number of bins and by the lag time (in number of time steps) used.

To make sure bound molecules are indeed bound, we checked the value of D_{bound} by leaving it free for TKL130 and TKL130/pKC128 tracks (Supplementary File 2b). D_{bound} is then found to be between 10^{-4} - 10^{-9} from fitting a 3-state model. After confirming near-zero values for D_{bound} , we fixed $D_{\text{bound}} = 0$ for all experiments.

We complemented Spot-On measurements by a different method, which is based on the distribution of single-track effective diffusion constants (referred to as ‘ D_{eff} -based method’): For every track, we calculated D_{eff} from the first 4 steps of each track, applying a linear fit of single-track MSD's $\langle x^2(t) \rangle$ according to $\langle x^2(t) \rangle = 4D_{\text{eff}}t + 4\sigma^2$. The empirical distribution of D_{eff} was then compared with distributions generated from computational simulations. For the reference condition of PAmCherry-PBP2 fusions (TKL130), we calculated distributions $p(D_{\text{eff}}|D, \sigma)$ for diffusive molecules with different diffusion constant D and localization uncertainties σ . The combined distribution of a two-state population is then given by $p(D_{\text{eff}}) = b p(D_{\text{eff}}|D_{\text{bound}} = 0, \sigma) + (1-b) p(D_{\text{eff}}|D, \sigma)$, where we assume bound molecules to be immobile. For every combination $[D, \sigma]$ we obtained the bound fraction b by fitting the peak value at $D_{\text{eff}} = 0 \mu\text{m}^2/\text{s}$ to the experimental data. $[D, \sigma]$ were then obtained by minimizing the residual sum of squares (RSS) between experimental and simulated distributions, considering values for D_{eff} between -0.015 and 0.055 $\mu\text{m}^2/\text{s}$ (see Fig. 1–SI Fig. 3A). We used a bin size of 0.005 $\mu\text{m}^2/\text{s}$. We varied D between 0.015 and 0.06 $\mu\text{m}^2/\text{s}$ with an interval of 0.005 $\mu\text{m}^2/\text{s}$ and σ between 0 and 40 nm with an interval of 5 nm. The parameter set of $D = 0.04 \mu\text{m}^2/\text{s}$ and $\sigma = 20$ nm gave the lowest RSS. We confirmed that $D_{\text{bound}} = 0 \mu\text{m}^2/\text{s}$ by comparisons between distributions for zero and finite values of D_{bound} (Fig. 1 SI Fig. 3B).

We compared the values given by Spot-On with the D_{eff} -based method using a 2-state model and acquired very similar results (Fig. 1 SI Fig. 3C).

12. Velocity and orientation distributions of persistently moving PBP2 and MreB

Directed motion of individual trajectories can be inferred from a quadratic dependency of the single-particle mean squared displacement (MSD) on time according to

$$\langle x_i^2 \rangle = v_i^2 t^2 + b_i. \quad (11.1)$$

Here, v_i denotes the velocity of particle i and b_i is an offset reflecting the localization error.

To determine the velocity distribution of persistently moving PBP2 molecules or MreB filaments, respectively, we analyzed a subset of trajectories obtained with 1 s time intervals, for which each single-track MSD could be well fit by a quadratic function of the form of Eq. (11.1) according to the coefficient of determination R^2 . We considered trajectories with at least 4 time steps. For PBP2 we considered trajectories with a maximum of ten time steps to

prevent a bias towards slowly moving molecules that are more likely to remain in the TIR field of illumination for long times. MreB trajectories are longer in time than PBP2 trajectories, since they are obtained from filaments containing many msfGFP molecules, and they are obtained from a larger field of view since their movement is measured in epi-fluorescence mode. For comparability with PBP2 tracks we therefore constrained the MreB trajectories by analyzing the 10 displacement steps around the point closest to the cell centerline. These displacements are found within a field of view also detectable in TIRF mode.

The velocity distributions for different minimal R^2 values are plotted in Fig. 1–SI Fig. 5D. As expected, low velocities corresponding to immobile molecules contribute less with increasing minimal R^2 . Accordingly, both MreB and PBP2 showed a mildly increasing average velocity as a function of the minimum R^2 (Fig. 1 SI Fig. 5D). For comparison between PBP2 and MreB in Fig. 1F-G we generated velocity distributions from tracks that showed R^2 values ≥ 0.9 , corresponding to $\sim 10\%$ of PBP2 tracks that showed the highest R^2 values (Fig. 1 SI Fig. 5C), yielding average velocities of 18.3 nm/s for PAmCherry-PBP2 and 16.5 nm/s for MreB-msfGFP filaments (Fig. 1 SI Fig. 5D).

Performing the same analysis on PAmCherry-PBP2 trajectories generated with a time interval of 3.6 s we obtained an average velocity of $v = 14.2$ nm/s for persistent tracks ($R^2 \geq 0.9$). The average velocity is lower than for the 1 s dataset because fast-moving molecules are observed less often than slowly moving molecules, as they leave the TIR field of view at higher probability (Fig. 1 SI Fig. 5E-F). For msfGFP-PBP2 we obtained an average velocity of 13.5 nm/s.

To obtain the orientation of persistent PBP2 tracks we calculated the angle between the end-to-end vector of persistent trajectories measured with time interval of 3.6 s (same criteria of $R^2 \geq 0.9$ and a minimum length of 4 time points) and the cell orientation. For MreB we calculated the orientation in the same way and on the same data for which we obtained the velocity distribution.

13. Localization accuracy in low-frequency imaging

We determined the experimental localization accuracy from the distribution of displacements from measurements at 3.6 s time intervals for PAmCherry-PBP2 (Fig. 1 SI Fig. 6A). We restricted our analysis to immobile molecules according to a simple criterion (end-to-end distance less than 200 nm for tracks of at least 7 steps). The standard deviation σ_d of a Gaussian fit to the distribution of displacements in a single spatial direction is determined by $\sigma_d^2 = \langle (x_i - x_{i+1})^2 \rangle = 2\sigma^2$, where σ is the localization uncertainty. Therefore, $\sigma = \sigma_d/\sqrt{2}$. For PAmCherry-PBP2 $\sigma = 25$ nm.

14. Simulation of persistent and immobile tracks

To establish a criterion for reliably classifying persistently moving and immobile states in experimental PBP2 trajectories, we computationally simulated tracks of immobile or persistently moving molecules resembling the tracks observed by microscopy using 3.6 s time intervals. To that end we randomly picked a trajectory length (number of steps n) from an exponential distribution with $\langle n \rangle = 3.5$ that resembled the experimental length distribution (Fig. 1 SI Fig. 6B). For the simulation of persistently moving or immobile molecules we imposed a constant step size in the x-direction corresponding to the experimental velocity ($v = 14$ nm/s for PAmCherry-PBP2) for persistent molecules or to $v = 0$ nm for immobile molecules. To account for the localization uncertainty we subsequently added to all x- and y-coordinates a random displacement drawn from a normal distribution with a mean of 0 nm and a standard deviation equal to the localization accuracy for low-frequency imaging 25 nm (for PAmCherry-PBP2).

Trajectories with transitions between immobile and persistent states were obtained by randomly selecting sub-trajectories from a single 1000-step long trajectory containing transitions between persistent and immobile states. Transition rates were obtained from experimental data (see next paragraph).

15. Determination of persistent and immobile states and switching rates

For each time point we calculated the smoothed local velocity by dividing the displacement during the surrounding w time steps by the time lag $w\tau$:

$$v(t) = \mathbf{r}\left(t + \frac{w}{2}\right) - \mathbf{r}\left(t - \frac{w}{2}\right) / w\tau,$$

Here $\mathbf{r}(t) = (x(t), y(t))$ is the position at time t , and $\tau = 3.6$ s is the imaging time interval. We classified the particle as either immobile or persistently moving at time t if v was smaller or bigger than the threshold velocity v_{thr} , respectively.

We applied different values for w and v_{thr} to simulated trajectories of PAmCherry-PBP2 ($v = 14$ nm/s; $\sigma = 25$ nm) to find the parameter combination that reliably detected dynamic states in simulated tracks with more than 99% success rate (Fig. 1 SI Fig. 6C). We chose a window size of $w = 4$ and a velocity threshold of $v_{\text{thr}} = 8$ nm/s (classifying 99.6% of segments of simulated immobile molecules as immobile and 99.6% of simulated persistent molecules as persistent) (Fig. 1 SI Fig. 6C). Since we found almost identical average velocity for msfGFP-PBP2, we used the same window size and velocity threshold for persistence classification.

We calculated transition rates k_{ip} or k_{pi} by counting the number of transitions from immobile to persistent or persistent to immobile states, respectively, and dividing by the total duration of persistent or immobile states observed. Here, we ignored intermittent segments of duration of a single time step.

All error bars denote standard errors between replicates.

16. Testing the two-state model of immobile and persistent states

To test whether the dynamics of PBP2 molecules is compatible with a model of molecules residing in either of two possible states we measured single-particle MSD's of track segments identified as either immobile or persistent (Fig. 1–SI Fig. 6A). The average MSD of segments classified as persistently moving increased quadratically with time, while the average MSD of segments classified as immobile remained nearly constant (Fig. 1 SI Fig. 6 D-E).

To test whether deviations of single-particle MSDs from the average were due to transitions between the two states we analyzed computationally simulated tracks of our two-state model containing transitions. We then used the same classification criterion and MSD analysis on simulated tracks as on experimental tracks. For simulations of persistent segments we adjusted the velocity of $v = 12$ nm/s (compared to 14 nm/s above) that yielded better agreement of the average MSD curves of persistent segments with experiments (Fig. 1–SI Fig. 6D). The difference is likely due to the fact that we consider here all persistent segments while above we obtained the velocity from the 10% most persistent full tracks according to the R^2 -criterion.

Simulations and experiments showed very similar distributions of single-particle MSD's (Fig. 1–SI Fig. 6F), suggesting that bound PBP2 molecules are indeed either immobile or persistently moving, but not found in a qualitatively different slowly-moving state.

17. Calculation of the unbinding rate based on fluorescence-lifetime measurements

To obtain the unbinding rate k_{bd} in non-treated or A22-treated cells we measured lifetime distributions of tracks $f(n, \tau)$ obtained with 1 s exposure time and different time intervals $\tau = 1$ s or 12 s (Fig. 2). Here, n is the number of steps a track is observed corresponding to the lifetime $t = n\tau$. At first, we assume two random processes to contribute to particle loss: GFP bleaching with a probability p_b per time frame, and a second process with an apparent track termination rate k_a , corresponding to a termination probability $p_a = 1 - \exp[-k_a \tau]$.

For A22-treated cells, k_a is caused by unbinding only, that is, $k_{bd} = k_a$. For non-A22-treated cells, k_a subsumes unbinding and particles leaving the field of view due to persistent motion. While the probability of molecules leaving the field of view is not independent of track duration, this assumption does not affect our calculation of k_{bd} , as we will see below.

For both conditions (-A22, +A22), we simultaneously fit the two lifetime distributions to the above model, considering tracks between 3 to 7 steps (4-8 localizations). For A22-treated cells we obtained $p_b = 0.43 \pm 0.08$ and $k_a = k_{bd} = 0.021 \pm 0.008 \text{ s}^{-1}$. The unbinding rate corresponds to an average lifetime of the bound state of $48 \pm 18 \text{ s}$.

For non-A22-treated cells we obtained $p_b = 0.39 \pm 0.08$ and $k_a = 0.035 \pm 0.007 \text{ s}^{-1}$. To estimate the contribution of persistent motion to the apparent unbinding rate, we then conducted simulations of bound molecules transitioning between persistent and immobile states: Molecules started from random positions within the field of view (width 600 nm) either moving persistently with speed of $v = \pm 14 \text{ nm/s}$ perpendicular to the central axis, or resting immobile. Transitions between the two states occurred at experimental rates k_{ip} and k_{pi} , respectively. The probability of bleaching was set equal to p_b . In a second set of simulations, we changed either of the two rates to maintain the measured persistent fraction of $p = 80\%$, that is, either $k_{ip}^{\text{corr}} = k_{pi} p / (1 - p)$ or $k_{pi}^{\text{corr}} = k_{ip} (1 - p) / p$ (Fig. 2–SI Fig. 1). We then measured track-length distributions from simulations with different unbinding rates k_{bd} to infer the range of unbinding rates k_{bd} compatible with the experimentally obtained apparent termination rate k_a (Fig. 2–SI Fig. 1).

In both conditions, experimental lifetime distributions of 1 s data are dominated by bleaching. Therefore, the time-dependent process of persistent molecules leaving the field of view only affects the 12 s distributions. While those distributions are not perfectly exponential, we could still fit them by an exponential function over the window of 3 to 7 steps, considered here.

18. Estimate of the number of MreB filaments per cell

To estimate the number of MreB filaments we assume for simplicity that all MreB proteins of the cell are part of dimers of MreB protofilaments (Salje et al., 2011). A substantial fraction of proteins is found as cytoplasmic monomers. Our estimate is therefore rather conservative. Previous measurements suggest that there is a broad distribution of filament lengths with many filaments as long as 1 μm (Ouzounov et al., 2016). As a conservative estimate we assume that all filaments are 100 nm in length and have a repeat length of 5 nm (Salje et al., 2011). Each of the idealized filaments therefore contains 40 monomers. With an average of 2000 or 11000 proteins per cell in poor or rich growth media, respectively (Li et al., 2014) the cytoplasmic membrane is decorated with up to 50-200 filaments according to this simple model.

19. Measuring transitions from diffusive to bound states (Bound-Molecule FRAP)

In order to determine the transition rate from the diffusive to the bound state k_{db} we measured the bound fraction at different time points after bleaching the field of view, conceptually similarly to classical FRAP (fluorescence recovery after photobleaching) experiments. In a first step we aimed to activate all PAmCherry fluorophores in the TIRF field of view with a 1.5 s exposure of 10-fold increased UV intensity compared to our standard protocol (see above). We introduced a waiting time of 2 seconds in the dark in order to let diffusive photo activated PBP2 molecules escape the field of view. Then, we photo bleached for 4 seconds with normal excitation intensity. After a recovery period of 0-10 minutes in the dark, we acquired images in high-frequency mode without any additional photo activation for a duration of 48 seconds. In this way, we were able to detect PAmCherry-PBP2 molecules, which were activated in the first step, which were able to escape the field of view during the 2 second pause, and which then reentered the field of view, where they either remained diffusive or bound to their substrate.

For finding bound fractions as reported in Fig.4B, we fixed $D_1 = 0.02$ and $D_2 = 0.06$ which are the diffusion constants found in the reference state (A22-treated cells with 20ug/ml for 30 minutes) in order to avoid fluctuations in population sizes.

20. Estimation of the timescale of molecules leaving the TIR field of view due to persistent motion

To estimate the average time it takes a molecule that bound randomly in the field of view to leave the field of view through persistent motion, we conducted simulations identical to those in Section 17, ignoring the effect of bleaching. Specifically, bound molecules were initially assigned to be immobile before transitioning between immobile and persistently moving states according to the experimentally determined rates k_{ip} and k_{pi} . Persistently moving molecules moved with a the experimentally determined average speed of 14 nm/s in a random direction, while immobile molecules remained at their current locations. According to this model it takes 45 s on average for a molecule to leave the field of view through persistent motion. This time is four times smaller than the time it takes an initially diffusive molecule to bind. We therefore reasoned that the rapid escape of bound molecules through persistent motion is responsible for the FRAP curve of non-A22-treated cells to not show recovery.

21. Quantification of expression level from fluorescence

For PAmCherry-PBP2 we counted the number of fluorescent spots observed per cell after a single activation pulse of the UV laser. For the comparison between native and overexpression levels see Fig. 1 – SI Fig. 1D.

We quantified the different levels of msfGFP-PBP2 obtained on microscope 2 (see above) by measuring the total GFP fluorescence intensity per cell, where cell outlines were obtained by segmentation of phase-contrast images using Morphometrics (SimTK) (Ursell et al., 2017). We subtracted contributions from auto-fluorescence per pixel as obtained from imaging wildtype *E. coli* (MG1655) cells. For a comparison between different induction levels see Fig. 1 – SI Fig. 8B.

For comparing the number of bound molecules: We compared PAmCherry-PBP2 track densities between native and overexpression levels. To collecting tracks, we used same activation power for the two strains and acquired 5 consecutive images with an exposure time of 1 second. Then, we did peak detection and tracking as described in Section 7. We selected tracks with at least 3 localizations to discard any mis-annotations. Density of tracks is than found by dividing the number of tracks by the area in the field of view covered with cells (Fig. 1 – SI Fig. 7C).

22. Calculation of the stoichiometry between RodA and bound PBP2 molecules

For the stoichiometry between RodA and PBP2 in wildtype cells, we used literature values obtained by ribosome profiling (Li et al., 2014). In those measurements, the stoichiometry is 1.34 and 1.36 in poor (minimal medium + glucose) and rich growth media (rich defined media), respectively. We thus assume that the mean stoichiometry of 1.35 holds for wildtype cells in our intermediate growth medium (minimal medium+glucose+casamino acids).

In the RodA depletion strain and in the parent PAmCherry-PBP2 overexpression strain, PBP2 levels are about 9-fold higher than in MG1655 according to mass spectrometry, while RodA levels are 1.5-fold above wildtype levels. However, fluorescence measurements suggest that the increase of PAmCherry-PBP2 with respect to TKL130 is only about three-fold, while PAmCherry-PBP2 is expressed between one- to two-fold above wildtype PBP2 (MG1655) in TKL130 depending on the measurement (Bocillin, DIA, PRM). Assuming that functional PAmCherry-PBP2 levels are equal to PBP2 levels in MG1655 as a conservative estimate, we then calculated the stoichiometry of PAmCherry-PBP2 and RodA in the overexpression strain according to $N_{\text{RodA}}^0/N = 1.35/3 = 0.45$, where N_{RodA} and N are the numbers of RodA and PBP2 molecules per cell, respectively.

1409 Upon CRISPRi-based repression, we estimate that RodA levels go down as a function of
1410 time t according to

$$N_{\text{RodA}}(t) = N_{\text{RodA}}^0 [(1 - f)2^{-t/t_d} + f],$$

1411 where $t_d = 90$ min is the doubling time and $f = 0.1$ is the relative residual expression level of
1412 mCherry-PBP2 after CRISPRi-based repression of the *mCherry-mrdA-mrdB* operon during
1413 steady-state growth (Vigouroux et al., 2018). This strain is equal except for the differences
1414 between PAmCherry and mCherry and for the overexpression of PBP2 from the pKC128
1415 plasmid. We then made the conservative estimate that RodA only started to drop 4h after
1416 inducing dCas9 due to any unanticipated delay of dCas9 activity. 5h after induction we
1417 observed a significant increase in cell diameter, suggesting that RodA levels had already
1418 fallen well below wildtype levels.

1419 Accordingly, we found that $N_{\text{RodA}}/N = 0.1$. With a bound fraction of $b = 0.19 \pm 0.03$, we then
1420 obtain the ratio between RodA and bound PBP2 molecules of $N_{\text{RodA}}/(bN) = 0.5 \pm 0.1$. Thus,
1421 there is likely less than one RodA molecule for every bound PBP2 molecule.

1422 **23. Model to test the contribution of diffusing PBP2 molecules to** 1423 **rod-complex activity**

1424 Cross-links with neighboring glycan strands are formed every other di-sugar subunit. Each
1425 subunit is about 1 nm long (Boal and Boal, 2012). Thus, the rate of transpeptidation
1426 corresponding to a high but common speed of MreB of 30 nm/s is $\lambda = 15/\text{s}$. Lee *et al.* argued
1427 that after forming one cross link, PBP2 would detach and diffuse in the cell envelope to find
1428 a new site for cell-wall cross-linking (Lee et al., 2014).

1429 The number of PBP2 enzymes in the cell is about between 100-300 in nutrient-rich medium
1430 and 60-75 in poor medium according to radiolabeling (Dougherty et al., 1996) or ribosome
1431 profiling (Li et al., 2014). We thus wondered whether free diffusion of such a small number of
1432 enzymes could account for the experimentally observed rate of cross-link formation, or
1433 whether free diffusion would limit this process. Alternatively, we also considered that
1434 molecules underwent facilitated diffusion along one-dimensional tracks such as the
1435 cytoskeleton MreB (Oswald et al., 2016), similarly to the phenomenon of transcription factors
1436 searching their target on chromosomal DNA (Mirny et al., 2009).

1437 We conducted overdamped Brownian-dynamics simulations of $N = 100$ enzymes
1438 [interpolating between measurements made for poor and rich media (Dougherty et al., 1996;
1439 Li et al., 2014)] in a rectangular domain of $3 \times 3 \mu\text{m}$ with periodic boundary conditions in x -
1440 and y -directions, thus approximating the cylindrical surface of a rod-like *E. coli* bacterium of
1441 $1 \mu\text{m}$ width and $3 \mu\text{m}$ length (Fig. 1 – SI Fig. 1B) and ignoring the shape of the cell poles.

1442 The overdamped Brownian motion of PBP2 in our model is governed by the Langevin
1443 equation for its position

$$\dot{\mathbf{r}} = D\boldsymbol{\zeta}$$

1444 where the dot denotes a time derivative, $D = 0.06 \mu\text{m}^2/\text{s}$ is the experimental diffusion
1445 constant, and $\boldsymbol{\zeta}$ is the zero mean Gaussian white noise random displacement originating
1446 from the solvent. Its variance is given by

$$\overline{\boldsymbol{\zeta}(t)\boldsymbol{\zeta}(t')} = 2\delta_{ij}\delta(t - t'), i, j = x, y,$$

1448 where the bar denote a noise average.

1449 A number of $n = 10$ circular cross-linking sites of diameter $a = 10$ nm are placed at random
1450 locations in the rectangular domain. Once a diffusing molecule hits any of the cross-linking
1451 sites, a cross-linking event is registered to occur. Note, that this model is based on the
1452 conservative estimate that every encounter between enzyme and cross-linking site leads to
1453 a successful reaction. To prevent rapid return of an enzyme to the same site we introduce a
1454 deterministic latency time t_{off} after every encounter during which an enzyme can diffuse but
1455 not facilitate a reaction. This latency time could reflect the typical time it takes to conduct one
1456 reaction or a combination of different microscopic effects. The reaction rate per site γ is then
1457 calculated as the mean number of enzyme-site encounters per site per total simulated time.

We consider latency times larger than 0.1 ms (Fig. 7B), a time that is needed for a PBP2 enzyme to explore an area similar to the size of an enzyme (5 nm). In this regime, the encounter rate depends only weakly on t_{off} (Fig. 7B). Thus, only a minor fraction of enzymes re-encounters the same site shortly after leaving it (Fig. 7C). Notably, the effect of t_{off} on rebinding is much weaker than in the previously studied cases of finding a membrane receptor from the cytoplasm or of binding a receptor in the 3D bulk (Mugler et al., 2012), where the probability of rebinding decays algebraically with the latency time for short times and exponentially for long times. Results are nearly independent of target numbers n (not shown).

We next considered the possibility that PBP2 undergoes facilitated diffusion along one-dimensional tracks, such as MreB filaments: MreB forms circumferentially oriented filaments of up to 1 μm in length (Ouzounov et al., 2016). PBP2 enzymes and other cell-wall proteins interact with MreB filaments (Kruse et al., 2004; Morgenstein et al., 2015), and PBP2 was observed to partially co-localize with MreB filaments (Lee et al., 2014). To test the possible influence of linear tracks on the encounter rate we extended the model introduced above by adding unidirectional filaments of length l to every rod-complex site (filaments are oriented along the y -axis). PBP2 molecules cannot cross filaments. Instead, a PBP2 molecule that encounters a filament, diffuses along the filament with the same diffusion constant D until it either a) hits the reaction site, b) reaches one of the two filament ends and returns to 2D diffusion, or c) is randomly displaced from the filament by an amount $\Delta x = 2a$ with rate k_{off} . Only after hitting the target is an enzyme inactive for the latency time t_{off} .

24. Western blotting

In order to estimate the relative amount of msfGFP-PBP2 in different strains or with different induction levels, three independent preparations of the membrane protein fraction of AV127 and TU230(attLHC943) were analyzed by western blot using a GFP primary antibody.

Cells were grown overnight in LB at 37°C and diluted 1/400 into 15 ml of M63A with varying amounts of IPTG or not depending on the strain. Three independent cultures, for each strain, were grown at 30°C with different inducer concentrations (5 to 25 μM of IPTG) for 6 hours to an OD600 approximately of 0.3. Cells were harvested by centrifugation and resuspended in 500 μl of ice-cold 1X phosphate-buffered saline (PBS) containing 10 mM EDTA. Cells were disrupted by sonication and the membrane protein fraction was collected by centrifugation (20,000 $\times g$ for 30 min at 4°C). The membrane fractions were suspended in 100 μL of 1X PBS.

The protein concentrations were determined using a Bradford-based Protein Assay (5000006, Bio-Rad) according to the instructions. Membrane protein fractions were adjusted to the same concentration with 1X PBS. 75 μl of the membrane protein extract was mixed with 25 μl of Laemmli sample buffer 4X (#1610747, Bio-Rad). Ultimately, approx. 14 μg of proteins for each sample were loaded and separated on 10 % SDS-PAGE gels (Miniprotean TGX, Bio-rad). After migration, the proteins were transferred on PVDF membranes. The membranes were incubated for 1h in TRIS-buffered saline, 0,1% Tween 20 (TBS-T) with 3% milk at room temperature and incubated in TBS-T milk 3% with anti-GFP antibodies (1/10000 dilution) ON at 4°C. Membranes were then washed three times with TBS-T and incubated for 1h with the secondary antibody tagged with horseradish peroxidase (HRP) (Goat anti-rabbit #172 1019, Bio-Rad) at room temperature. Unbound secondary antibodies were again washed out with three TBS-T washes. Signal was revealed using ECL solution (RPN2232, Amersham) and blots were imaged. Relative fold-change in signal intensity was measured in ImageJ.

25. PBP2 Mass-spectrometry

To quantify relative changes of protein levels between conditions and strains, we used Data Independent Acquisitions (DIA) following (Bruderer et al., 2017). For absolute quantification of PBP2 levels, we used a targeted proteomics approach by Parallel Reaction Monitoring (PRM) (Bourmaud et al., 2016; Gallien et al., 2012; Peterson et al., 2012).

1510 ***Preparation of E. coli whole protein extracts***

1511 Cells were collected by centrifugation (4000g, 10 minutes at 4°C) around OD₆₀₀ 0.15. For
1512 absolute quantification of PBP2, an aliquot part was taken from each culture in order to
1513 determine cell number by colony counting. Supernatant was removed and cell pellets were
1514 flash-freeze in liquid nitrogen and stored at -80°C. Cells were suspended in 250 µl of Urea
1515 buffer 8M (Sigma U4883). Cooled cells were lysed by sonication (Fisherbrand FB120)
1516 (alternating 3 cycles of 30 seconds ON with 40% amplitude and 15 seconds OFF to cool
1517 down the sample). Protein concentration was determined using a Bradford-based
1518 colorimetric assay (Bio-Rad 5000006) (Bradford, 1976) with known concentrations of bovine
1519 serum albumin (Sigma) as a standard. Proteins samples were diluted with 2x phosphate
1520 buffered saline (PBS) in order to decrease Urea concentration and be compatible with the
1521 colorimetric assay. For the quantification of absolute numbers of PBP2 we used colony
1522 counting and measured protein concentration led, which resulted in an average of 105 fg of
1523 proteins per cell.

1524 **Digestion of proteins**

1525 All protein samples were denatured in 8 M urea in Tris HCl 100 mM pH 8.0. Proteins
1526 disulfide bonds were reduced with 5 mM tris (2-carboxyethyl)phosphine (TCEP) for 20 min at
1527 23° C and further alkylated with 20 mM iodoacetamide for 30 min at room temperature in the
1528 dark. Subsequently, LysC (Promega) was added for the first digestion step (protein to Lys-C
1529 ratio = 80:1) for 3 h at 30° C. Then the sample was diluted to 1 M urea with 100 mM Tris pH
1530 8.0, and trypsin (Promega) was added to the sample at a ratio of 50:1(w/w) of protein to
1531 enzyme for 8 h at 37° C. Proteolysis was stopped by adding 1% formic acid (FA). Resulting
1532 peptides were desalted using Sep-Pak SPE cartridge (Waters) according to manufacturer
1533 instructions. Peptides elution was done using a 50% acetonitrile (ACN), 0.1% FA buffer.
1534 Eluted peptides were lyophilized and then stored until use.

1535 For Data Independent Acquisitions (DIA) and Parallel Reaction Monitoring (PRM) (see
1536 below), iRT peptides (Biognosys) were spiked into all samples as recommended by
1537 manufacturer.

1538 **Peptide Fractionation for spectral library**

1539 Peptide fractionation was done using poly(styrenedivinylbenzene) reverse phase sulfonate
1540 (SDB-RPS) stage-tips method as described in (Kulak et al., 2014; Rappsilber et al., 2007).
1541 Briefly, 3 SDB-RPS Empore discs were stacked on a P200 tip and used to fractionate 30 µg
1542 of peptides. Four serial elutions were applied as following: elution 1 (80mM Ammonium
1543 formate, 20% (v/v) ACN, 0.5% (v/v) FA), elution 2 (110mM Ammonium formate, 35% (v/v)
1544 ACN, 0.5% (v/v) FA), elution 3 (150mM Ammonium formate, 50% (v/v) ACN, 0.5% (v/v) FA)
1545 and elution 4 (80% (v/v) ACN, 5 % (v/v) ammonium hydroxide).

1546 All fractions were dried and resuspended in 0.1% formic acid before injection. For all
1547 fractions, iRT peptides were spiked as recommended by Biognosys.

1548 ***LC-MS data acquisitions***

1549 **Data Independent Acquisitions (DIA)**

1550 LC-MS/SM analysis of digested peptides was performed on an Orbitrap Q Exactive HF mass
1551 spectrometer (Thermo Fisher Scientific, Bremen) coupled to an EASY-nLC 1200 (Thermo
1552 Fisher Scientific). Peptides were loaded and separated at 250 nl/min on a home-made C18
1553 50 cm capillary column picotip silica emitter tip (75 µm diameter filled with 1.9 µm Reprosil-
1554 Pur Basic C18-HD resin, (Dr. Maisch GmbH, Ammerbuch-Entringen, Germany)) equilibrated
1555 in solvent A (2% ACN, 0.1 % FA). Peptides were eluted using a gradient of solvent B (80%
1556 ACN ,0.1 % FA) from 3% to 6% in 5 min, 6% to 29% in 130 min, 29% to 56% in 26 min, 56%
1557 to 90% in 5 min (total length of the chromatographic run was 180 min including high ACN
1558 level steps and column regeneration). Mass spectra were acquired in data-independent
1559 acquisition mode with the XCalibur 4.1.31.9 software (Thermo Fisher Scientific, Bremen).

1560 Each cycle was built up as follows: one full MS scan at resolution 30 000 (scan range
1561 between 400 and 1200 m/z), AGC was set at 3×10^6 , ion trap was set at 50 ms. All MS1 was
1562 followed by 40 isolation windows of 20 m/z, covering the MS1 range from 400 m/z to 1200

1563 m/z. The AGC target was 2×10^5 , and NCE was set to 27. All acquisitions were done in
1564 positive and profile mode.

1565 Parallel Reaction Monitoring acquisitions for absolute quantification of PBP2 (PRM)

1566 Peptides chosen and used for absolute quantification of PBP2 were based on the FASTA
1567 sequence obtained from UniprotKB database (The Uniprot Consortium, 2015) and MS
1568 evidence of identification. Peptides sequences are SGTAQVFGLK and VDNVQQTLDALR
1569 (Aqua UltimateHeavy, Thermo Fisher Scientific). Targeted peptides and their heavy forms
1570 were imported into Skyline (MacLean et al., 2010) to generate precursor ion inclusion list
1571 that also contained instrument control parameters for Xcalibur to detect peptides using PRM-
1572 MS. Information on iRT peptides (Biognosys) were also generated.

1573 Heavy peptides synthesized from PBP2 sequence were spiked at $16 \text{ fmol} \cdot \mu\text{l}^{-1}$ in each sample.
1574 Each sample was injected at a known concentration with iRT peptides (as recommended by
1575 Biognosys) and 50 fmol of heavy peptides. Quantity of peptide injected on column was
1576 controlled by UV absorbance at 280 nm and tryptophan absorbance.

1577 PRM was performed on an Orbitrap Q Exactive HF mass spectrometer (Thermo Fisher
1578 Scientific, Bremen) coupled to an EASY-nLC 1200 (Thermo Fisher Scientific). Peptides were
1579 loaded and separated at $250 \text{ nl} \cdot \text{min}^{-1}$ on a home-made C18 50 cm capillary column picotip
1580 silica emitter tip ($75 \mu\text{m}$ diameter filled with $1.9 \mu\text{m}$ Reprosil-Pur Basic C18-HD resin, (Dr.
1581 Maisch GmbH, Ammerbuch-Entringen, Germany) equilibrated in solvent A (2% ACN, 0.1 %
1582 FA). Peptides were eluted using a gradient of solvent B (80% ACN, 0.1 % FA) from 5% to
1583 10% in 1 min, 10% to 30% in 82 min, 30% to 50% in 5 min, 50% to 95% in 5 min (total
1584 length of the chromatographic run was 105 min including high ACN level steps and column
1585 regeneration). Mass spectra were acquired XCalibur 4.1.31.9 software (Thermo Fisher
1586 Scientific, Bremen). The acquisition method combined a full scan method with a time-
1587 scheduled sequential PRM method. For the full MS, a scan range of 350 to 1500 m/z, an
1588 orbitrap resolution of 60000, and an AGC value of a 3×10^6 were used. An orbitrap resolution
1589 of 60000, a maximum IT set at 110 ms, an isolation window selection of 1.2 m/z, AGC target
1590 was 2×10^5 and NCE fixed at 28 were used. Targeted, heavy and retention time peptides (iRT
1591 peptides, Biognosys) were listed in an inclusion list and monitored.

1592 **Data analysis**

1593 Data Analysis for spectrum library building and DDA analysis of Co-IP

1594 For spectral library purposes and DDA experiments, MaxQuant (Tyanova et al., 2016a)
1595 1.5.5.3 was used. Raw data were analyzed against an *E. coli* database (6071 entries,
1596 downloaded from Uniprot on 10/03/2016).

1597 The following search parameters were applied: carbamidomethylation of cysteines was set
1598 as a fixed modification, oxidation of methionine and protein N-terminal acetylation were set
1599 as variable modifications. The mass tolerances in MS and MS/MS were set to 5 ppm and 20
1600 ppm respectively. Maximum peptide charge was set to 7 and 7 amino acids were required
1601 as minimum peptide length. A false discovery rate of 1% was set up for both protein and
1602 peptide levels.

1603 Data analysis was done mainly using Excel and Perseus environment (Tyanova et al.,
1604 2016b).

1605 Data analysis for DIA acquisitions

1606 DIA experiments were analyzed using Spectronaut X (v. 11 Biognosys AG). Dynamic mass
1607 tolerance at the MS1 and MS2 levels was employed. The XIC RT Extraction Window was
1608 set to Dynamic with a correction factor of 1. Calibration mode was set to automatic with
1609 nonlinear iRT calibration and precision iRT enabled. Decoys were generated using the
1610 scrambled method and a dynamic limit (default settings). P value estimation was performed
1611 using a kernel density estimator. Interference correction was enabled with no proteotypicity
1612 filter. Major grouping was by Protein-Group ID, and minor grouping was by stripped
1613 sequence. The major group quantity was mean peptide quantity. The major group top N was
1614 enabled with a minimum of 1 and a maximum of 3. Minor group quantity was mean
1615 precursor quantity. The minor group top N was enabled with a minimum of 1 and a

1616 maximum of 3. The quantity MS-Level was MS2, and quantity type was area. Q value was
1617 used for data filtering. Cross run normalization was enabled with Q value sparse row
1618 selection and local normalization. The default labeling type was label-free with no profiling
1619 strategy and unify peptide peaks not enabled. The protein inference workflow was set to
1620 automatic.

1621 PRM data analysis

1622 Raw mass spectrometry data were exported to Skyline-daily (version 4.1.1.18179) for
1623 identification of transitions and peak area integration. Data were exported in .csv file format
1624 and analyzed in Excel.

1625 **Bibliography**

1626 Bendežú, F.O., and Boer, P.A.J. de (2008). Conditional Lethality, Division Defects,
1627 Membrane Involution, and Endocytosis in mre and mrd Shape Mutants of Escherichia coli. *J.*
1628 *Bacteriol.* *190*, 1792–1811.

1629 Bendežú, F.O., Hale, C.A., Bernhardt, T.G., and de Boer, P.A.J. (2009). RodZ (YfgA) is
1630 required for proper assembly of the MreB actin cytoskeleton and cell shape in E. coli. *The*
1631 *EMBO Journal* *28*, 193–204.

1632 Boal, D., and Boal, D.H. (2012). *Mechanics of the Cell* (Cambridge University Press).

1633 de Boer, P.A., Crossley, R.E., and Rothfield, L.I. (1990). Central role for the Escherichia coli
1634 minC gene product in two different cell division-inhibition systems. *Proceedings of the*
1635 *National Academy of Sciences* *87*, 1129–1133.

1636 Bourmaud, A., Gallien, S., and Domon, B. (2016). Parallel reaction monitoring using
1637 quadrupole-Orbitrap mass spectrometer: Principle and applications. *PROTEOMICS* *16*,
1638 2146–2159.

1639 Bradford, M.M. (1976). A rapid and sensitive method for the quantitation of microgram
1640 quantities of protein utilizing the principle of protein-dye binding. *Analytical Biochemistry* *72*,
1641 248–254.

1642 Bruderer, R., Bernhardt, O.M., Gandhi, T., Xuan, Y., Sondermann, J., Schmidt, M., Gomez-
1643 Varela, D., and Reiter, L. (2017). Optimization of Experimental Parameters in Data-
1644 Independent Mass Spectrometry Significantly Increases Depth and Reproducibility of
1645 Results. *Molecular & Cellular Proteomics* *16*, 2296–2309.

1646 Cho, H., Wivagg, C.N., Kapoor, M., Barry, Z., Rohs, P.D.A., Suh, H., Marto, J.A., Garner,
1647 E.C., and Bernhardt, T.G. (2016). Bacterial cell wall biogenesis is mediated by SEDS and
1648 PBP polymerase families functioning semi-autonomously. *Nat. Microbiol* *1*, 16172–16172.

1649 Crocker, J.C., and Grier, D.G. (1996). Methods of Digital Video Microscopy for Colloidal
1650 Studies. *Journal of Colloid and Interface Science* *179*, 298–310.

1651 Cui, L., Vigouroux, A., Rousset, F., Varet, H., Khanna, V., and Bikard, D. (2018). A CRISPRi
1652 screen in E. coli reveals sequence-specific toxicity of dCas9. *Nature Communications* *9*,
1653 1912.

1654 Datsenko, K.A., and Wanner, B.L. (2000). One-step inactivation of chromosomal genes in
1655 Escherichia coli K-12 using PCR products. *Proc Natl Acad Sci USA* *97*, 6640–6645.

1656 Dougherty, T.J., Kennedy, K., Kessler, R.E., and Pucci, M.J. (1996). Direct quantitation of
1657 the number of individual penicillin-binding proteins per cell in Escherichia coli. *Journal of*
1658 *Bacteriology* *178*, 6110–6115.

1659 Edelstein, A., Amodaj, N., Hoover, K., Vale, R., and Stuurman, N. (2010). Computer control
1660 of microscopes using μ Manager., Computer Control of Microscopes using μ Manager. Curr
1661 Protoc Mol Biol *Chapter 14, CHAPTER*, Unit14.20, Unit14.20-Unit14.20.

1662 Gallien, S., Duriez, E., Crone, C., Kellmann, M., Moehring, T., and Domon, B. (2012).
1663 Targeted Proteomic Quantification on Quadrupole-Orbitrap Mass Spectrometer. *Molecular &*
1664 *Cellular Proteomics* *11*, 1709–1723.

1665 Hansen, A.S., Woringer, M., Grimm, J.B., Lavis, L.D., Tjian, R., and Darzacq, X. (2018).
1666 Robust model-based analysis of single-particle tracking experiments with Spot-On. *ELife* *7*,
1667 e33125.

1668 Kocaoglu, O., Calvo, R.A., Sham, L.-T., Cozy, L.M., Lanning, B.R., Francis, S., Winkler,
1669 M.E., Kearns, D.B., and Carlson, E.E. (2012). Selective Penicillin-Binding Protein Imaging
1670 Probes Reveal Substructure in Bacterial Cell Division. *ACS Chem Biol* *7*, 1746–1753.

1671 Kruse, T., Bork-Jensen, J., and Gerdes, K. (2004). The morphogenetic MreBCD proteins of
1672 *Escherichia coli* form an essential membrane-bound complex. *Molecular Microbiology* *55*,
1673 78–89.

1674 Kuhlman, T.E., and Cox, E.C. (2010). Site-specific chromosomal integration of large
1675 synthetic constructs. *Nucleic Acids Res* *38*, e92.

1676 Kulak, N.A., Pichler, G., Paron, I., Nagaraj, N., and Mann, M. (2014). Minimal, encapsulated
1677 proteomic-sample processing applied to copy-number estimation in eukaryotic cells. *Nature*
1678 *Methods* *11*, 319–324.

1679 Lee, T.K., Tropini, C., Hsin, J., Desmarais, S.M., Ursell, T.S., Gong, E., Gitai, Z., Monds,
1680 R.D., and Huang, K.C. (2014). A dynamically assembled cell wall synthesis machinery
1681 buffers cell growth. *Proceedings of the National Academy of Sciences* *111*, 4554–4559.

1682 Li, G.-W., Burkhardt, D., Gross, C., and Weissman, J.S. (2014). Quantifying Absolute
1683 Protein Synthesis Rates Reveals Principles Underlying Allocation of Cellular Resources. *Cell*
1684 *157*, 624–635.

1685 MacLean, B., Tomazela, D.M., Shulman, N., Chambers, M., Finney, G.L., Frewen, B., Kern,
1686 R., Tabb, D.L., Liebler, D.C., and MacCoss, M.J. (2010). Skyline: an open source document
1687 editor for creating and analyzing targeted proteomics experiments. *Bioinformatics* *26*, 966–
1688 968.

1689 Miller, J.H. (1972). Experiments in molecular genetics (Cold Spring Harbor Laboratory).

1690 Mirny, L., Slutsky, M., Wunderlich, Z., Tafvizi, A., Leith, J., and Kosmrlj, A. (2009). How a
1691 protein searches for its site on DNA: the mechanism of facilitated diffusion. *J. Phys. A: Math.*
1692 *Theor.* *42*, 434013–434013.

1693 Morgenstein, R.M., Bratton, B.P., Nguyen, J.P., Ouzounov, N., Shaevitz, J.W., and Gitai, Z.
1694 (2015). RodZ links MreB to cell wall synthesis to mediate MreB rotation and robust
1695 morphogenesis. *Proceedings of the National Academy of Sciences* *112*, 12510–12515.

1696 Mugler, A., Bailey, A.G., Takahashi, K., and ten Wolde, P.R. (2012). Membrane clustering
1697 and the role of rebinding in biochemical signaling. *Biophysical Journal* *102*, 1069–1078.

1698 Oswald, F., Varadarajan, A., Lill, H., Peterman, E.J.G., and Bollen, Y.J.M. (2016). MreB-
1699 Dependent Organization of the *E. coli* Cytoplasmic Membrane Controls Membrane Protein
1700 Diffusion. *Biophysical Journal* *110*, 1139–1149.

1701 Ouzounov, N., Nguyen, J.P., Bratton, B.P., Jacobowitz, D., Gitai, Z., and Shaevitz, J.W.
1702 (2016). MreB Orientation Correlates with Cell Diameter in *Escherichia coli*. *Biophysical*
1703 *Journal* *111*, 1035–1043.

1704 Peterson, A.C., Russell, J.D., Bailey, D.J., Westphall, M.S., and Coon, J.J. (2012). Parallel
 1705 Reaction Monitoring for High Resolution and High Mass Accuracy Quantitative, Targeted
 1706 Proteomics. *Molecular & Cellular Proteomics* *11*, 1475–1488.

1707 Rappsilber, J., Mann, M., and Ishihama, Y. (2007). Protocol for micro-purification,
 1708 enrichment, pre-fractionation and storage of peptides for proteomics using StageTips.
 1709 *Nature Protocols* *2*, 1896–1906.

1710 Rohs, P.D.A., Buss, J., Sim, S.I., Squyres, G.R., Srisuknimit, V., Smith, M., Cho, H., Sjodt,
 1711 M., Kruse, A.C., Garner, E.C., et al. (2018). A central role for PBP2 in the activation of
 1712 peptidoglycan polymerization by the bacterial cell elongation machinery. *PLOS Genetics* *14*,
 1713 e1007726.

1714 Salje, J., van den Ent, F., de Boer, P., and Löwe, J. (2011). Direct Membrane Binding by
 1715 Bacterial Actin MreB. *Molecular Cell* *43*, 478–487.

1716 Schneider, C.A., Rasband, W.S., and Eliceiri, K.W. (2012). NIH Image to ImageJ: 25 years
 1717 of image analysis.

1718 Sliusarenko, O., Heinritz, J., Emonet, T., and Jacobs-Wagner, C. (2011). High-throughput,
 1719 subpixel precision analysis of bacterial morphogenesis and intracellular spatio-temporal
 1720 dynamics. *Molecular Microbiology* *80*, 612–627.

1721 van Teeffelen, S., Wang, S., Furchtgott, L., Huang, K.C., Wingreen, N.S., Shaevitz, J.W.,
 1722 and Gitai, Z. (2011). The bacterial actin MreB rotates, and rotation depends on cell-wall
 1723 assembly. *Proceedings of the National Academy of Sciences* *108*, 15822–15827.

1724 The Uniprot Consortium (2015). UniProt: a hub for protein information. *Nucleic Acids Res*
 1725 *43*, D204–D212.

1726 Tyanova, S., Temu, T., and Cox, J. (2016a). The MaxQuant computational platform for mass
 1727 spectrometry-based shotgun proteomics. *Nature Protocols* *11*, 2301–2319.

1728 Tyanova, S., Temu, T., Sinitcyn, P., Carlson, A., Hein, M.Y., Geiger, T., Mann, M., and Cox,
 1729 J. (2016b). The Perseus computational platform for comprehensive analysis of (prote)omics
 1730 data. *Nature Methods* *13*, 731–740.

1731 Ursell, T., Lee, T.K., Shiomi, D., Shi, H., Tropini, C., Monds, R.D., Colavin, A., Billings, G.,
 1732 Bhaya-Grossman, I., Broxton, M., et al. (2017). Rapid, precise quantification of bacterial
 1733 cellular dimensions across a genomic-scale knockout library. *BMC Biology* *15*, 17.

1734 Vigouroux, A., Oldewurtel, E., Cui, L., Bikard, D., and Teeffelen, S. van (2018). Tuning
 1735 dCas9's ability to block transcription enables robust, noiseless knockdown of bacterial
 1736 genes. *Molecular Systems Biology* *14*, e7899.

1737
 1738

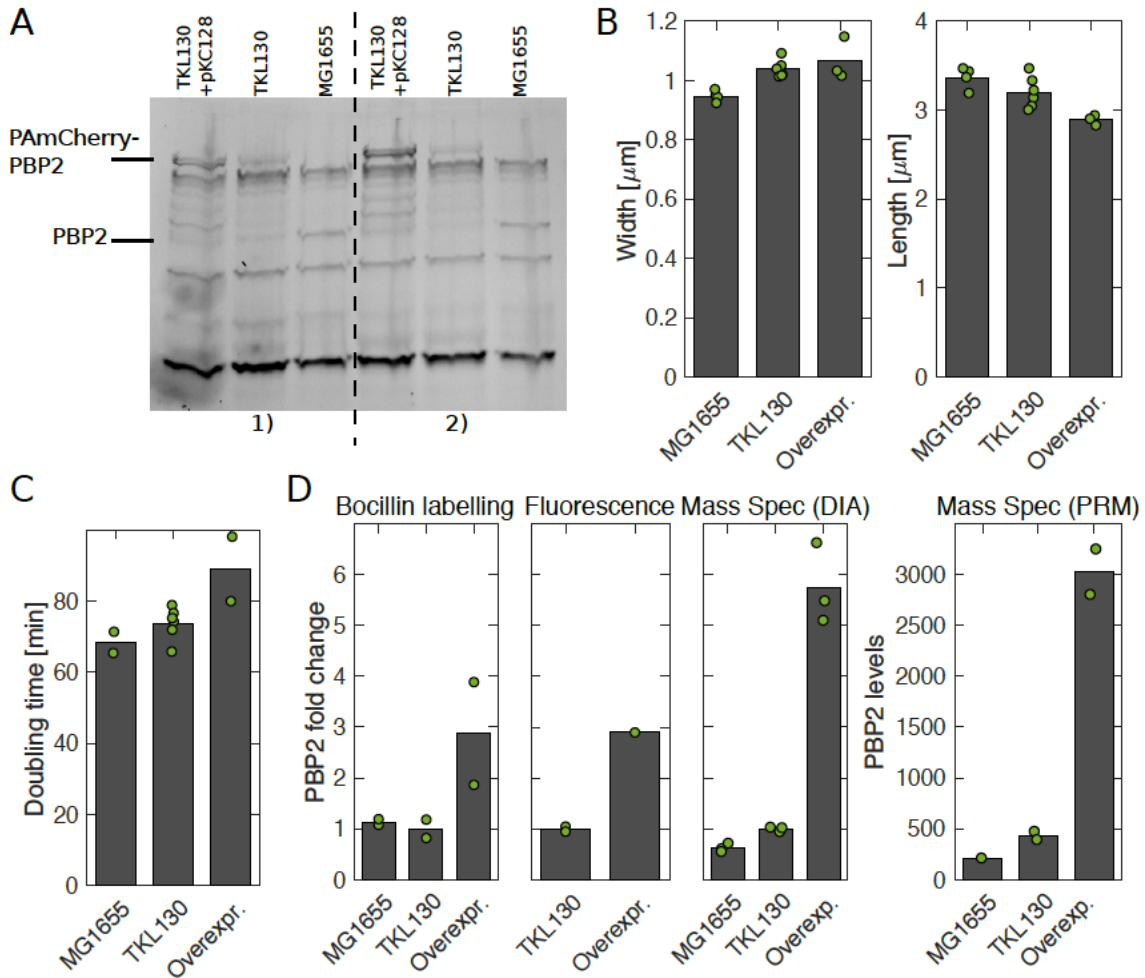


Figure 1-figure supplement 1. Comparison of PBP2-PAmCherry expressing cells and WT.

(A) Bocillin-binding assay to compare expression levels of PBP2 in the wild-type strain (MG1655), the strain expressing PBP2-PAmCherry from the native locus (TKL130), and the strain overexpressing PBP2-PAmCherry (TKL130/pKC128). Quantification in (D).

(B) Average cell dimensions obtained by phase-contrast microscopy and computational image segmentation.

(C) Average doubling times during steady-state exponential growth in batch culture (from OD600).

(D) Different methods to compare PBP2 expression levels in different strains (from left to right): Bocillin labeling (from A), single-cell fluorescence levels measured in epi-fluorescence mode, mass spectrometry [Data Independent Acquisitions (DIA) and Parallel Reaction Monitoring (PRM)]. For the first three methods, PBP2 levels are normalized by the corresponding value in TKL130. For PRM, we obtained absolute numbers of proteins per cell by comparing to reference peptides and colony counting. With both mass spectrometry methods, we observe a higher fold-change than through the other methods. Dots represent biological replicates.

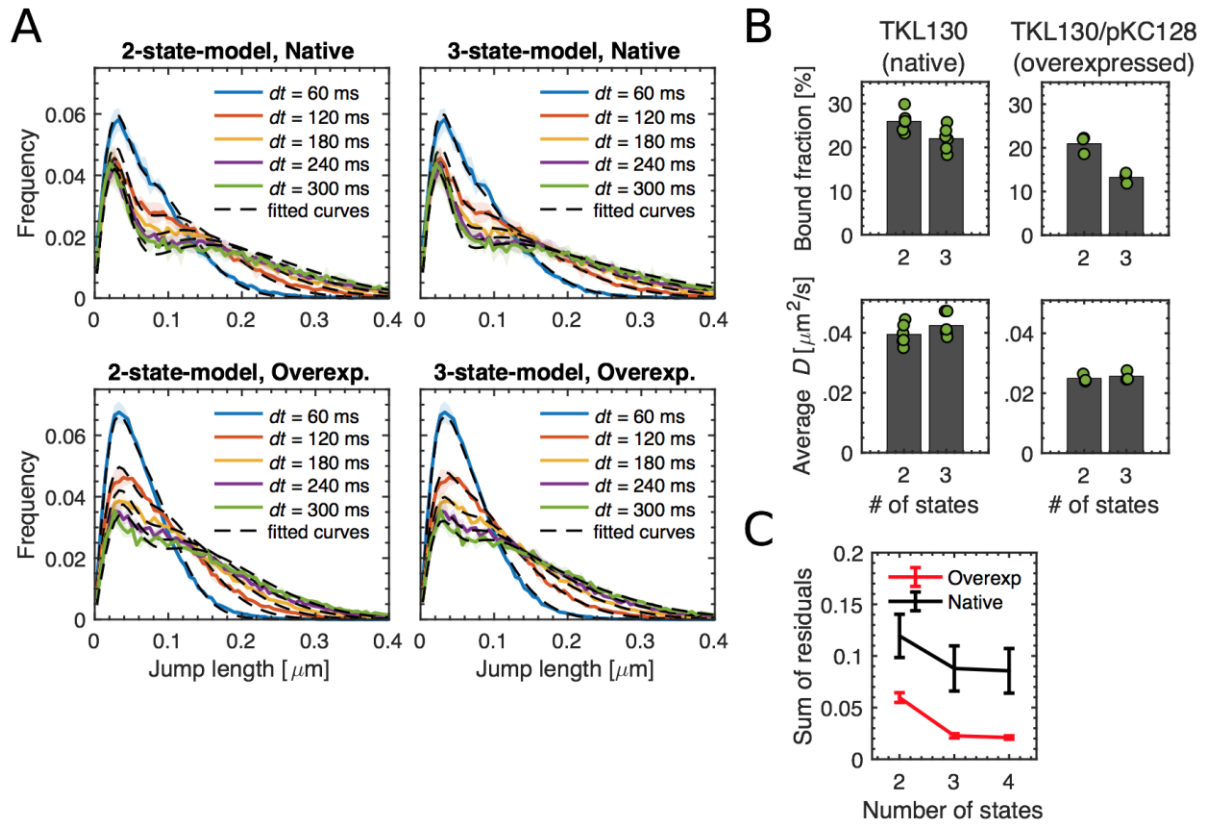


Figure 1-figure supplement 2. Comparing 2- and 3-state-diffusion models to fit experimental data through Spot-On.

(A) Probability distributions of single-molecule jump lengths (solid lines, colored) and fit (dashed, black) using a two-state (left) or three-state (right) diffusion model for different time intervals for native levels (TKL130) and for over-expression (TKL130/pKC128) of PBP2-PAmCherry. Shaded regions show standard deviations between biological replicates.

(B) Comparison of bound fractions and average diffusion constants acquired by fitting two-state and three-state diffusion models shown in (A). Dots represent biological replicates.

(C) Normalized sum of residuals found by using multi-state models with Spot-On. Error bars show standard error between biological replicates.

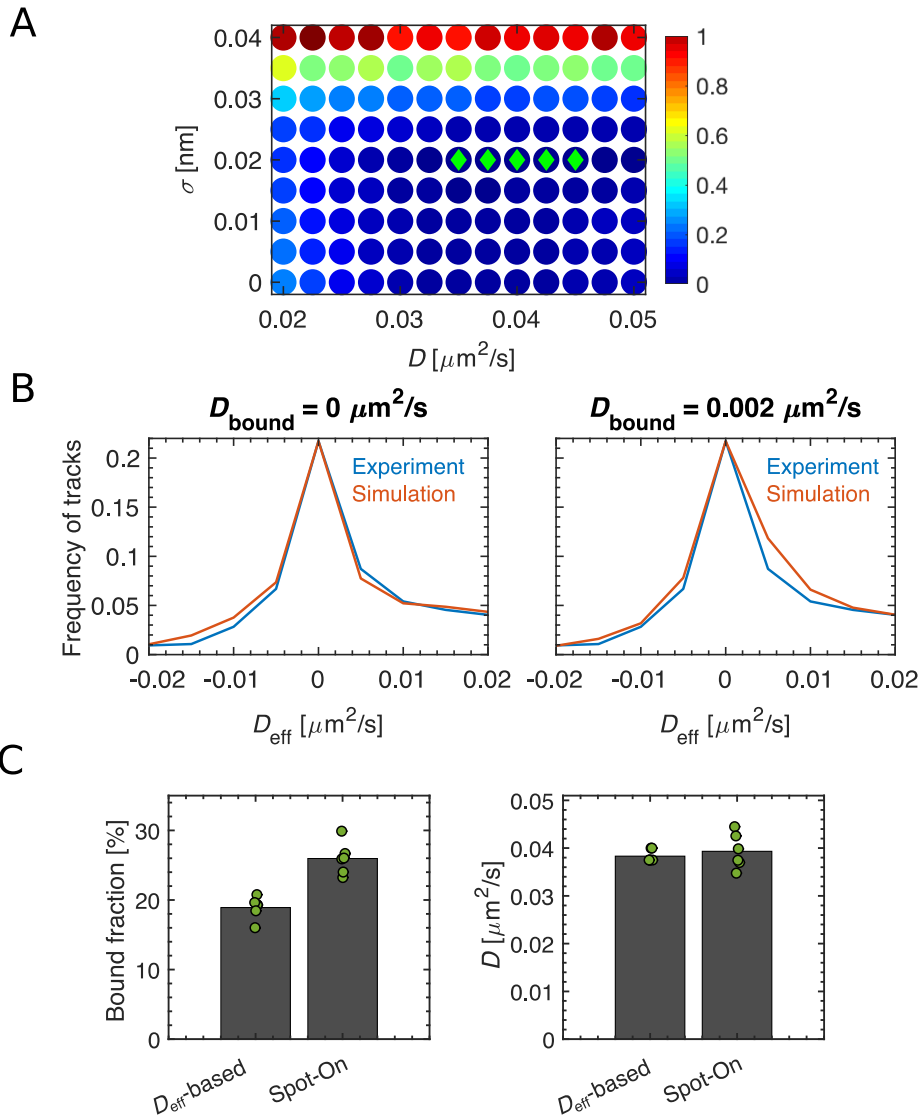


Figure 1–figure supplement 3. An alternative approach to fit a two-state diffusion model, based on the distribution of effective diffusion constants.

(A) Heat map of sum of squared differences (RSS) between the D_{eff} distributions of single-track effective diffusion constants D_{eff} obtained from experimental data or computational simulations of a two-state model, using different model parameters D (diffusion constant of the diffusive fraction) and σ (localization precision). Parameter sets giving the lowest 5 RSS values are shown with green diamonds. Best fit is given by $D = 0.04 \mu\text{m}^2/\text{s}$ and $\sigma = 20 \text{ nm}$.

(B) We verified that the non-diffusive population was indeed not diffusing, with $D_{\text{bound}} = 0 \mu\text{m}^2/\text{s}$ (left), while a finite diffusion constant $D_{\text{bound}} > 0.002 \mu\text{m}^2/\text{s}$ gives poor agreement between simulation and experiment. Here, the experimental D_{eff} distribution is the mean of 6 biological replicates.

(C) We compared the results of our method with the Spot-On code (2-state model) in TKL130 (native levels) and TKL130/pKC128 (overexpression), respectively.

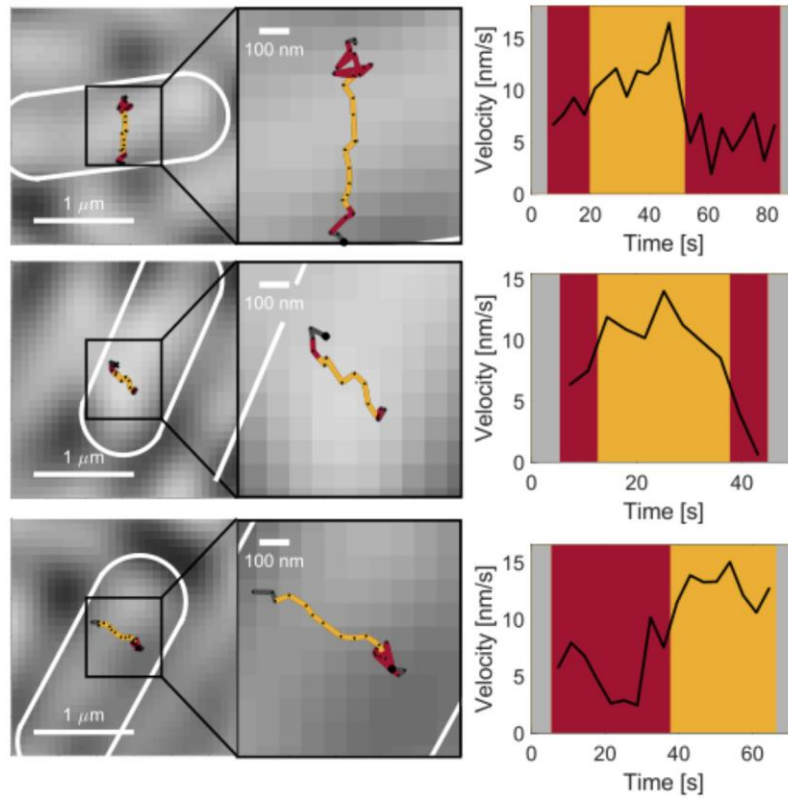


Figure 1-figure supplement 4. Transitions between immobile and persistent states.

Example tracks and velocity as a function of time for example tracks that show transitions between persistent and immobile states.

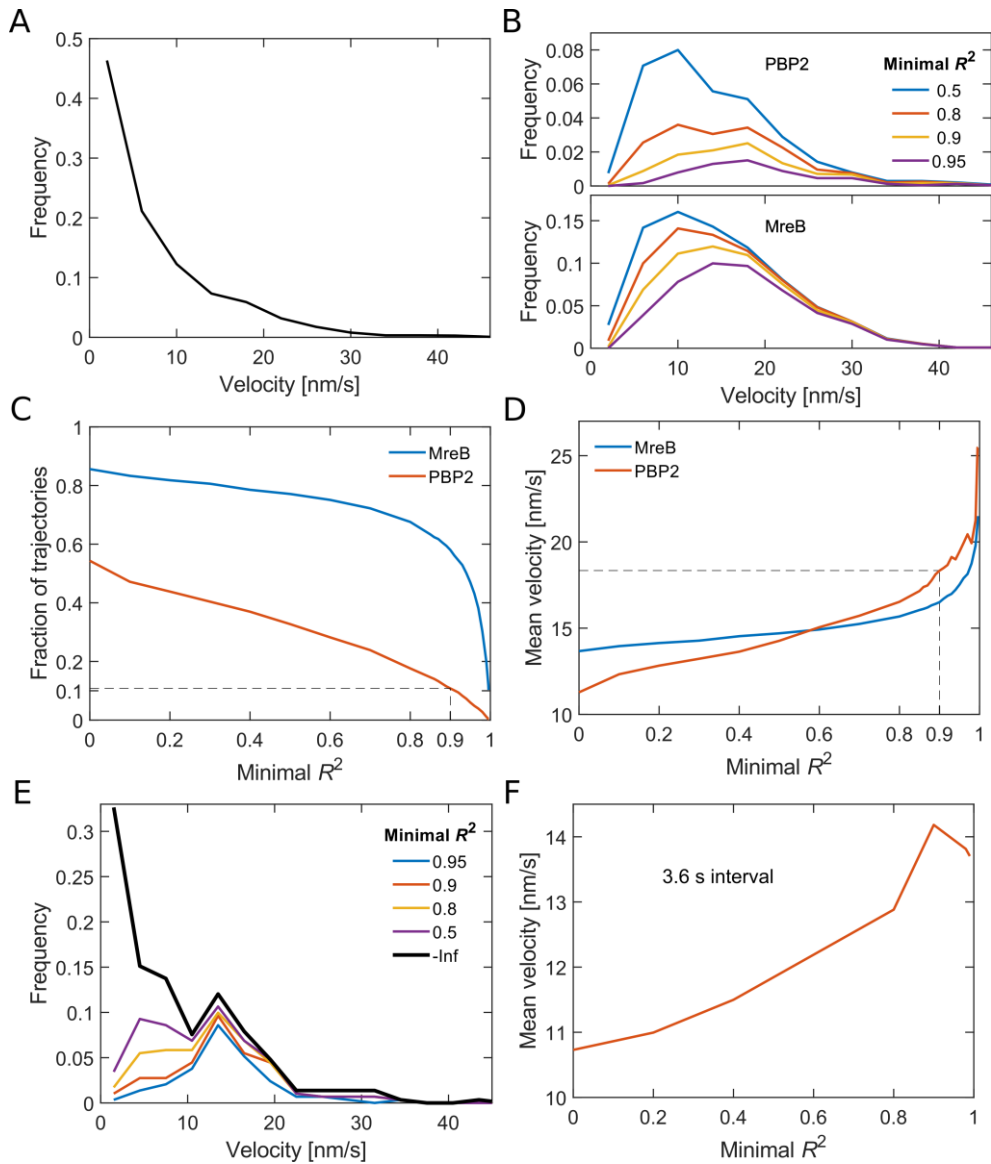


Figure 1-figure supplement 5. Analysis of bound PAmCherry-PBP2 molecules.

(A) Velocity distribution of all PBP2 tracks measured with 1 s intervals. The velocity of individual tracks was determined by fitting a quadratic function to the MSD.

(B) Velocity distributions for directed trajectories of PBP2 and MreB as found by selecting for an increased goodness of fit measured by R^2 of a quadratic function to the MSD.

(C) The stricter the goodness of fit criterion (minimal R^2) the less trajectories contribute to the mean track velocity.

(D) The mean velocity increases with increasing minimum R^2 . The dashed line indicates the value chose for the distributions in Fig. 1.

(E-F) The same analysis applied on 4-step segments of trajectories measured with 3.6 s intervals delivers smaller mean velocities, likely because fast trajectories reside for a shorter amount of time in the field of view.

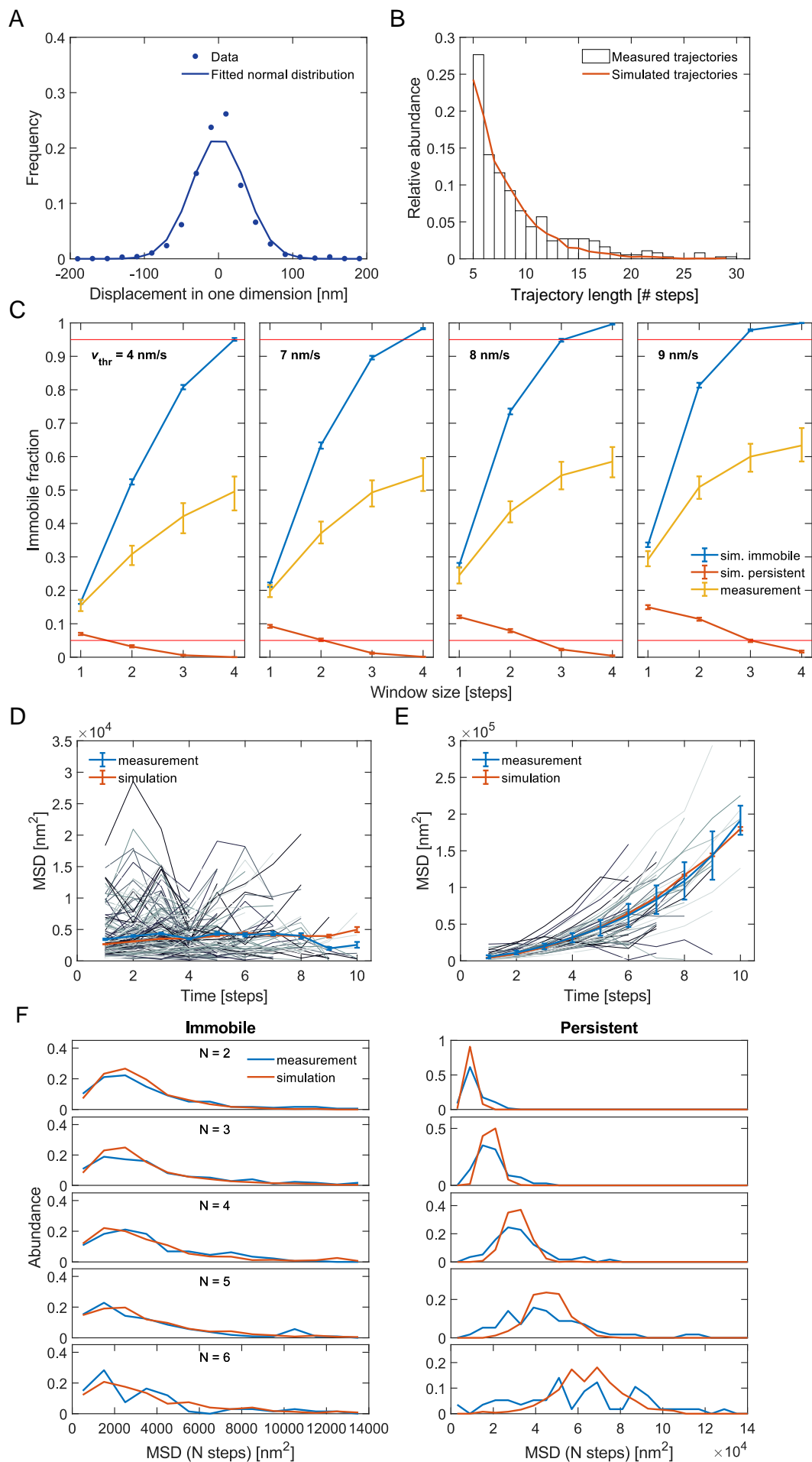


Figure 1—figure supplement 6. Quantitative analysis of persistent and immobile states based on computational simulations.

1807 **(A)** Distribution of measured single-step displacements in one dimension. A fit of a normal
1808 distribution to the data delivers a standard deviation of 36 nm, which corresponds to a
1809 localization error of single localization events of 25 nm.

1810 **(B)** We computationally simulated trajectories such that the length distribution of the
1811 simulated trajectories resembles the one from measured trajectories.

1812 **(C)** Fraction of immobile segments measured in simulations of immobile (blue) or persistent
1813 (red) molecules and in experimentally measured tracks (yellow) as a function of the moving-
1814 average window size and for different velocity thresholds. The red horizontal lines signify 5%
1815 and 95% probability thresholds, respectively. Error bars are from bootstrapping. For a
1816 window size of 4 steps and a velocity threshold of 8 nm/s the rate of wrong annotation is
1817 smaller than 1% both in simulations of purely persistent or immobile molecules. For pairs of
1818 w and v_{thr} that lead to high accuracy of the determination of immobile and persistent
1819 segments the immobile fraction of the experimental data shows similar results.

1820 **(D-E)** MSD's of single-track segments (gray lines) classified as **(D)** immobile or **(E)**
1821 persistent compared to the MSD of all respective segments (blue line). For simulated
1822 trajectories that can switch between the immobile and the persistent state (simulated with v
1823 $= 12 \text{ nm/s}$, $k_{\text{ip}} = 0.015 \text{ s}^{-1}$, $k_{\text{pi}} = 0.021 \text{ s}^{-1}$) we find a similar behavior of the MSD curves (red
1824 line).

1825 **(F)** Distribution of MSD's of immobile and persistent segments for different numbers of steps
1826 N .
1827

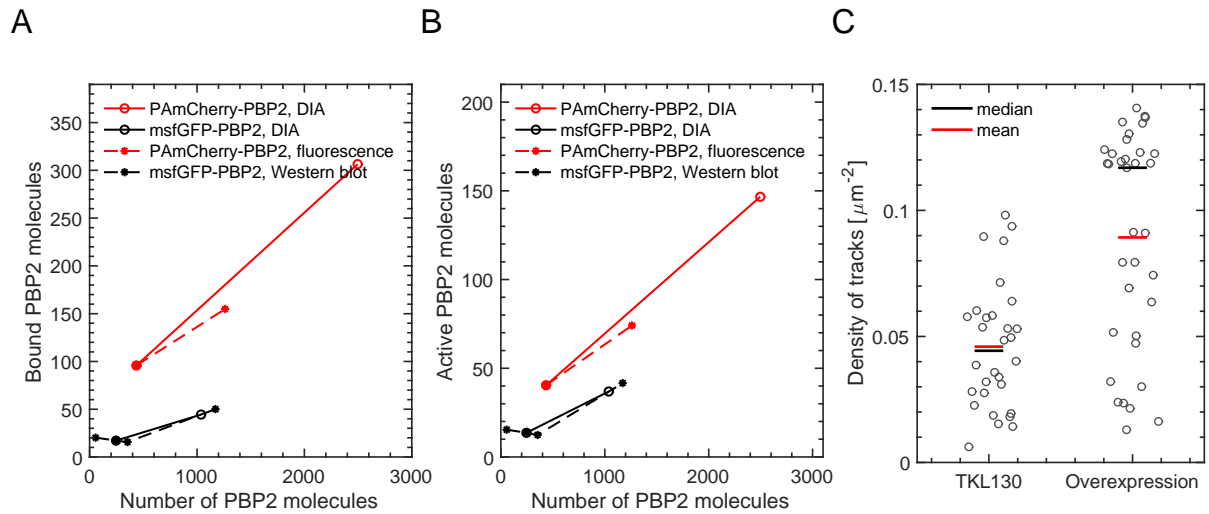


Figure 1-figure supplement 7. Number of bound PBP2 molecules increases with increasing PBP2 levels.

(A-B) Number of bound PBP2 molecules ($N_{\text{bound}} = N_{\text{PBP2}}b$) **(A)** and active PBP2 molecules ($N_{\text{active}} = N_{\text{PBP2}}bp$) **(B)** as a function of the number of PBP2 molecules per cell (N_{PBP2}). b and p are the bound and persistent fractions of molecules, respectively. Since DIA, fluorescence, and Western Blot results only gave relative changes of PBP2 numbers, we used PRM values for TKL130 (for PAmCherry-PBP2) or for TU230(attLHC943) with 5 μM IPTG induction (for msfGFP-PBP2), respectively.

(C) Density of tracks obtained by slow tracking for TKL130 and TKL130/pKC128, using same photo-activation and imaging conditions. Dots represent single fields of view (40x40 μm). Despite variations between different fields of view, the fold-change of the median is of the same order as the relative change of bound molecules obtained in (A).

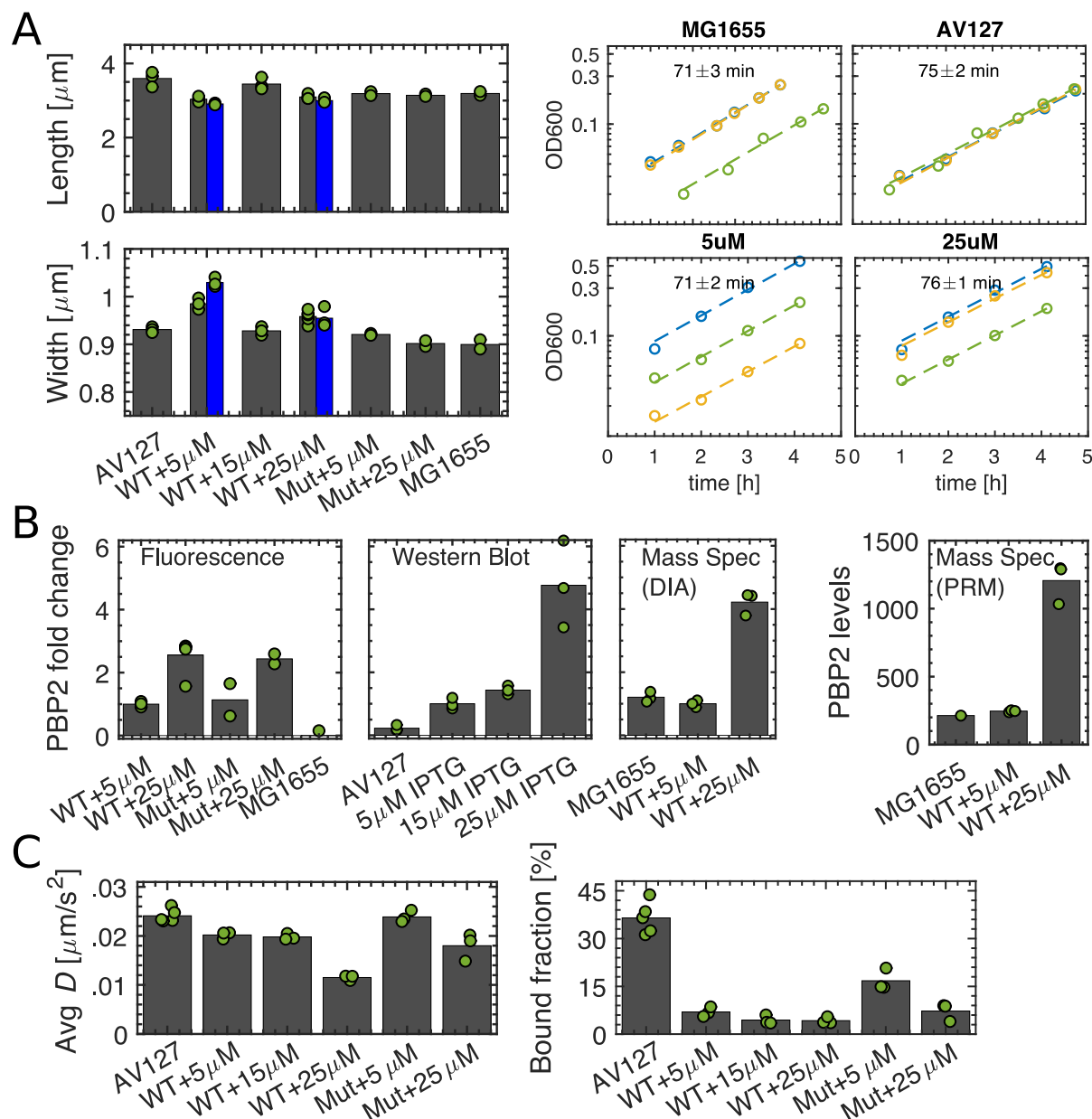


Figure 1-figure supplement 8. Comparison of AV127, msfGFP-PBP2 (TU230(attLHC943)), msfGFP-PBP2(L61R) (TU230(attLHC943)), and WT strains.

(A) Length (top left), width (bottom left), and growth curves (right) of the strains carrying msfGFP-PBP2 (AV127 or IPTG-inducible) and msfGFP-PBP2(L61R) (labeled 'Mut') for different induction levels in comparison to MG1655. Gray and blue bars show cell dimensions after 6 and 10 hours of growth, respectively (see also Fig. 1–SI Fig. 9). Doubling times are obtained from exponential fits (dashed lines) to three biological replicates (different colors).

(B) PBP2 fold changes acquired from epi-fluorescence images, GFP-Western Blotting, and mass spectrometry measurements (DIA and PRM). The values are normalized by the value acquired from 5 μM IPTG induction except for PRM counts. PRM measurements combined with colony counting yield absolute numbers of proteins per cell.

(C) Average diffusion constants and bound fractions. Gray bars show data after 6 hours of growth. Dots represent biological replicates.

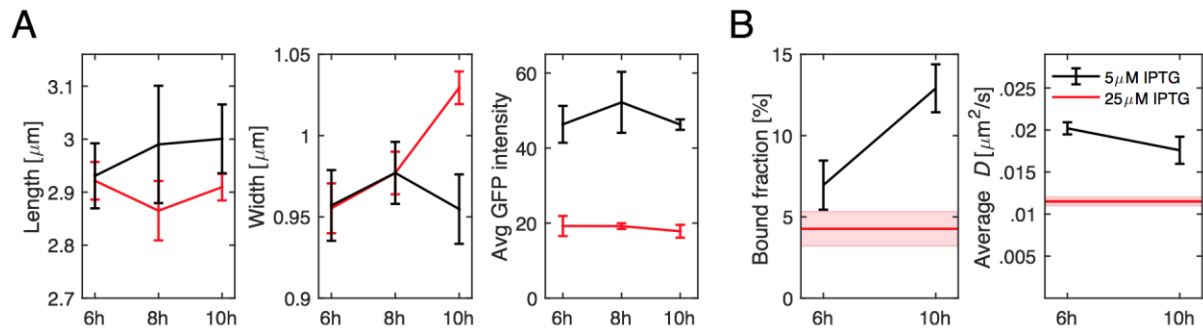


Figure 1-figure supplement 9. Time-dependent effect of low msfGFP-PBP2 expression.

(A) Cell length, width, and GFP intensity as a function of time of TU230(attLHC943) cells for 2 different induction levels of 5 μM IPTG (black) and 25 μM IPTG (red).

(B) Bound fractions and average diffusion constants. Red lines in (B) indicate the values measured for 25 μM induction during steady-state growth. Shaded areas and error bars show standard deviation between at least 3 technical replicates.

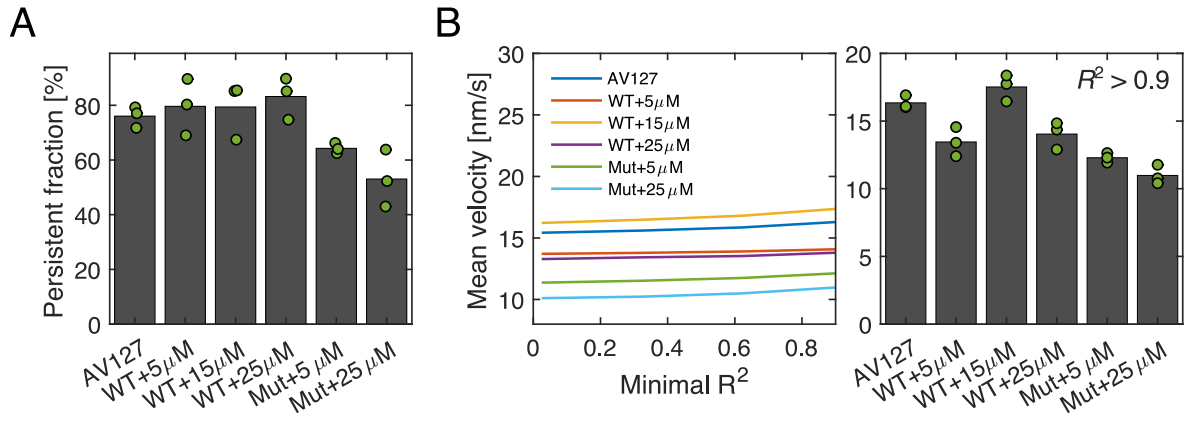


Figure 1–figure supplement 10. Low-frequency tracking of msfGFP-PBP2 and msfGFP-PBP2(L61R) cells under different induction levels.

(A) Persistent fractions for different expression levels of msfGFP-PBP2 and msfGFP-PBP2(L61R).

(B) Left. Mean velocity as a function of minimal R^2 , which are obtained from a quadratic fit to single-track MSD's of the form $y = a + bx^2$. **Right.** Mean velocity of tracks, which satisfy $R^2 > 0.9$. Dots represent biological replicates.

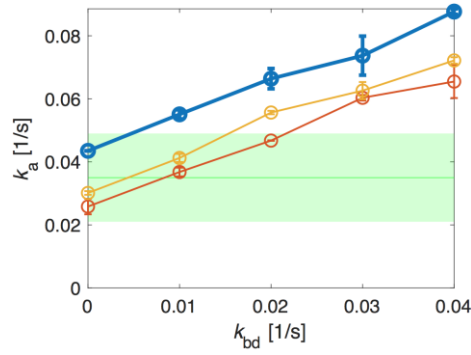


Figure 2—figure supplement 1. Determination of an upper limit of the unbinding rate k_{bd} through simulations.

Simulations of track-length distributions reveal the apparent track termination rate k_a as a function of the unbinding rate k_{bd} for different transition simulated rates k_{ip} , k_{pi} . Top: $k_{ip} = 0.063/s$, $k_{pi} = 0.0086/s$ (experimentally measured rates, leading to a bound fraction of 88%); middle and bottom (thin solid lines): $k_{ip} = 0.063/s$, $k_{pi} = 0.0158/s$; $k_{ip} = 0.033/s$, $k_{pi} = 0.0086/s$. For the thin solid lines, we adjusted either of the two rates to yield the experimentally measured bound fraction of 80%. Comparison with the experimentally measured apparent unbinding rate (green) allows us to infer an upper bound for the unbinding rate $k_{bd} < 0.03/s$. Shaded area: 95% confidence interval.

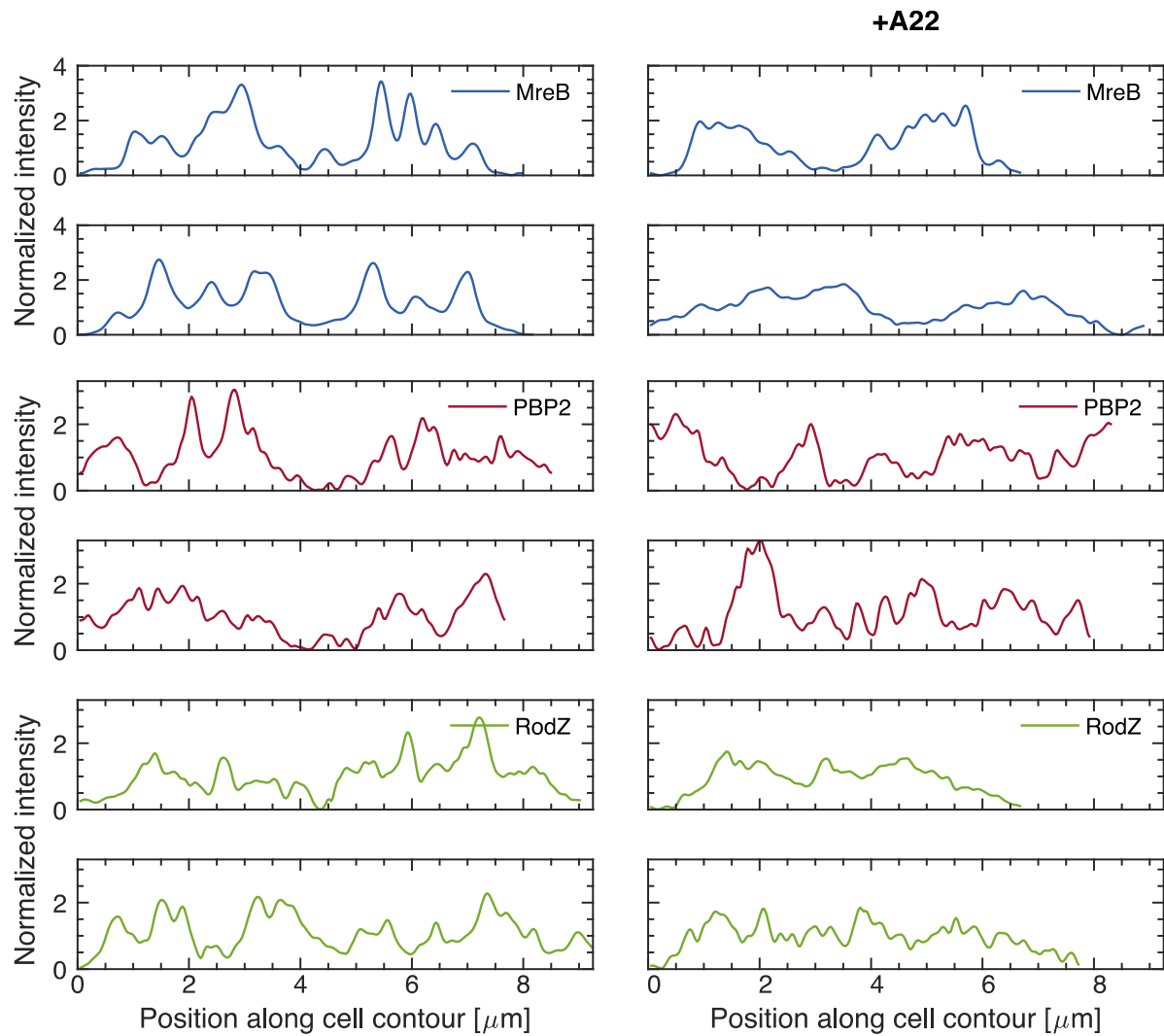


Figure 3—figure supplement 1. Sample fluorescence profiles on cell boundaries as in Fig. 3B.

Fluorescence profiles along contours of different cells carrying mCherry-PBP2, MreB-msfGFP, or GFP-RodZ fusions for untreated (**left**) or A22 treated cells (50 µg/ml) (**right**), obtained in the same way as in Fig. 3A, B. Intensities are normalized by the median value and smoothened with a Gauss filter with standard deviation of 33 nm (0.5 pixel).

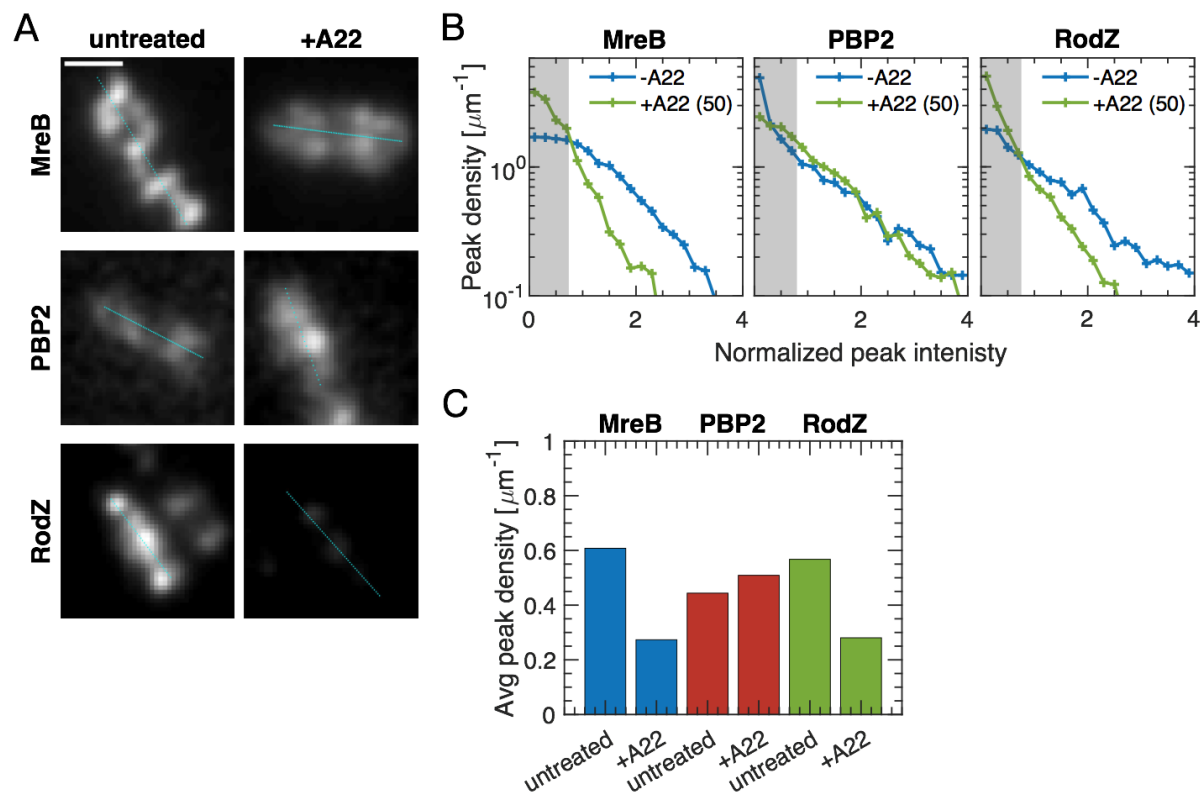
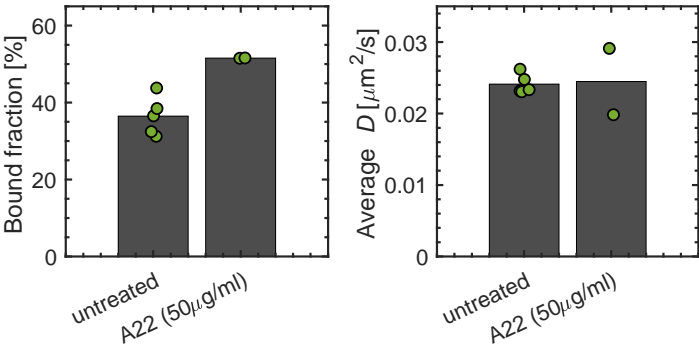


Figure 3-figure supplement 2. Spotty patterns of MreB, RodZ and PBP2 in TIRF microscopy.

(A) Sample TIRF images with cell centerline plotted in cyan. Scale bar 1 μm .

(B-C). In analogy to Fig. 3C-D, TIRF microscopy shows that A22 (30 min; 50 $\mu\text{g/ml}$) visibly reduces peak number and intensity of MreB-msfGFP and GFP-RodZ but not of mCherry-PBP2.

1901



1902

1903

1904 **Figure 3—figure supplement 3. Verification of bound fraction measurements with A22**
1905 **treated cells carrying the msfGFP-PBP2 fusion.**

1906 Bound fractions and average diffusion constants for untreated and A22-treated (for 30
1907 minutes) cells carrying the msfGFP-PBP2 fusion (AV127). Dots represent biological
1908 replicates.

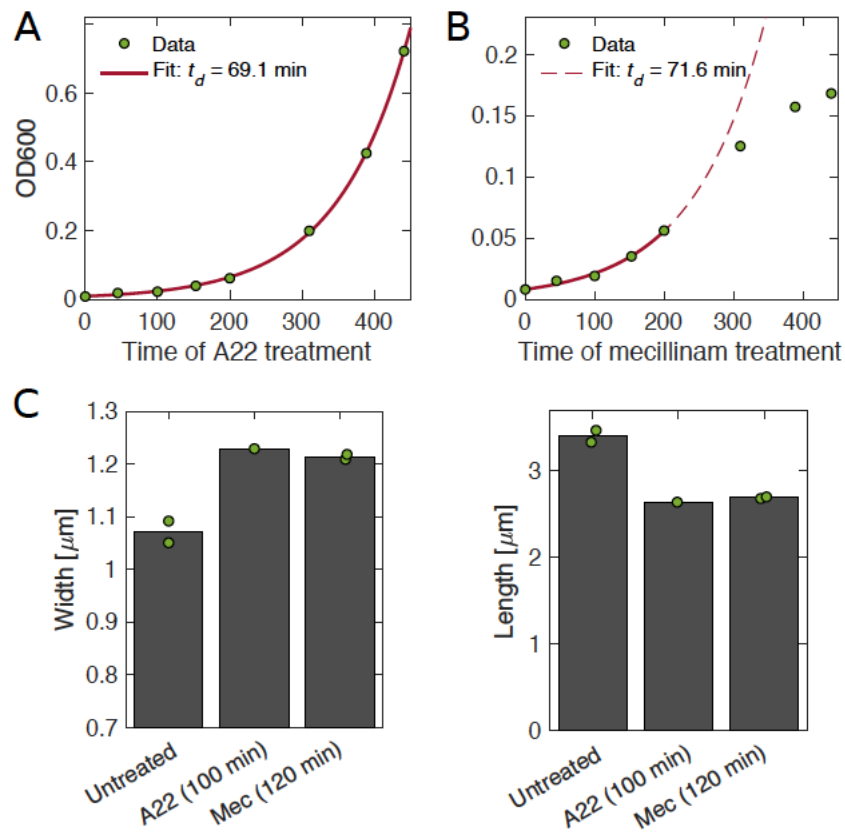


Figure 3-figure supplement 4. Growth and shape of A22- and mecillinam-treated cells.

(A-B) A22-treated cells grow unperturbed for 6 generations (A), while cells treated with mecillinam show a reduced growth rates after around 3 generations (B). **(C)** Cell shape of cells treated with A22 (A) and mecillinam (B). In both cases, cells become wider and shorter. Dots represent technical replicates.

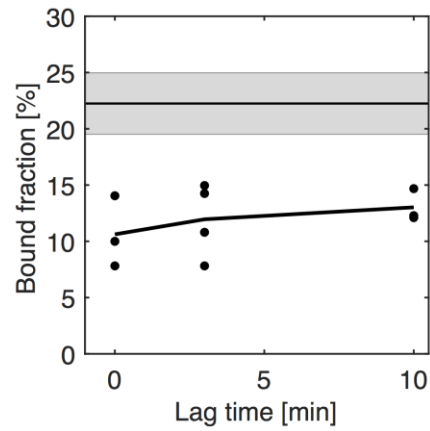
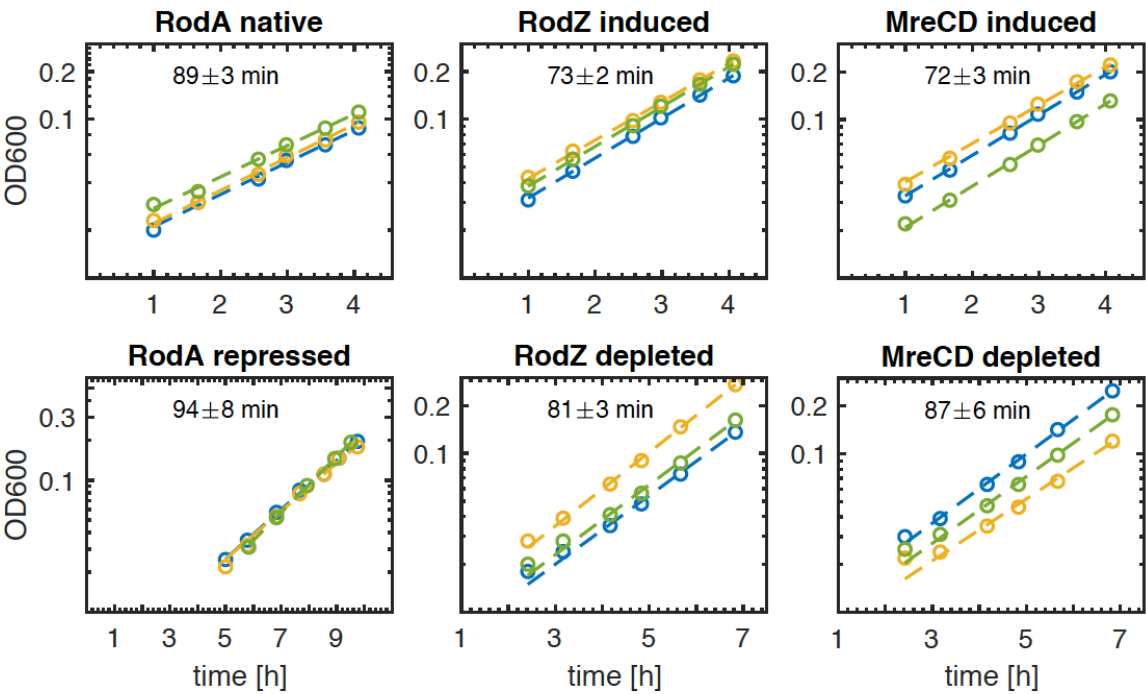


Figure 4—figure supplement 1. Change in the bound fraction after photobleaching of untreated cells.

The horizontal line corresponds to the mean bound fractions obtained from unbleached cells (see Fig 3). Error bars and shaded area show standard deviations between at least 3 technical replicates.

1925



1926

1927

1928

Figure 5—figure supplement 1. Depletion of Rod-complex components shows no effect on growth.

1929

1930

1931

1932

Growth curves for the different depletion strains in induced and depleted conditions as a function of time after initiating protein depletion. The doubling time is obtained from an exponential fit. 3 biological replicates for each condition. Y-axis is shown in log-scale.

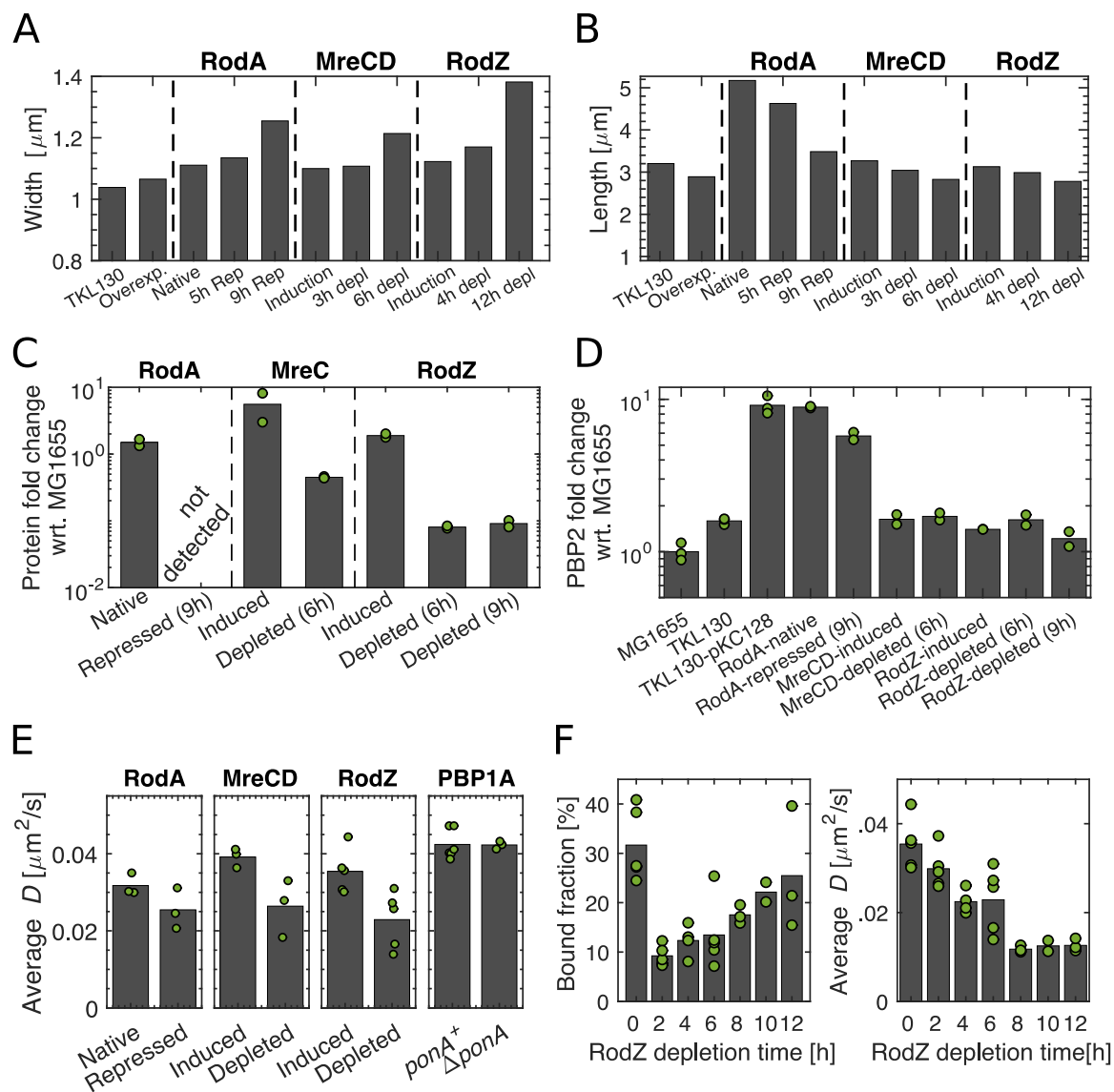


Figure 5-figure supplement 2. Depletion of Rod-complex components.

(A-B) Cell length and width upon repression of RodA, and depletion of MreCD or RodZ at different time points after initiating protein depletion.

(C-D) Levels of RodA, MreC, and RodZ (C) and levels of PBP2 (D) acquired by mass spectrometry (DIA). Protein levels are normalized by the mean of the corresponding protein level in MG1655. Dots represent two biological replicates for each condition.

(E) Average diffusion constants drop upon repression of potential members of the Rod complex. Dots represent biological replicates.

(F) Bound fraction and average diffusion constant of PBP2-PAmCherry at different time points during RodZ depletion. Dots represent biological replicates.

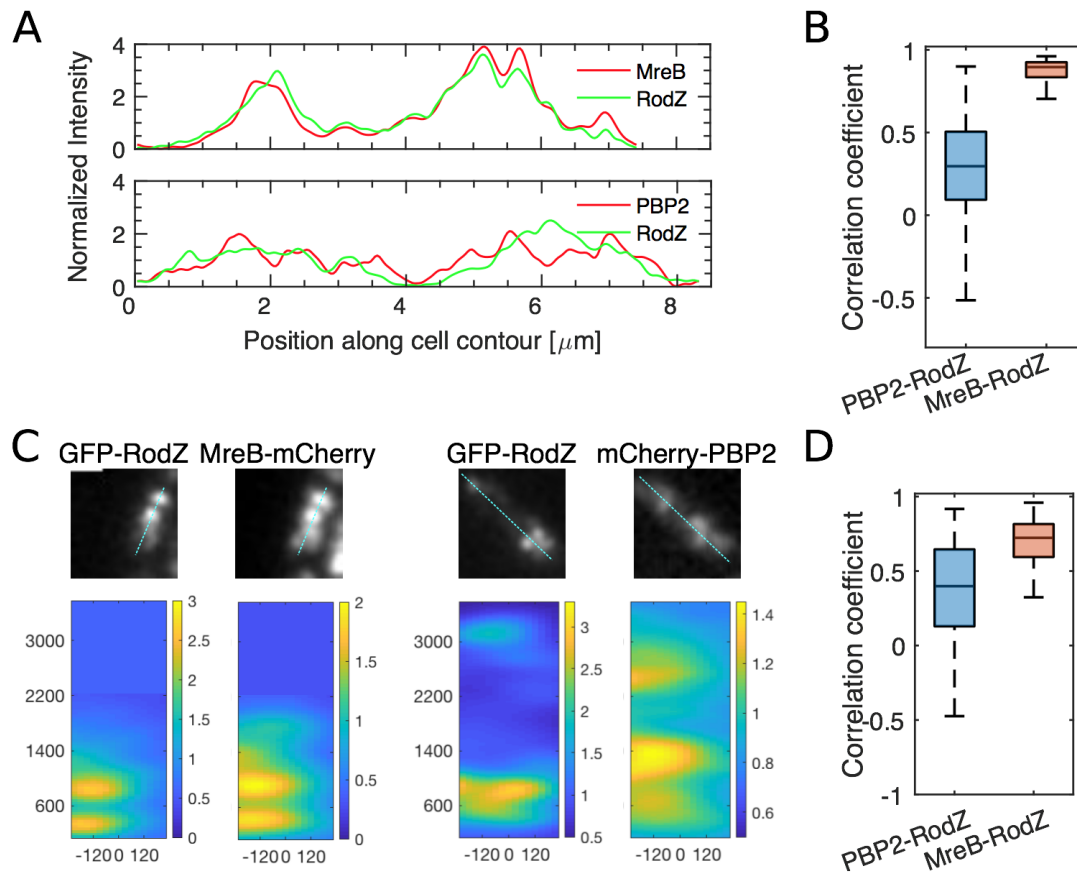


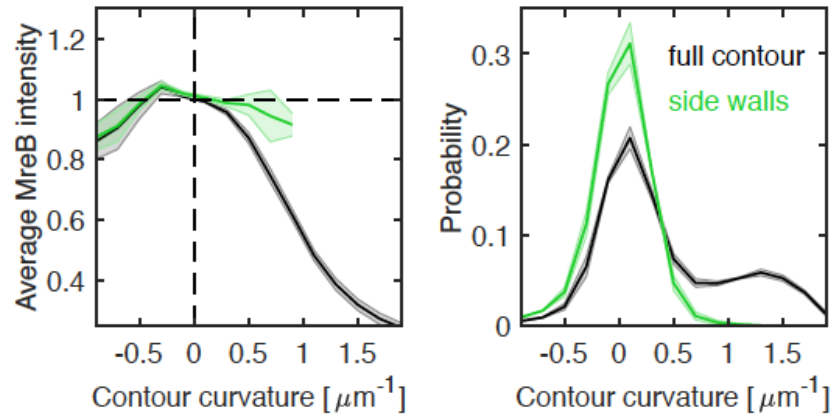
Figure 5-figure supplement 3. RodZ and PBP2 do not colocalize, while RodZ and MreB do.

(A) Sample profiles along the cell centerline of different cells carrying MreB-mCherry and GFP-RodZ fusions ($\Delta\text{rodZ mreB} \leftrightarrow \text{mreB-mCherry}$ ($P_{\text{lac}}::\text{gfp-rodZ}$)) (**top**) or mCherry-PBP2 and GFP-RodZ fusions ($\Delta\text{rodZ mrdA} \leftrightarrow \text{mCherry-mrdA}$ ($P_{\text{lac}}::\text{gfp-rodZ}$)) (**bottom**) acquired by epi-fluorescence microscopy. Intensities are normalized by the median value and then smoothened with a Gauss filter with standard deviation of 33 nm (0.5 pixel).

(B) Boxplots of Pearson correlation coefficients between PBP2- and RodZ signals (**left**) and between MreB-and RodZ signals (**right**) acquired by epi-fluorescence microscopy.

(C) Sample snapshots and corresponding intensity maps of cells carrying mCherry-PBP2 and GFP-RodZ fusions ($\Delta\text{rodZ mrdA} \leftrightarrow \text{mCherry-mrdA}$ ($P_{\text{lac}}::\text{gfp-rodZ}$)) (**left**) or MreB-mCherry and GFP-RodZ fusions ($\Delta\text{rodZ mreB} \leftrightarrow \text{mreB-mCherry}$ ($P_{\text{lac}}::\text{gfp-rodZ}$)) (**right**) acquired by TIRF microscopy. Intensities are normalized by the median value. x-axis show position along the short axis of the cell where zero corresponds to the centerline (mid-cell). y-axis is then the position along the cell's long axis. Distances are given in nm. Scale bar shows 1 μm . Intensity maps are stretched in x-direction for better visibility.

(D) Boxplots of Pearson correlation coefficients between PBP2- and RodZ signals (**left**) and between MreB-and RodZ signals (**right**) acquired by TIRF microscopy.



1965

1966

1967

Figure 6—figure supplement 1. Correlations between MreB and contour curvature in WT cells.

1968

1969

1970

Left. Normalized average MreB intensity as a function of local contour curvature in strain NO53 (*mreB*↔*mreB-msfGFP*). Comparison between correlations obtained from full contours (black) and side walls (green).

1971

1972

Right. Distributions of contour-curvature values corresponding to correlation plots on the left. Shaded areas show standard deviation between 3 biological replicates.

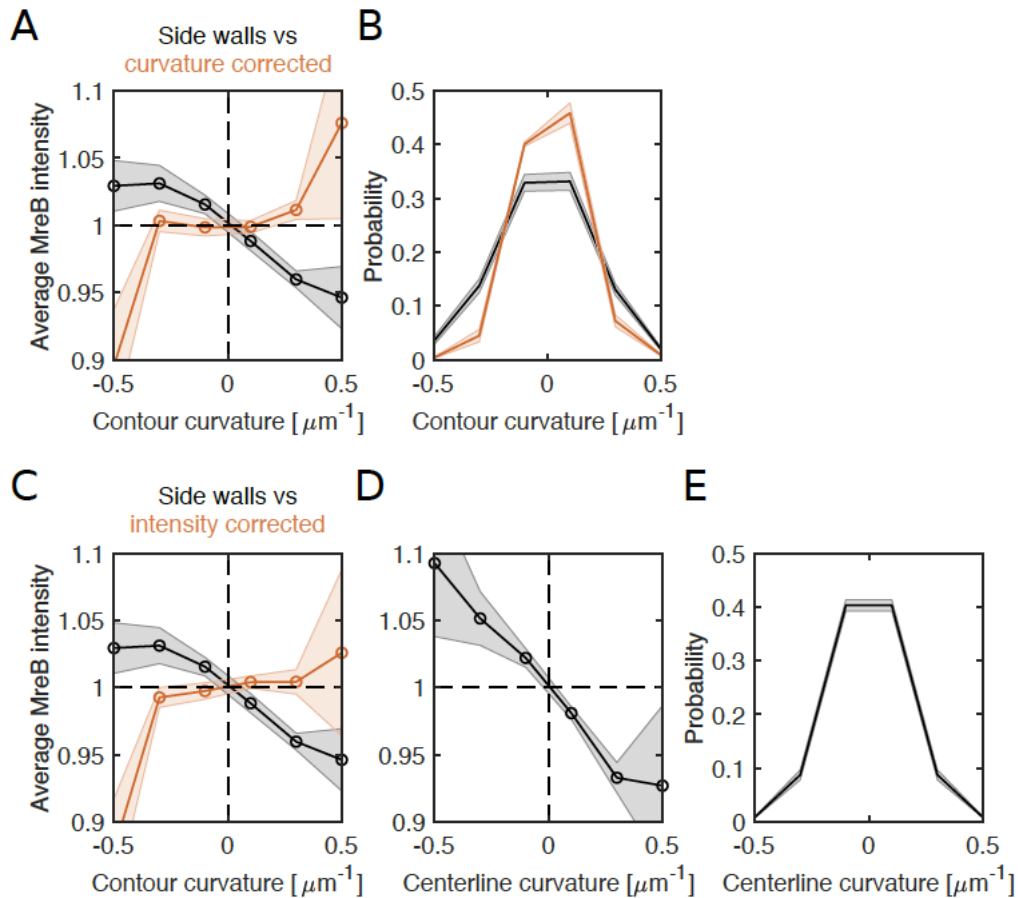


Figure 6—figure supplement 2. Loss of correlations between MreB and contour curvature after renormalizing either curvature or intensity for cell bending in filamentous cells.

(A-B) Curvature correction. **(A)** Average MreB intensity as a function of contour curvature (black) and bending-corrected contour curvature (orange) in NO53/pDB192 ($P_{lac}::sulA$). **(B)** Distributions of contour curvature (black) and corrected contour curvature (orange). Curvature correction leads to a narrower distribution while ~80% of local curvature values keep their original sign of curvature.

(C-E) Intensity correction. **(C)** Average MreB intensity as a function of bending-corrected MreB-intensity (orange). Intensity is corrected for observed correlations between MreB intensity and centerline curvature in (D) (Methods). **(D)** Average MreB intensity as a function of smoothed centerline curvature (using a Gauss filter of $\sigma = 80$ nm). **(E)** Centerline-curvature distribution. Shaded areas show standard deviation between 3 biological replicates.

1988 [Supplementary files](#)

1989 **Supplementary File 1. PBP2 levels and dynamics.**

1990 **a.** Unperturbed conditions. Measurement results at different levels of PAmCherry-PBP2 and
1991 msfGFP-PBP2 as well as msfGFP-PBP2(L61R). Protein levels are measured based on
1992 fluorescence, mass spectrometry (DIA and PRM), and Western Blots.

1993 **b.** PBP2 dynamics under different perturbations corresponding to Figs. 3 and 5.

1994

1995 **Supplementary File 2. Comparison of 2- and 3-state diffusion models.**

1996 **a, b.** Measurements of PAmCherry-PBP2 in TKL130 and TKL130/pKC128, constraining
1997 $D_0=0$ **(a)** or leaving D_0 free **(b)**.

1998 **c.** All measurements carried out with the msfGFP-PBP2 or msfGFP-PBP2(L61R) fusions.

1999

2000 **Supplementary File 3. Strains (a), plasmids (b), and primers (c) used in this study.**

2001

2002 [Video captions](#)

2003 **Fig. 1–Video 1. High-frequency imaging of PAmCherry-PBP2.**

2004 **Left.** Denoised bright-field image taken at the beginning of the video. **Right.** Raw images
2005 from high-frequency imaging (imaging interval 60 ms) of PAmCherry–PBP2 show diffusive
2006 and bound molecules. Blue circles and lines represent peaks and corresponding tracks
2007 considered for analysis.

2008 **Fig. 1– Video 2. Low-frequency imaging of PAmCherry-PBP2.**

2009 **Left.** Denoised bright field image **Right.** Raw images from low frequency imaging (imaging
2010 interval 3.5 s) of PAmCherry–PBP2 show immobile and persistently moving molecules. Blue
2011 circles and lines represent peaks and corresponding tracks considered for analysis.

2012 **Fig. 1– Video 3. High-frequency imaging of msfGFP-PBP2.**

2013 **Left.** Denoised bright field image taken at the beginning of the video. **Right.** Raw images
2014 from high frequency imaging (imaging interval 60 ms) of msfGFP–PBP2 (AV127) show
2015 diffusive and bound molecules. Blue circles and lines represent peaks and corresponding
2016 tracks considered for analysis.

2017 **Fig. 1– Video 4. Low-frequency imaging of msfGFP-PBP2**

2018 **Left.** Denoised bright field image **Right.** Raw images from low frequency imaging (imaging
2019 interval 3.5 s) of msfGFP–PBP2 (AV127) show immobile and persistently moving molecules.
2020 Blue circles and lines represent peaks and corresponding tracks considered for analysis.

2021 **Fig. 3– Video 1. MreB-msfGFP imaging**

2022 **Left.** Phase contrast image taken at the beginning of the video. **Right.** Raw images of MreB-
2023 msfGFP motion (imaging interval 1 s) of NO53 cells. Blue circles and lines represent peaks
2024 and corresponding tracks considered for analysis.

2025 **Fig. 3– Video 2. MreB-msfGFP imaging of A22 treated cells**

2026 **Left.** Phase contrast image taken at the beginning of the video. **Right.** Raw images of MreB-
2027 msfGFP motion (imaging interval 2 s) of NO53 cells treated with 20 $\mu\text{g/ml}$ A22 for a duration
2028 of 30 minutes. Blue circles and lines represent peaks and corresponding tracks considered
2029 for analysis.

2030 Supplemental datasets for figures and tables

2031 Source Data File 1 – Data related to Figure 1.

2032 The file Dataset-Fig1.xlsx contains:

2033 **Fig. 1H-I.** Number of tracks, average diffusion constants, bound and persistent fractions for
2034 PAmCherry-PBP2 for native and overexpression conditions, including p-values for bound
2035 and persistent fractions.

2036 **Fig. 1F-G.** Numerical values of the distribution of speeds and orientations of PAmCherry-
2037 PBP2 and MreB-msfGFP tracks from low frequency imaging and number of tracks
2038 considered.

2039 **Fig1. SI1B-C.** Width, length and doubling times obtained from OD600 measurements of
2040 MG1655, TKL130, and TKL130/pKC128 cells.

2041 **Fig1. SI1D.** Bocillin labeling, fluorescence and mass spectrometry measurements of
2042 MG1655, TKL130, and TKL130/pKC128 cells.

2043 **Fig1. SI2.** Values of bound fractions, average diffusion constants, and sum of residuals of
2044 PAmCherry-PBP2 tracks from TKL130/pKC128 strain with high frequency imaging given by
2045 the Spot-On method using 2- or 3-state diffusion model.

2046 **Fig1. SI3.** Values of bound fractions and diffusion constants of PAmCherry-PBP2 tracks
2047 from TKL130/pKC128 strain to compare the results from Spot-On with the D_{eff} based
2048 method.

2049 **Fig1. SI5.** Raw data for Fig. 1F-G. List of velocity, orientation and goodness of fit (R^2).

2050 **Fig1. SI7.** Number of bound or active PBP2 molecules as a function of the number of PBP2
2051 molecules per cell acquired from mass spectrometry and fluorescence measurements.

2052 **Fig1. SI8A.** Shape and OD600 measurements of cells carrying the msfGFP-PBP2 fusion
2053 expressed from the native or P_{Lac} promoters with different induction levels of IPTG.

2054 **Fig1. SI8B.** Fluorescence and Western Blot quantifications and mass spectrometry (both
2055 DIA and PRM) of cells carrying the msfGFP-PBP2 fusion expressed from the native or P_{Lac}
2056 promoters with different induction levels of IPTG

2057 **Fig1. SI8C.** Values of number of tracks, average diffusion constants, and bound fractions for
2058 cells carrying the msfGFP-PBP2 fusion, including p-values for bound fractions.

2059 **Fig1. SI9.** Shape and fluorescence measurements, number of tracks, average diffusion
2060 constants and bound fractions from high frequency imaging of cells carrying msfGFP-PBP2
2061 fusion with induction levels of 5 and 25uM IPTG after different times of growth, including p-
2062 values for bound fractions.

2063 **Fig1. SI10A.** Values of number of tracks, and persistent fractions for cells carrying msfGFP-
2064 PBP2 fusion expressed from the native or P_{Lac} promoters with different induction levels of
2065 IPTG, including p-values for persistent fractions.

2066 **Fig1. SI10B.** List of velocity and goodness of fit (R^2) values for cells carrying msfGFP-PBP2
2067 fusion under different induction levels of IPTG.

2068

2069 Source Data File 2 – Data related to Figure 2.

2070 The file Dataset-Fig2.xlsx contains:

2071 **Fig. 2B.** Values of switching rates of PAmCherry-PBP2 and msfGFP-PBP2 tracks from low
2072 frequency imaging and number of tracks considered.

2073 **Fig. 2C.** Values of histogram counts of track lengths of msfGFP-PBP2 tracks for lifetime
2074 measurements.

2075

2076 [Source Data File 3 – Data related to Figure 3.](#)

2077 The file Dataset-Fig3.xlsx contains:

2078 **Fig. 3C-D.** Numerical values of the distribution of peak intensities, average peak density,
2079 pixel noise and number of cells considered for untreated and A22-treated cells carrying
2080 either mCherry-PBP2, MreB-msfGFP, or GFP-RodZ fusion.

2081 **Fig. 3E.** Number of tracks, average diffusion constants, and bound fractions from high
2082 frequency imaging for non-treated, A22- and Mecillinam- treated cells from TKL130,
2083 including p-values for bound fractions and diffusion constants.

2084 **Fig. 3F.** Number of tracks and persistent fractions from low frequency imaging for non-
2085 treated, A22- and Mecillinam- treated cells from TKL130, including p-values for persistent
2086 fractions.

2087 **Fig3. SI2.** Numerical values of the distribution of peak intensities, average peak density,
2088 pixel noise and number of cells considered for untreated and A22-treated cells carrying
2089 either mCherry-PBP2, MreB-msfGFP, or GFP-RodZ fusion.

2090 **Fig3. SI3.** Number of tracks, average diffusion constants, and bound fractions from high
2091 frequency imaging for non-treated and A22-treated cells from AV127, including p-values for
2092 bound fractions and diffusion constants.

2093 **Fig3. SI4.** Width, length and doubling time from OD600 measurements for non-treated, A22-
2094 treated and Mecillinam- treated cells from TKL130.

2095

2096 [Source Data File 4 – Data related to Figure 4.](#)

2097 The file Dataset-Fig4.xlsx contains:

2098 **Fig. 4B.** Number of tracks and bound fractions from Bound-molecule-FRAP measurements
2099 at different time lags with A22-treated cells from TKL130.

2100 **Fig. 4C.** Values of histogram counts of track lengths of msfGFP-PBP2 tracks from A22-
2101 treated cells for lifetime measurements.

2102 **Fig4. SI1.** Number of tracks and bound fractions from bound-molecule-FRAP measurements
2103 at different time lags with non-treated cells from TKL130.

2104

2105 [Source Data File 5 – Data related to Figure 5.](#)

2106 The file Dataset-Fig5.xlsx contains:

2107 **Fig. 5C.** Number of tracks, average diffusion constants and bound fractions of PAmCherry-
2108 PBP2 tracks from high frequency imaging during depletion of Rod-complex components,
2109 including p-values for bound fractions and diffusion constants.

2110 **Fig. 5D.** Number of tracks and persistent fractions of PAmCherry-PBP2 tracks from low
2111 frequency imaging during depletion of Rod-complex components, including p-values for
2112 persistent fractions.

2113 **Fig5. SI1.** OD600 measurements during depletion of Rod-complex components.

2114 **Fig5. SI2A-B.** Shape measurements during depletion of Rod-complex components.

2115 **Fig5. SI2C-D.** Mass spectrometry measurements (DIA method) of MreC, RodA, RodZ, and
2116 PBP2 during depletion of Rod-complex components. Protein levels are normalized by the
2117 mean of the corresponding protein level in MG1655.

2118 **Fig5. SI2E.** see data for Fig. 5C.

2119 **Fig5. SI2F.** Number of tracks, average diffusion constants, and bound fractions of
2120 PAmCherry-PBP2 tracks from high frequency imaging at different times of RodZ depletion,
2121 including p-values for diffusion constants and bound fractions.

2122 **Fig5. SI3B, D.** Pearson correlation coefficients between (i) mCherry-PBP2 and GFP-RodZ
2123 or (ii) MreB-mCherry and GFP-RodZ signals for each cell.
2124

2125 [Source Data File 6 – Data related to Figure 6.](#)

2126 The file Dataset-Fig6.xlsx contains:

2127 **Fig. 6C-D.** For filamentous NO53 cells, numerical values of correlations between contour
2128 curvature and normalized MreB-msfGFP intensities for the full contour, side walls or flat
2129 regions with number of cells considered.

2130 **Fig. 6E-F.** For filamentous NO53 cells, numerical values of the distribution of contour
2131 curvatures for the full contour, side walls or flat regions with number of cells considered.

2132 **Fig6. SI1.** For NO53 cells, numerical values of the (i) correlations between contour curvature
2133 and normalized MreB-msfGFP intensities, and (ii) distribution of contour curvatures for the
2134 full contour and side walls.

2135 **Fig6. SI2.** For filamentous NO53 cells, numerical values of (i) correlations between
2136 curvature and normalized MreB-msfGFP intensities, and (ii) curvature distributions after
2137 applying curvature or intensity correction methods.

2138